INVESTIGATION OF SOLUTION VERIFICATION AND VALIDATION OF NUCLEAR THERMAL HYDRAULICS COMPUTATIONAL FLUID DYNAMICS USING TWIN RECTANGULAR TURBULENT JETS

A Dissertation

by

LANE B. CARASIK

Submitted to the Office of Graduate and Professional Studies of
Texas A&M University
in partial fulfillment of the requirements for the degree of

DOCTOR OF PHILOSOPHY

Chair of Committee,	Yassin A. Hassan
Committee Members,	Mark L. Kimber
	Maria D. King
	Hamn-Ching Chen
Head of Department,	Yassin A. Hassan

May 2017

Major Subject: Nuclear Engineering

ABSTRACT

The research and development of advanced nuclear reactors requires complementary experimental and computational approaches. These approaches are used in such a manner that experimental campaigns help validate computational tools. These computational tools are then utilized for similar scenarios where experimental efforts would be prohibitive due to variety of reasons including cost. Advanced reactor designs, such as sodium fast reactors, very high temperature reactors, and molten salt reactors motivate this work due to the exotic coolants used. The exotic coolants require surrogate experiments for fluids of specific thermal physical properties to mirror their properties.

There are established standards of verification and validation methods that are broken up into code and solution (also known as calculational) pathways. Code verification and validation is in the realm of the code developer while solution verification and validation is in the realm of the user. The current work reported is focused on the later and tries to do so without any assumptions regarding code verification and validation. The work conducted focuses on a case study to show an alternate means of solution verification that is pursued without restrictive methods such as Grid Convergence Index and its variants. It is not meant to be a rigorous means of developing error bands (uncertainty bands) for realistic computational fluid dynamics analysis (including 3-D effects such as turbulence) though there is an attempt to do so. The sample case study provides future users an approach to determine if their computational fluid dynamics studies are sufficient without the aforementioned methods (i.e. mesh convergence without a commentary on the error bands).

The case study used in this work is based on twin planar-like turbulent jets exhausting into a large volume of fluid. The two jets combine into a single turbulent free shear

planar jet which can be shown through velocity, vorticity, and Reynolds stress information in the areas of interest. The simulations used to model this case are done using the computational fluid dynamics code, Star-CCM+. Based on this effort, a simple mesh convergence methodology is proposed and a solution validation analysis was conducted. The computational fluid dynamics simulations were shown to have reasonable agreement with the experimental works within the Twin Jet Water Facility. It is hoped this work will help provide an alternate pathway for code users of computational fluid dynamics tools to do simple and effective solution verification and validation.

DEDICATION

To my siblings, godparents, and family friends who have been supportive of my education and career goals throughout my life. To my lifelong friends who have supported me in a similar fashion. To my grade school teachers who saw the potential in me when others didn't.

To my sister, Erika who spent countless hours teaching me how to read, how to love learning, and to always be curious.

To the academic community that raised me during my formidable years of being a clueless freshman into the academic researcher I am today. In particular, Dr. Yassin A. Hassan, Dr. Lawrence Heilbronn, Dr. Arthur Ruggles, Dr. Lawrence Townsend, Dr. Pavel Tsvetkov and Mr. Imad El-Jeaid all made major contributions in my education.

ACKNOWLEDGMENTS

This material is based upon work supported under a Department of Energy Nuclear Energy University Programs Graduate Fellowship. Additionally, any opinions, findings, conclusions or recommendations expressed in this publication are those of the authors and do not necessarily reflect the views of the Department of Energy Office of Nuclear Energy.

Portions of this research were conducted with high performance research computing resources provided by Texas A&M University (http://hprc.tamu.edu).

CONTRIBUTORS AND FUNDING SOURCES

Contributors

This work was supported by a dissertation committee consisting of Professor(s) Yassin A. Hassan and Mark Kimber of the Department of Nuclear Engineering, Professor Hamn-Chen of the Department of Civil Engineering, and Professor Maria King of the Department of Mechanical Engineering. This work was supported by Dr. W. David Pointer of Oak Ridge National Laboratories as a special appointment on the dissertation committee.

All other work conducted for the dissertation was completed by the student independently.

Funding Sources

Graduate study was supported by a College of Engineering Graduate Teaching Fellowship from Texas A&M University and by a Nuclear Energy University Program Graduate Fellowship from the United States Department of Energy.

This material is based upon work supported under a Department of Energy Nuclear Energy University Programs Graduate Fellowship.

NOMENCLATURE

AES	Approximate Error Splines
ASME	American Society of Mechanical Engineering
CFD	Computational Fluid Dynamics
CP	Combined Point
D.O.F	Degrees of Freedom
GCI	Grid Convergence Index
GRE	Generalized Richardson Extrapolation
HTTR	High Temperature Test Facility
HWA	Hot-Wire Anemometry
LDV	Laser Doppler Velocimetry
LES	Large Eddy Simulations
LIF	Laser Induced Fluorescence
LS-GCI	Least Squares Grid Convergence Index
MP	Merge Point
MHTGR	Modular High Temperature Gas Reactor
MSR	Molten Salt Reactor
PCC	Pressurized Conduction Cooldown

PDE	Partial Difference Equations
PIV	Particle Imaging Velocimetry
RANS	Reynolds Averaged Navier-Stokes
RSM	Reynolds Stress Turbulence Model
SEM	Standard Error of the Mean
SFR	Sodium Fast Reactors
TAMU	Texas A&M University
TJWF	Twin Jet Water Facility
UTK	University of Tennessee, Knoxville
UVP	Ultrasonic Velocimetry Probe
VHTR	Very High Temperature Reactors
V&V	Verification and Validation

TABLE OF CONTENTS

Page

LIST OF FIGURES

FIGURE Page

LIST OF TABLES

TABLE Page

1. INTRODUCTION AND LITERATURE REVIEW*

1.1 Generation IV Reactor Development

The next era of advanced reactors, coined "Generation IV" reactors, are considered the next evolutionary step of reactor technologies. In 2000, the Gen IV forum determined that a shortlist of six types (figure 1.1) of reactor designs are need to be focused on for development and potential deployment. These reactors have various advantages such as higher operating temperatures, closed fuel cycles, and coupling to high temperature thermo-chemical production or desalination. The higher temperatures allow for higher thermal power cycle efficiency while achieving lower operating pressures. The lower operating pressures, due to the properties of the working fluids (such as sodium or molten salt), contribute towards a potentially lower design, construction, and maintainability cost.

Many of the designs have geometric features that encourage the formation of hot coherent jets that may impinge on vessel structures or free surfaces. The impingement on vessel structures can cause thermal striping which is the frequent cycling of fluid flowing over a structure with varying temperatures [14] and [4]. This can occur during both operation and accident conditions for reactors with large upper structures such as upper plenums in sodium fast reactors (SFR) and upper vessel heads in very high temperature reactors (VHTR) (figure 1.2). Thermal stratification, which is the layering of hotter lighter fluid on cooler denser fluid, can result from the hot jets injecting into these large vessels or

*Reprinted with permission from "Some thermal hydraulic challenges in sodium cooled fast reactors" by D. Tenchine, 2010, Nuclear Engineering and Design, 240, 1195-1217, Copyright 2010 by Elsevier.

*Reprinted with permission from "The Structure of a self-preserving turbulent plane jet" by L. J. S. Bradbury, 1965, Journal of Fluid Mechanics, 23, 31-64, Copyright 1965 by Cambridge University Press.

*Reprinted with permission from "Experimental and Numerical Investigation of Two-Dimensional Parallel Jets" by E. A. Anderson and R. E. Spall, 2001, Journal of Fluids Engineering, 123, 401-406, Copyright 2001 by ASME.

*Reprinted with permission from "Flow structures in initial region of two interacting parallel plane jets" by N. W. M. Ko and K. K. Lau, 1989, Experimental Thermal and Fluid Science, 2, 431-449, Copyright 1989 by Elsevier.

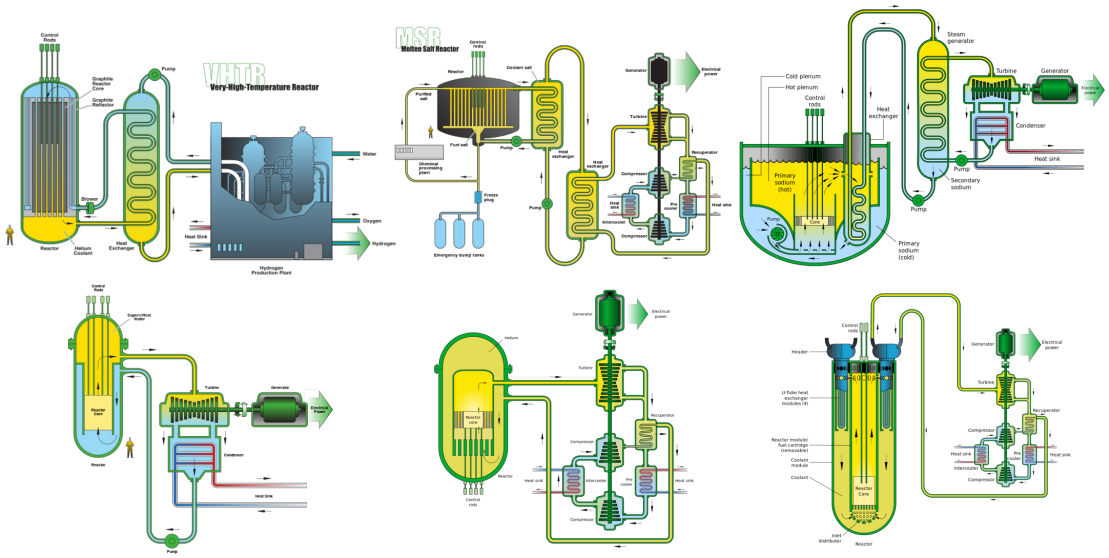

Figure 1.1: The Six Shortlisted Generation IV Reactors

enclosures. Like thermal striping, thermal stratification can lead to severe consequences if the impacted structures are not designed to accommodate the large temperature gradients between the layers of fluids. This can be intensified when a free surface (interface between a working fluid and fill gas) is encountered such as in a SFR. The temperature difference between the fill gas and working fluid with the oscillatory behavior of the free surface will cause thermal fatigue.

Neither of these behaviors are usually desirable effects in reactor safety context and are intended to be minimized. These thermal-fluid phenomena involve behavior which increase the difficulty of experimental and computational efforts. The specific behaviors such as jets of fluid injected into a free shear environment, the interaction of two or more jets, buoyancy effects, and high aspect ratios of geometry are particularly impactful on these efforts.

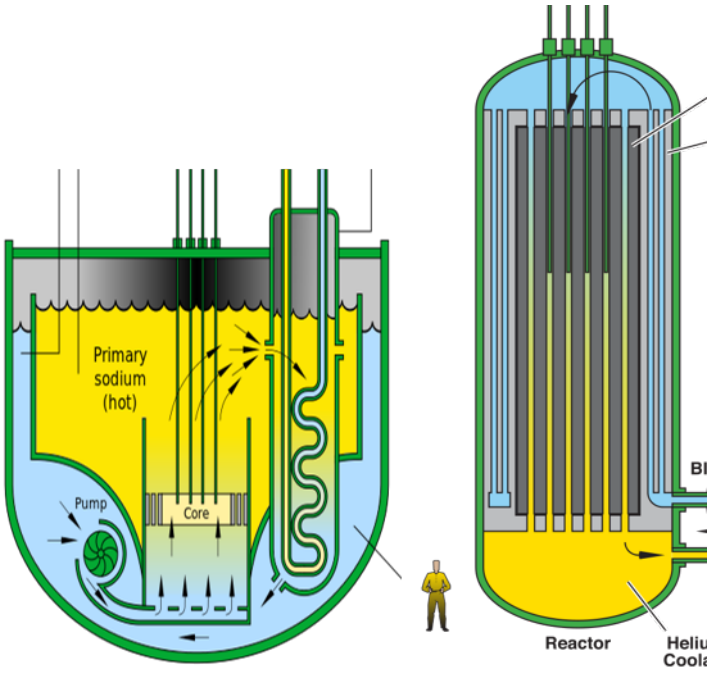

Figure 1.2: Sodium Fast Reactor [1] (Left), Very High Temperature Reactor [2] (Right)

1.1.1 Sodium Fast Reactors

There are two types of SFRs that all of the major components are contained within one large vessel (pool) or individually connected by piping (loop). This discussion focuses on the former which involves large upper plenums or enclosures with an example (European Fast Reactor) seen in figure 1.3. The SFR core, during operation and accident conditions, heat fluid that injects into the upper plenum that develop into multiple coherent heated jets. The jets experience a significantly larger environment that can be considered free shear environments for analysis purposes. These jets eventually impact on the aforementioned structures or free surfaces [14], [3]. This behavior has been the focus of experimental [15] and computational campaigns [16] and the behaviors of importance are highlighted in figure 1.4. In particular, the called out transient thermal stratification and temperature measurements are motivating current studies in this area of work.

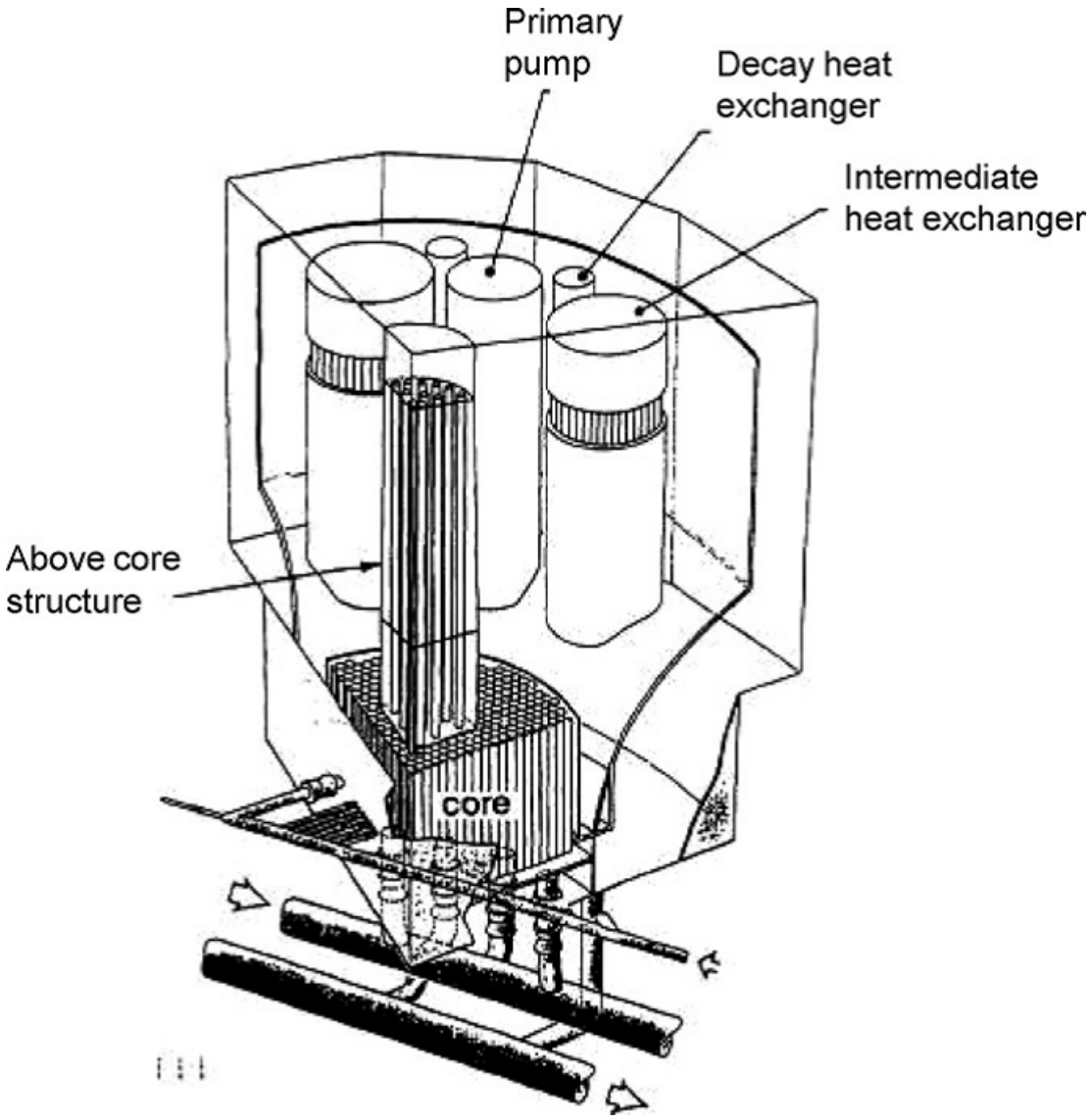

Figure 1.3: JESSICA Water Test Facility of the European Fast Reactor Upper Plenum [3]

The different behaviors seen in figure 1.4 need to be appropriately predicted to determine points of interest for operational needs such as instrumentation placement or component design. For instance, to accurately measure outlet reactor temperature, thermocouples should be placed in regions that do not encounter significant thermal striping and are representative of that region of the core. Further, these behaviors can be determined to be the

limited behavior during accident conditions and can result in significant design ramifications to account for the phenomena.

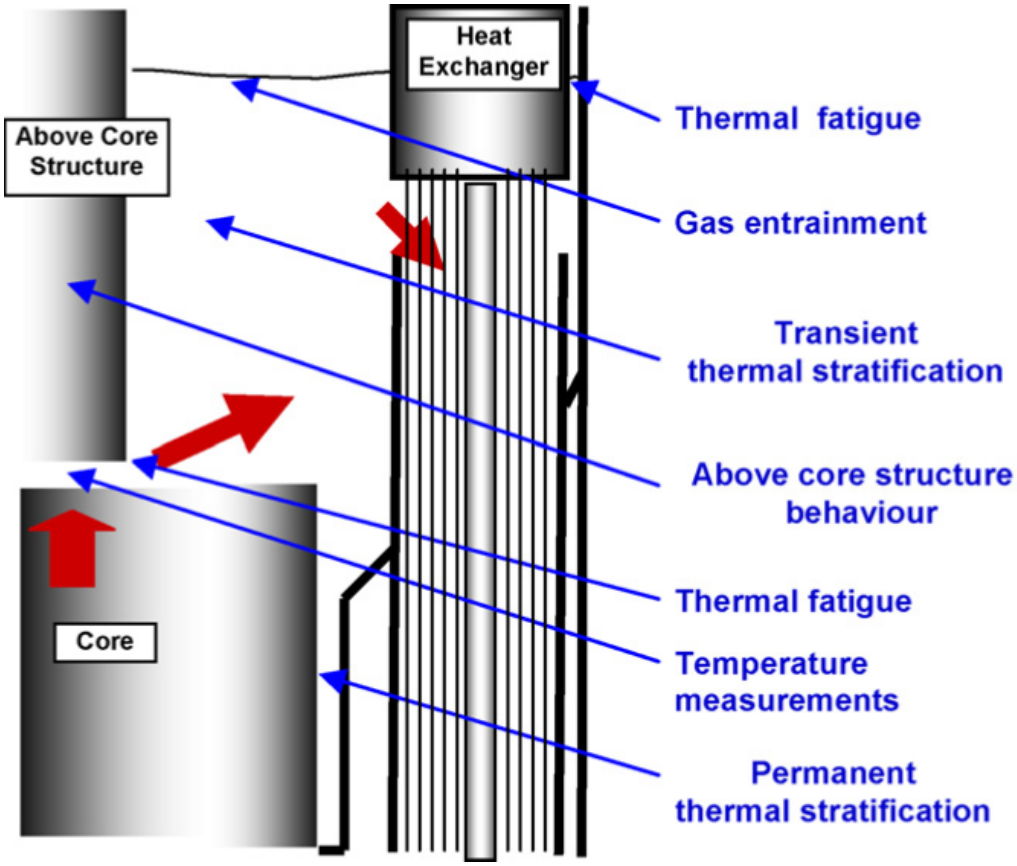

Figure 1.4: Sodium Fast Reactor Upper Plenum Behavior [3]

1.1.2 Very High Temperature Reactors

Gas reactor designs have two different types of designs, pebble bed and prismatic block, which result in radically different core geometries. The prismatic block geometry has been the focus of reactor design such as the modular high temperature gas reactor (MHTGR) [17] of which the high temperature test facility (HTTR) is based on [4]. The geometry of the MHTGR and similar designs involve a core of graphite bricks with coolant

channels placed throughout it. The coolant channels are connected to lower and upper plenums where the gas flows through as it gets heated by the core (figure 1.5. During accident scenarios such as a pressurized conduction cooldown (PCC) event, the flow in the reactor (from upper to lower plenums) reverses due to the loss of forced convection from circulator shutdown. The reactor shuts down, but the decay heat causes buoyancy effects to drive the flow in the opposite direction. Heated coherent jets develop and exhaust out of the coolant channels into the upper plenum and impinge on the upper vessel head. Aforementioned thermal striping could result and lead to severe structural damage leading to offsite releases. The experimental efforts of the HTTF and other similar facilities are used to investigated this scenario. This is a similar situation to the SFR upper plenum behavior of heated jets injected in a larger free shear environment.

1.1.3 Motivation of Current Works

Jets from small nozzles (rectangular or circular) impinging into large enclosures which are treated as free shear environments is a phenomenon that motivate the works discussed in this dissertation. The environments do not have any major structures for the jets to impact on such that the simplest case can be investigated. Specifically, this work will focus on verification and validation (V&V) techniques for computational fluid dynamics (CFD) tools simulating this behavior in a test facility (chapter 2). The next sections will discuss the current state of V&V for CFD tools, what is applicable, and where can improvements be made. Additionally, the physics involving twin planar turbulent jets are discussed in detail to provide a basis for the analysis.

1.2 Verification & Validation

CFD tools or codes have been shown to be useful for research/design in advanced reactors previously [3], but the process of verifying and validating the solutions have much left to be desired. Although it was published over a decade ago, Oberkampf's and Tru-

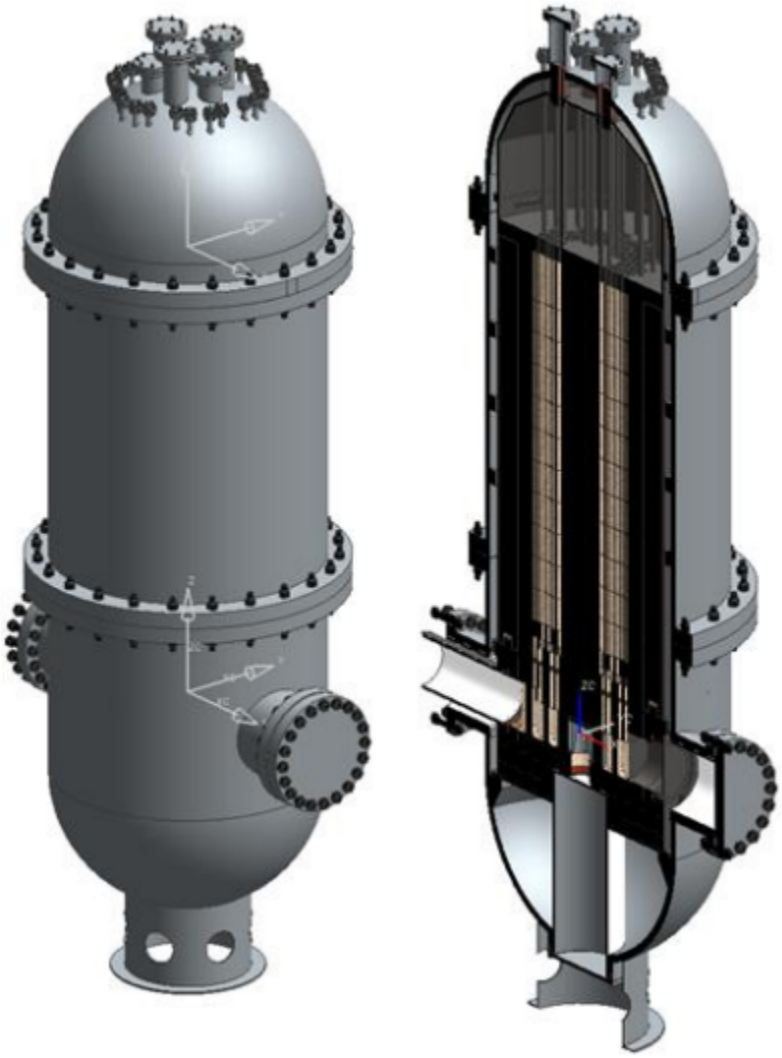

Figure 1.5: CAD Representation of High Temperature Test Facility [4]

cano's [18] paper on V&V for CFD tools still provides insightful commentary on the subject. It suggests that solution (known as calculational in some publications) V&V is more an afterthought for CFD analysis. In that, it is not commonly conducted for research efforts and much less so for design efforts. Or if conducted, they are regularly done as limited visual comparisons using data plotted on figures in the case of both verification

(computational vs. analytical or higher order computational results) and validation (computational vs. experimental results). This can be regularly seen in a significant number of recent CFD journal articles such as Journal of Fluid Engineering or Nuclear Engineering and Design. These articles make no mention or discussion of solution V&V which leave concerns about the validity of the analysis. For instance, Jayaraju et. al. [19] provides an insightful view of Reynolds averaged Navier Stokes (RANS) modeling as compared to quasi-DNS for pebble bed reactor-like geometries. Unfortunately, the work does not provide any meaningful discussion regarding the validity of the mesh used and how was it determined to be suitable for the simulations conducted. This is acceptable depending on the application or purpose of a study but the work has to be considered carefully for supporting design purposes.

Large eddy simulations (LES) and direct numerical simulations (DNS) are also difficult to conduct solution V&V methods for various reasons. Solution verification for LES and DNS are approached in a different manner such as ensuring the full range of length scales are resolved. These methods will not be a topic of discussion in this work.

For both steady and unsteady RANS, the overarching community has reached somewhat of a census that V&V efforts should be pursued but not how. In particular, a growing interest in using CFD for nuclear safety applications with solution V&V included can be seen. This is demonstrated by the Nuclear Regulatory Commission (NRC) NUREG documents outlining various CFD calculations. In NUREG-2152 [20], they suggest using generalized Richardson extrapolation (GRE) [21] with the usage of the grid convergence index (GCI) [22] as a form of verification. In the report, the authors did not present an exhaustive case to support the usage of GCI or GRE and had issues regarding inaccuracies in the use of turbulence modeling. Further, the report does not cover the determination of mesh convergence (i.e. sufficient amount of refinement) for a calculation's set of meshes.

The role of V&V is fundamental towards making CFD tools suitable for these usage

of design and development efforts for advanced reactors [23]. V&V of computational tools can be separated into two major types, code and solution (or calculational). Code V&V is predominantly in the domain of the developers of a specific tool or code. Whereas solution V&V would be activities conducted by users/analysts of the tool/code for their specific case. This discussion is focused on the latter in the context of advanced reactors.

1.3 Solution Verification

Solution verification for CFD emphasizes building a case of evidence for showing a specific CFD calculation is correct and accurate within a specific bound. The standard version of solution verification is focused on grid and time step convergence/sensitivity as a posteriori type of analysis [18]. When solution verification is provided for a CFD study, mesh convergence can be shown by simple visual comparisons and/or numerical comparisons such as L^2 norms. This has been a steadfast manner of observing mesh convergence, but there has been movement towards a more rigorous process since the early 1990s. This process was initiated by Roache [22] in his early efforts to establish a basic means of showing mesh convergence and sensitivity.

For the work presented in this dissertation, a differentiation between mesh convergence and mesh sensitivity is provided to ensure clarity of the results and conclusions. Mesh convergence is defined as the mesh density or grid size shown to be sufficient for further sensitivity analysis or comparisons to validation data. Mesh sensitivity is defined as the development of uncertainty/error bands associated with a specific mesh density or grid size determined using a posteriori analysis. These definitions are likely not consistent with the V&V communities definitions of these items, though most of the CFD community does not use these terms consistently.

1.3.1 Mesh Convergence

In order to do mesh convergence studies, an analyst would traditionally plot a meaningful quantity or parameter resulting from a series of CFD simulations. The plotted results are obtained using different meshes of an arbitrary, but significant, level of refinement between each mesh. The analyst would compare the graphical results and through either qualitative and/or quantitative comparison determine what amount of mesh refinement is needed for further studies. For the quantitative comparison, the analyst may define a specific criteria of two numbers that are within some percent or absolute difference as converged (for instance, 5% difference where neither are treated as the "true" answer). This is found to be effectively standard practice within the overall CFD community. An example of which can be found in Anderson's twin jet works [7] which is topically related to the current works. Currently, there is no census on how mesh convergence studies should be conducted by the overarching CFD community. Some groups argue mesh convergence can be shown by determining the uncertainty from the discretization error. While other groups use visualizations and basic numerical comparisons to show mesh convergence. Although one significant point that can be drawn from both ends of the spectrum, a basic means of showing mesh convergence is important and should be shown/provided. A large effort of current V&V work is focused on determining the discretization error of a specific set of calculations. The discretization error is defined as the difference between the exact solution of a PDE and the numerical solution. The error is associated with converting a continuous function or equation into a discrete set of equations. The discretization error is shown as,

$$E_n = f_n - f_{exact} \tag{1.1}$$

where f_n is a meaningful quantity predicted by a numerical method and f_{exact} is the exact

solution.

This is complicated by the majority of meaningful engineering analysis do not have an exact solution. Which is why numerical methods are used for solving PDEs, but exact solution estimators such as GRE can be used to as a replacement. This is complicated by two points, the first being the requirement that solutions used for estimating the exact (or extrapolated) solution need to be in the asymptotic range (i.e. mesh size becomes small or close to zero). An example of an asymptotic range is shown in figure 1.6 for the $1-D$ transient heat conduction equation for an insulated rod. The second point is that it is difficult to reach the asymptotic range for every flow situation due to the demand of computational resources.

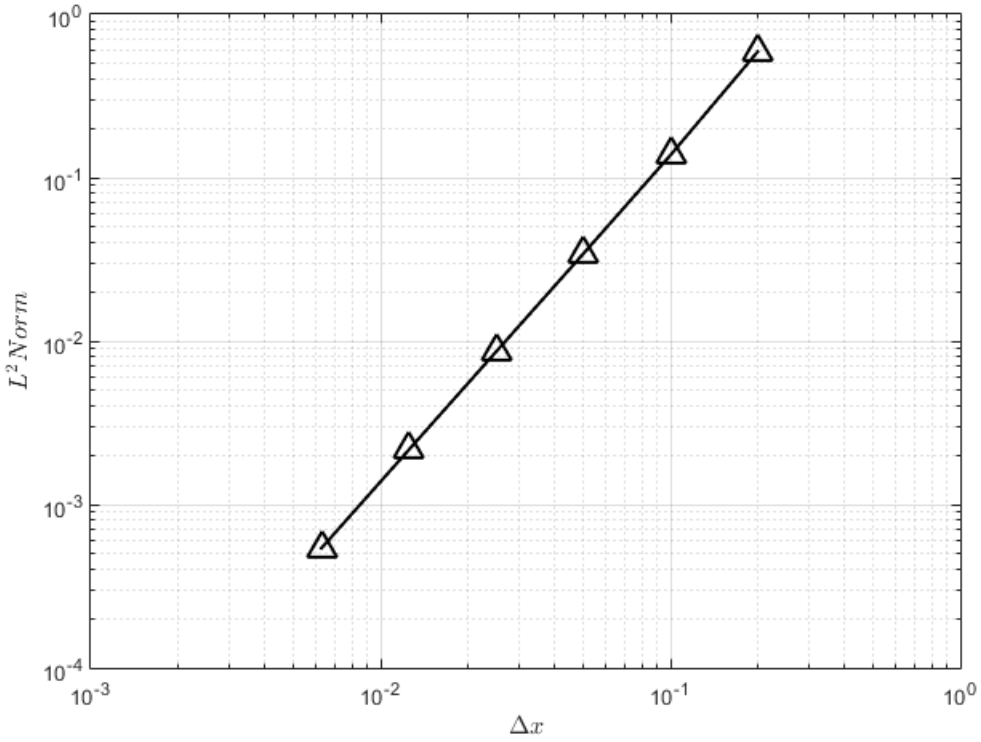

Figure 1.6: Asymptotic Range shown using a Mixed-Order (1^{st} Order Time and 2^{rd} Order Space) Scheme for Transient Heat Condition [5]

Other convergent behavior that can be observed are oscillatory convergence and divergence and monotonic divergence. To determine what type of behavior is encountered using a set of three solutions, the discriminating ratio [24] can be used

$$R = \frac{f_1 - f_2}{f_2 - f_3} \tag{1.2}$$

where 1 is the finest mesh and 3 is the coarsest mesh. The "apparent" convergence behavior can then be classified using the following conditions.

1. Monotonic convergence: $0 < R < 1$
2. Oscillatory convergence: $R < 0$ and $|R| < 1$
3. Monotone divergence: $R > 1$
4. Oscillatory divergence: $R < 0$ and $|R| > 1$

Richardson Extrapolation and Generalized Richardson Extrapolation

Richardson extrapolation is used to build error estimators and error bands (uncertainty bands) of discretization error for systems described by partial differential equations (PDE) [21]. This is through the usage of estimating an exact solution of the quantity of interest. The Richardson Extrapolation was originally based on a 2^{nd} order numerical scheme involving grid refinements of 2. Without rigorous derivation, the Richardson extrapolated solution can be found using the following,

$$f_{exact} = f_1 + \frac{f_1 - f_2}{3} \tag{1.3}$$

where f_1 and f_2 are the fine and coarse solutions.

The extrapolation solution from the above is considered 3^{rd} order accurate but can be extended to 4^{th} order accuracy. This scheme depends on uniform grid refinement and that

all levels (meshes) of refinement are in the asymptotic range. The formal order of accuracy (p_f) is order of the leading truncation term that dominates the error of the numerical prediction and an exact solution (i.e. 2^{nd} order accuracy). In order to use a generic p_f and a refinement (factor) that is not restricted to 2, GRE can be presented as,

$$f_{exact} = f_1 + \frac{f_1 - f_2}{r_{12}^p - 1} \tag{1.4}$$

where r_{12} is (using h as the uniform grid size). It is defined as

$$r_{12} = \frac{h_2}{h_1} \tag{1.5}$$

Other Forms of Determining Extrapolated Solution

Due to the issues associated with reaching an asymptotic range, alternate methods discussed and proposed for use by Celik et. al. ([25], [26], [27], [28]) to calculate an extrapolated value for oscillatory convergence. These methods include the polynomial method, power law method, cubic spline method, and Appropriate Error Spline (AES) with the last one being the most promising. Though, these methods will not be pursued for usage in this work and left for future studies.

Observed Order of Accuracy

For situations where the exact solution is not known (i.e. most CFD analysis), an observed order of accuracy (as opposed to the formal) can be approximated using at least three meshes (referred to as a mesh triplet). One could use the formal order of accuracy, but it would be viewed as more of a guess or estimate and not properly reflective of the discretization error. For three meshes with equal refinement factors between each meshing level, the equation 1.6 can be used.

$$p = \frac{ln\left(\frac{f_3 - f_2}{f_2 - f_1}\right)}{ln(r)} \tag{1.6}$$

For unequal refinement factors between successive meshes, the observed order of accuracy (P) can be estimated using equation 1.7.

$$\frac{f_2 - f_1}{r_{12}^p - 1} = r_{23}^p \frac{f_3 - f_2}{r_{23}^p - 1} \tag{1.7}$$

where f_1 would be the finest mesh and f_3 is the coarsest mesh. This equation has to be solved using a simple iterative method where the initial guess is usually based on the formal order of accuracy.

In the case of simulations conducted with unstructured meshing and a constant refinement, the following equation can be used to definite a representative refinement factor.

$$r_{12} = \left(\frac{N_1}{N_2}\right)^{\frac{1}{D}} \tag{1.8}$$

where N is the total number of degrees of freedom (D.O.F.) for the specific mesh level and D is the dimension of the simulation.

Based on the discussions by Roache [22], it can be inferred that mesh convergence can be determined using the observed order of accuracy assuming each mesh in the asymptotic region and does not violate any baseline assumptions. This can be done by using the solutions for a mesh triplet or several mesh triplets (if available) to determine if the observed order of accuracy is consistent with the formal order. This leaves a few questions such as, "What is considered a parameter indicative of global behavior of the mesh?", "What is the metric to determine the observed order is 'close enough' to the formal order?", and "What can be done in situations where asymptotic regions are feasible or the underlying assumptions are violated?"

1.3.2 Mesh Sensitivity

Mesh sensitivity in the CFD community is still relatively new due to a variety of factors. For instance, one telling point is the majority of the community does not even consider mesh sensitivity (based off the definition above) to be a standard part of a CFD analysis. Very rarely are error or uncertainty bands provided with any meaningful quantities shown in CFD analysis. There are several means to create error bands based on L^2 norms, GCI, and GCI variants which have associated pros and cons.

L^2 Norm

The L^2 norm has been historically used to show the reduction of error with decreasing mesh size (increasing D.O.F.) due to giving an indication of global behavior. The L^2 or "Euclidean norm" or root mean square value is defined as

$$L^2 = \left(\frac{1}{N} \sum_{n=1}^{N} f_i^2 \right)^{\frac{1}{2}} \tag{1.9}$$

where the L^2 norm error can be defined as

$$Error_{L^2} = \left(\frac{1}{N} \sum_{n=1}^{N} (f_i - \overline{f})^2 \right)^{\frac{1}{2}} \tag{1.10}$$

$\overline{f}$ is the average quantity of interest or the exact solution of a PDE. L^2 norm could be a decent metric for determining sensitivity, but Roache [22] argues against it. This is due to L^2 norm not taking into account mesh information (refinement factor) and observed order of accuracy.

Grid Convergence Index

Roache [22] originally proposed GCI to develop uncertainty bands using a posterior information of any meaningful quantities, the mesh information (refinement factor), and

observed order of accuracy. The observed order of accuracy is the order of accuracy determined using an a posteriori estimate based off the mesh information and corresponding meaningful quantities. GCI is based off GR) and the suffers from the same deficiencies found below.

1. The simulations have to be shown to be in a region of asymptotic convergence.

2. The mesh and mesh refinement must be done in a uniform and consistent manner.

3. Localized areas of refinement can not be used.

GCI for a mesh triplet can be calculated as a relative quantity for the finest mesh using the following equation,

$$GCI_{12} = \frac{F_s}{r_{12}^p - 1} \left| \frac{f_2 - f_1}{f_1} \right| \tag{1.11}$$

where F_s is the factor of safety. When the quantities are close to zero, the absolute quantity GCI is calculated without the normalization [29].

$$GCI_{12} = \frac{F_s}{r_{12}^p - 1} |f_2 - f_1| \tag{1.12}$$

The medium mesh can then be calculated using the solutions for the coarse and medium meshes. The factor of safety is usually selected to be 1.25 or 3.0 depending on the following.

1. $F_s = 3.0$, if only two grids are used.

2. $F_s = 1.25$, if a grid triplet is used and the observed order of accuracy is considered to match the formal order of accuracy.

The factor of safety is still an open question with work conducted by Xing and Stern [30] to address issues when the observed order of accuracy is larger than the formal order and others. Roache [31] and Xing [32] had an exchange where Xing and Stern revised their original discussed approach and it is solely included for completeness and not included in the current study.

The deficiencies of this method are quite restrictive considering most CFD analysis include turbulence, wall regions, localized refinement, unstructured grids, and are not found to be in an asymptotic range. Roache struggles to justify the usage of GCI in turbulence based on his comments [24], "By creating the words 'laminar' and 'turbulent' and using them in juxtaposition, we can deceive ourselves into thinking that they have equal weight and meaning. In fact 'laminar' means something, but 'turbulent' does not define the condition." These comments, in the author's opinion, undermine the argument that GCI should be aggressively pursued for turbulent CFD analysis which are the vast majority of current CFD analysis. The requirement against localized meshing supports this due the need for localized near wall refinement to resolve boundary layer behavior through near wall functions. Localized areas of refinement may also be needed to resolve key areas of gradients to be within the available computational resources. Further, the majority of CFD analysis found in industrial and research environments can not be done without the assistance of unstructured meshes. Finally, the determination of the observed order of accuracy using a global or local quantity is not well commented and is without consensus. It is up to the CFD analyst to determine the best approach possible which can lead to pitfalls for even the most experienced CFD analysts.

Least Squares - Grid Convergence Index

There are several forms of GCI developed in an attempt to address simulations conducted outside the asymptotic region. The most prominent being the Least Squares GCI

(LS-GCI or LSQ-09) by Eca [33], which involves minimizing an error function involving observed order of accuracy, solution of a function at some point, grid spacing, and others. An improved version (LSQ-10) was proposed and discussed in detail by Phillips [34] and Eca [35] which added more complexity but overcame some of the deficiencies of the previous. It suffers from the requirement of at least four meshes are needed which maybe unobtainable in large enough cases.

There are potentially other variants meant to overcome issues with non-asymptotic convergence with a direct estimate of error bands, but at the time of writing this was the most prominent one found.

1.4 Solution Validation

Solution validation for CFD is commonly based on the accuracy of the simulation results as compared to the experiment [29]. The validation can be in several forms including basic color maps, single data points and line profiles with or without error bars shown. Traditionally, solution validation in CFD is shown as the simple graphical comparison of the two results without error bars. This is due to a variety of factors but different forms are needed based on the extent of validation desired. For instance, an analyst may only find experimental data that is not well documented with regards to measurement error and uncertainty. It is better for them to at least have some comparison even if it isn't the best situation possible.

In general and strongly suggested by Roache [24], solution verification should occur before solution validation. Fortunately, solution verification allows the analyst to construct error bands based on the previously mentioned methods. Using that information, we can compare the experimental measurements with their associated error bands, Standard Error of the Mean (SEM), and the simulation results. If the error/uncertainty bands overlap, the measurements are suggested to agree within the uncertainty bands. This is a simple

method for validation and is well accepted for comparing two measurements of the same quantity. In this case, the simulation results are treated as a measurement of the same quantity of interest with GCI [36], [24] or two times the $Error_{L^2}$ acting as the 95% confidence interval based on a normal distribution for the reported quantity. The caveat being that the GCI and $Error_{L^2}$ do not include uncertainty attributed to boundary conditions, initial conditions, and others and solely attributed to discretization error. Additionally, a direct comparison between the experiment and simulation results can be shown as percent difference calculated as,

$$\%Diff = \left| \frac{U_1 - U_2}{\frac{U_1 + U_2}{2}} \right| \tag{1.13}$$

to show a quantification of the difference between the two reported quantities. This is if the magnitudes of the quantities are large enough to not cause artificially large differences. In cases such as this, absolute difference based off the definition below can be used.

$$Abs_{diff} = |f_n - f_{exp}| \tag{1.14}$$

Using the aforementioned validation comparison, the CFD simulations should be able to be determined if they are considered validated. This is only for the specific calculation and the stipulations surrounding it. Such that a CFD analyst does not attempt to try and claim calculations are validated for flow over a flat plate is now validated for flow in a complex reactor geometry.

1.5 Governing Physics

1.5.1 Turbulent Free Shear Planar Jets

The turbulent free shear planar jets (see figure 1.7) can be described using the boundary layer equations for free shear flow.

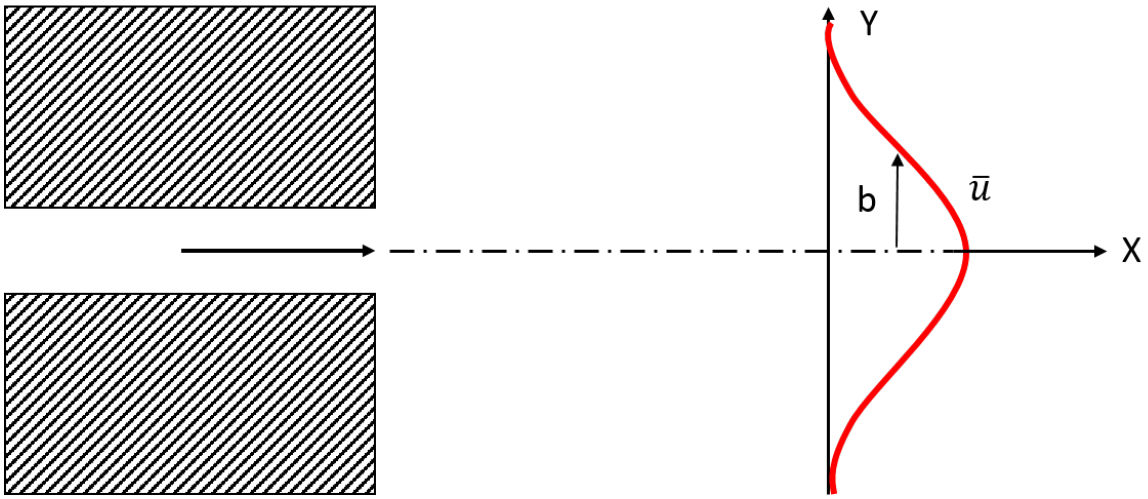

Figure 1.7: Schematic of Turbulent Planar Jet

To get there we start with the RANS equation in a 3-D form beginning with the continuity equation,

$$\frac{\partial \overline{u}}{\partial x} + \frac{\partial \overline{v}}{\partial y} + \frac{\partial \overline{w}}{\partial z} = 0 \tag{1.15}$$

where $\overline{u}$, $\overline{v}$, $\overline{w}$ are the streamwise and spanwise velocity components. The momentum (Reynolds) equations for x, y, and z components are,

$$\frac{\partial \overline{u}}{\partial t} + \overline{u}\frac{\partial \overline{u}}{\partial x} + \overline{v}\frac{\partial \overline{u}}{\partial y} + \overline{w}\frac{\partial \overline{u}}{\partial z} = -\frac{1}{\rho}\frac{\partial \overline{P}}{\partial x} + \nu\nabla^2\overline{u} - \left(\frac{\partial \overline{u'^2}}{\partial x} + \frac{\partial \overline{u'v'}}{\partial y} + \frac{\partial \overline{u'w'}}{\partial z}\right) \tag{1.16}$$

$$\frac{\partial \overline{v}}{\partial t} + \overline{u}\frac{\partial \overline{v}}{\partial x} + \overline{v}\frac{\partial \overline{v}}{\partial y} + \overline{w}\frac{\partial \overline{v}}{\partial z} = -\frac{1}{\rho}\frac{\partial \overline{P}}{\partial y} + \nu\nabla^2\overline{v} - \left(\frac{\partial \overline{u'v'}}{\partial x} + \frac{\partial \overline{v'^2}}{\partial y} + \frac{\partial \overline{v'w'}}{\partial z}\right) \tag{1.17}$$

$$\frac{\partial \overline{w}}{\partial t} + \overline{u}\frac{\partial \overline{w}}{\partial x} + \overline{v}\frac{\partial \overline{w}}{\partial y} + \overline{w}\frac{\partial \overline{w}}{\partial z} = -\frac{1}{\rho}\frac{\partial \overline{P}}{\partial z} + \nu\nabla^2\overline{w} - \left(\frac{\partial \overline{u'w'}}{\partial x} + \frac{\partial \overline{v'w'}}{\partial y} + \frac{\partial \overline{w'^2}}{\partial z}\right) \tag{1.18}$$

where $\overline{u'^2}$, $\overline{v'^2}$, $\overline{w'^2}$ are the Reynolds normal (diagonal) stresses and $\overline{u'v'}$, $\overline{u'w'}$, $\overline{v'w'}$ are the

Reynolds shear (off-diagonal) stresses.

The turbulent planar jets are by definition 2-D which results in the $\overline{w}$ spanwise component terms of the RANS equations to disappear. In this case, we are looking at steady behavior which reduces all time dependent terms to zero and results in the following equations for continuity and momentum.

$$\frac{\partial \overline{u}}{\partial x} + \frac{\partial \overline{v}}{\partial y} = 0 \tag{1.19}$$

$$\overline{u}\frac{\partial \overline{u}}{\partial x} + \overline{v}\frac{\partial \overline{u}}{\partial y} = -\frac{1}{\rho}\frac{\partial \overline{P}}{\partial x} + \nu\nabla^2\overline{u} - \left(\frac{\partial \overline{u'^2}}{\partial x} + \frac{\partial \overline{u'v'}}{\partial y}\right) \tag{1.20}$$

$$\overline{u}\frac{\partial \overline{v}}{\partial x} + \overline{v}\frac{\partial \overline{v}}{\partial y} = -\frac{1}{\rho}\frac{\partial \overline{P}}{\partial y} + \nu\nabla^2\overline{v} - \left(\frac{\partial \overline{u'v'}}{\partial x} + \frac{\partial \overline{v'^2}}{\partial y}\right) \tag{1.21}$$

In this flow, we have a much larger streamwise component of velocity for the majority of the jet which allows for the assumption of the spanwise velocity component to be negligible. The gradients of the stress terms are reduced by the gradient terms in the spanwise direction being much larger than the x direction allowing these terms to be considered negligible. This results in the equations being of the following form.

$$\frac{\partial \overline{u}}{\partial x} + \frac{\partial \overline{v}}{\partial y} = 0 \tag{1.22}$$

$$\overline{u}\frac{\partial \overline{u}}{\partial x} + \overline{v}\frac{\partial \overline{u}}{\partial y} = -\frac{1}{\rho}\frac{\partial \overline{P}}{\partial x} + \nu\frac{\partial^2\overline{u}}{\partial^2 y} - \left(\frac{\partial \overline{u'^2}}{\partial x} + \frac{\partial \overline{u'v'}}{\partial y}\right) \tag{1.23}$$

$$0 = -\frac{1}{\rho}\frac{\partial \overline{P}}{\partial y} - \frac{\partial \overline{v'^2}}{\partial y} \tag{1.24}$$

Then by taking the equation 1.24 and integrating to a point outside the mean flow, we can get the following equation for pressure using p_∞ as the free stream pressure.

$$\overline{P} = p_\infty - \rho\overline{v'^2} \tag{1.25}$$

After which, we can then substitute equation 1.25 into equation 1.23 after differentiating with respect to the streamwise direction to get the following.

$$\overline{u}\frac{\partial\overline{u}}{\partial x} + \overline{v}\frac{\partial\overline{u}}{\partial y} = -\frac{1}{\rho}\frac{\partial p_\infty}{\partial x} + \nu\frac{\partial^2\overline{u}}{\partial^2 y} - \left(\frac{\partial\overline{u'v'}}{\partial y} + \frac{\partial}{\partial x}(\overline{u'^2} - \overline{v'^2})\right) \tag{1.26}$$

The last term in equation 1.26 is quite small and will be ignored but not entirely negligible ([37]). Also, p_∞ is written as $\overline{p}$ for simplicity to get the boundary layer momentum equation for turbulent free shear planar jet flow.

$$\overline{u}\frac{\partial\overline{u}}{\partial x} + \overline{v}\frac{\partial\overline{u}}{\partial y} = -\frac{1}{\rho}\frac{\partial p_\infty}{\partial x} + \nu\frac{\partial^2\overline{u}}{\partial^2 y} - \left(\frac{\partial\overline{u'v'}}{\partial y}\right) \tag{1.27}$$

For the following discussions, the free shear region of flow results in a significantly larger turbulent shear stress than laminar shear stress. This results in the second term on the right side in the above equation to be assumed negligible and the following relationship is used $\tau = -\overline{u'v'}$. Also, the pressure gradient in the streamwise direction is considered negligible leading the final equation set used for analytical solutions discussed later.

$$\frac{\partial\overline{u}}{\partial x} + \frac{\partial\overline{v}}{\partial y} = 0 \tag{1.28}$$

$$\overline{u}\frac{\partial\overline{u}}{\partial x} + \overline{v}\frac{\partial\overline{u}}{\partial y} = \frac{1}{\rho}\frac{\partial\tau}{\partial y} \tag{1.29}$$

A more guided discussion of this deviation can be found in the seminal book by Rajaratnam [38].

1.5.2 Self-Similarity/Self-Preserving Quantities

Before diving further into turbulent planar jets, the concept of self-similarity (also referred to as self-preserving) for turbulent flows needs to be discussed [37]. Pope provides a summary of self-similarly by supposing there exists a generic function $Q(x, y)$ depends on two independent variables such as two directions (x and y). The generic function can have two characteristic scales associated with it that are dependent on x, $Q_0(x)$ and $\delta(x)$. Both of these scales are independent of the y direction. We can then define new scaled variables such as

$$\xi = \frac{y}{\delta(x)} \tag{1.30}$$

$$\widetilde{Q}(\xi, x) \equiv \frac{Q(x, y)}{Q_0(x)} \tag{1.31}$$

Using these, we can look at what it means if there exists a function $\widehat{Q}(\xi)$ that is independent of x. If this function does exist then the following holds true,

$$\widetilde{Q}(\xi, x) = \widehat{Q}(\xi) \tag{1.32}$$

This implies that Q(x,y) is self-similar. The following comments and qualifications are particularly relevant for the proceeding discussion.

- The characteristic scales, $Q_0(x)$ and $\delta(x)$ must be chosen in a sensible manner.
- Self-similar behavior may only exist and be observed over a range of x.
- A partial differential equation is the governing form of the generic function $Q(x, y)$ but ordinary differential equations are the governing forms of $Q_0(x)$ and $\delta(x)$.

Self-Similar/Self-Preserving Turbulent Planar Jet

The ideal turbulent free shear planar jet can be described by the characteristic velocity $U_0(x)$ which is the centerline streamwise velocity. The characteristic scale is set as the half-width height, b (figure 1.10), where $u(x, b) = \frac{1}{2}u_0(x)$. The following conditions based on the discussion in subsection 1.5.1 are needed for self-similarity.

1. The streamwise component of the flow has to be much larger than the spanwise components.

2. The streamwise and spanwise (y) component of velocity and resulting statistical flow quantities are independent of the spanwise (z) direction.

3. The flow behavior such as streamwise velocity and statistical flow quantities encounter symmetry on the x axis.

4. The geometric ratio of $\frac{H}{w}$ is large enough to be free of end effects from the duct sides (see figure 1.8) and effectively 2-D in the centerline profile of the jet.

These conditions are used during the derivation of the two analytical turbulent free shear planar jet profiles and useful for the analysis in the latter chapters.

1.5.3 Analytical Velocity Profile Solutions for Turbulent Planar Jets

Tollmien Solution

The Tollmien solution to the turbulent free shear planar jet is approached using the boundary layer equations 1.28 and 1.29 and the Prandtl mixing length hypothesis. The hypothesis allows the Reynolds stress tensor τ to be related to the velocity gradient by a mixing length l_m characteristic of the flow geometry. This relationship is shown by the following,

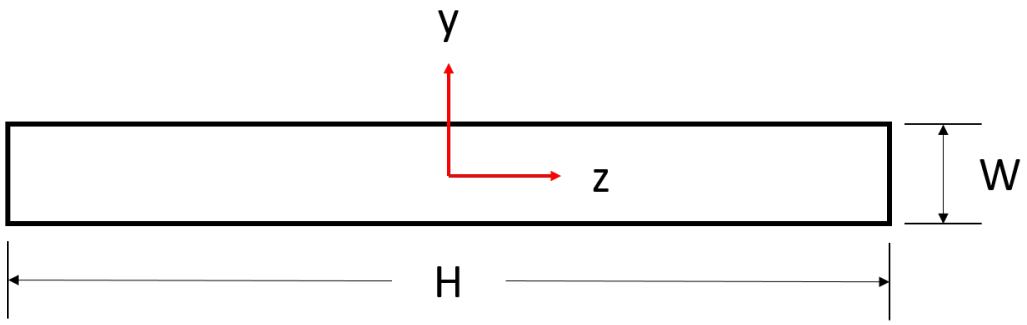

Figure 1.8: Schematic of a Duct

$$\tau = \rho l_m^2 \left(\frac{\partial \overline{u}}{\partial y} \right)^2 \tag{1.33}$$

where l_m is related to the flow by defining it as proportional to the jet half-width height, b. Using b, the similarity variable η is defined as $\eta = \frac{y}{b}$. These relationships are used to result in a non-linear second-order differential equation,

$$F''^2 + FF' = C \tag{1.34}$$

where F' is equal to $\frac{\overline{u}}{\overline{u_0}}$. The solution of this was originally determined numerically by Tollmien and is shown in figure 1.9.

Goertler Solution

The Goertler solution to the turbulent free shear planar jet is approached using the boundary layer equations 1.28 and 1.29 and the Prandtl turbulent shear stress equation (equation 1.35.

$$\tau = \rho \epsilon \left(\frac{\partial \overline{u}}{\partial y} \right) \tag{1.35}$$

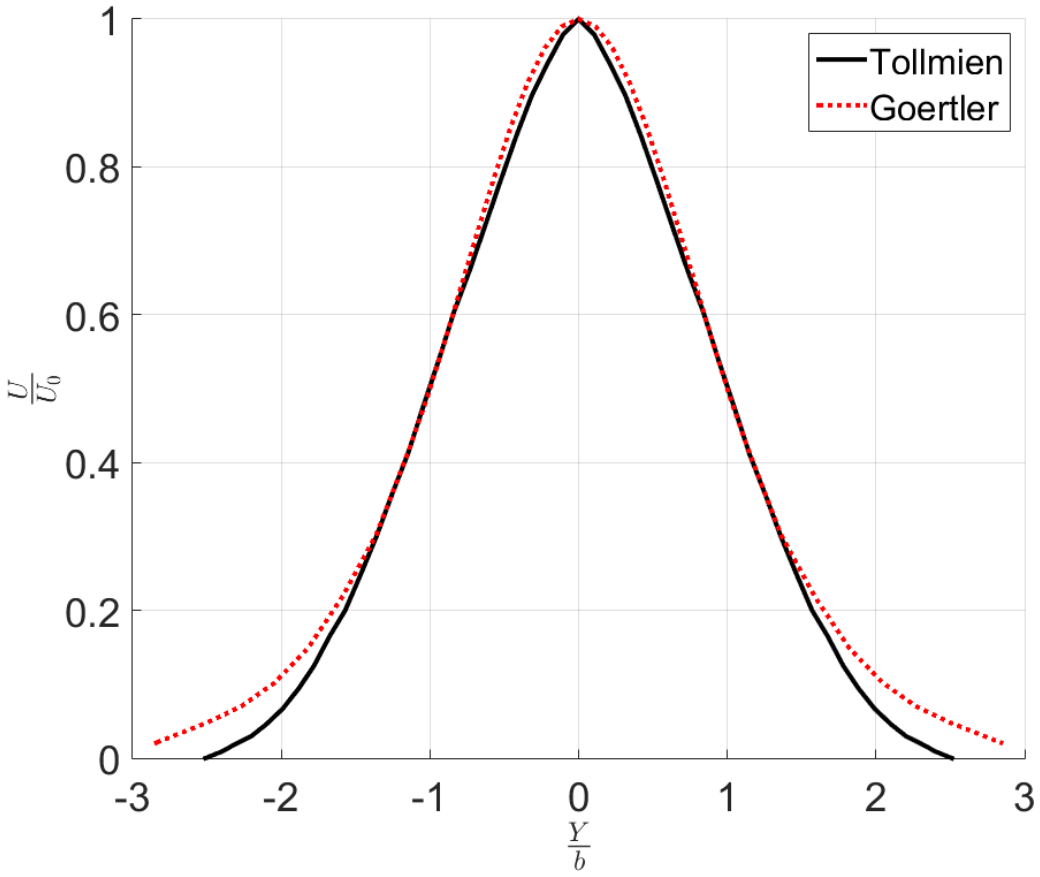

Figure 1.9: Analytical Solutions for Planar Turbulent Jet

where ϵ is the turbulent viscosity. The turbulent viscosity is proportional to the $\overline{u_0}$ and b that allows the following equation to result,

$$F^2 + F' = C \tag{1.36}$$

where F' is again equal to $\frac{\overline{u}}{\overline{u_0}}$ and C is a constant. The resulting analytical solution for F' is then shown in figure 1.9.

1.5.4 The Turbulent Planar Jet Experiments

The turbulent free shear planar jet (figure 1.10) has been investigated extensively by several groups found in the literature. Although previous work had been conducted before hand, Bradbury [6] and Heskestad [39] provided the first sets of comprehensive measurements of the turbulent planar jet using HWA and static pressure measurements (Pitot and static tubes). These two groups measured the mean and fluctuating velocities, turbulent intensities, Reynolds stresses, and higher order moments of the flow. Bradbury found that for their setup, self-similarly is achieved by thirty jet nozzle widths from the injection point.

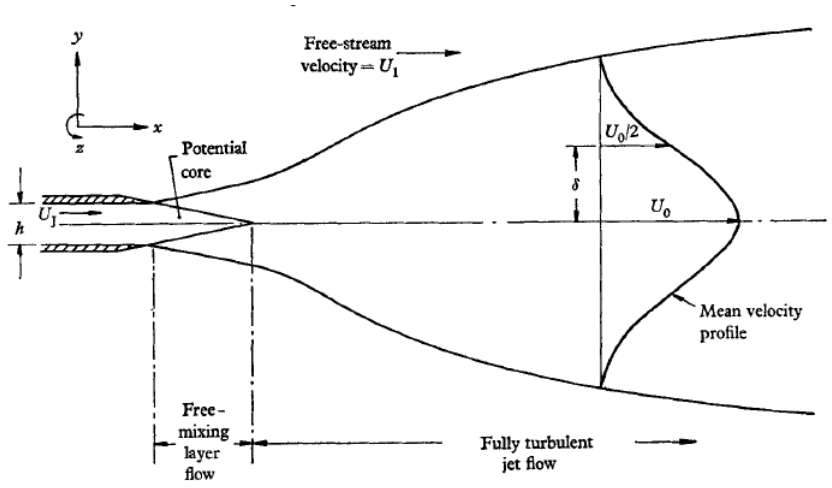

Figure 1.10: Schematic of Turbulent Planar Jet [6]

Whereas, Heskestad found their jet reached self-similarly of the streamwise velocity and turbulent fluctuations around sixty-five jet nozzle width from the injection point. The motion of jet corresponding to the largest eddies (turbulent dissipation) was found to become self-similar much later around one hundred jet nozzle widths. The differences found relating to self-similarly are due to the different initial conditions. Such as Bradbury's inlet

profile was likely more similar to a "top-hat" whereas Heskestad was closer to a channel flow profile (see figure 1.11).

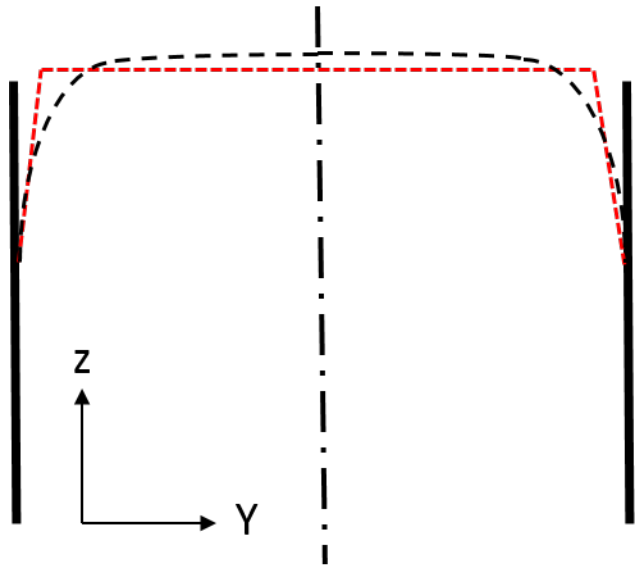

Figure 1.11: Top Hat (Red) vs. Channel Flow (Black) Velocity Profiles

Bradbury's experimental set up was also injected into free stream conditions that was 0.16 of the exhaust jet velocity. This was discussed in greater detail by Gutmark and Wygnanski [40]. Gutmark and Wygnanski's effort was focused on determining the structure of turbulent free shear flows. They conducted experiments on mixing layer, axisymmetric jet, and planar jets and found that the latter two were similar. Although, all three flows were found to be anisotropic in nature which impacts modeling assumptions involving isotropy for the Boussinesq eddy viscosity assumption. The planar jet was found to become self-similar at forty jet widths from the injection point.

1.5.5 Twin Jets

Previous Experimental Efforts

The first investigations into twin planar jets converging into one were done by Miller and Comings [41]. Using Hot-Wire Anemometry (HWA) and static pressure disk probes, Miller and Comings were able to determine that a sub-atmospheric static pressure region was pulling the jets together. They found after merging together, the single jet behavior was similar to that of a single free jet. In Tanaka's first report [42], they discuss the entrainment of fluid surrounding the twin jets causing the sub-atmospheric pressure region (later referred to as converging region) to develop. In this early work, they look at the effect of the separation distance between the jets on various jet parameters using HWA and static pressure disk probes. In particular, the free stagnation point (later referred to as merge point) is depending on the ratio of the separation distance between the centerline of the two jets over the jet width. If the ratio becomes larger, the free stagnation point is further away from the injection point of the jets. In the second report by Tanaka [43], the work focused on the region of the combined single jet (later referred to as the combined region) using the same experimental apparatus previously mentioned. Tanaka determined that regardless of the separation distance over nozzle width ratio ($\left(\frac{S}{d}\right)$ in figure 1.13), the combined jet will have good agreement with Goerter's single jet curve [38].

They did find the combined jet will not be observed to have the same turbulent intensity profile as a true single jet. Further, the combined jet will spread similarly to a single jet which is a linear relationship between jet half-width and downstream distance. Tanaka also found that the Reynolds number did not have an effect on the combining physics of the twin jets. The flow solely depends on geometry of the nozzles for a fully turbulent twin jet. The previously discussed work were conducted in environments considered to be "unventilated" due to the jets being injected perpendicular to a solid plane. An example of

ventilated and unventilated jets are shown in figure 1.12

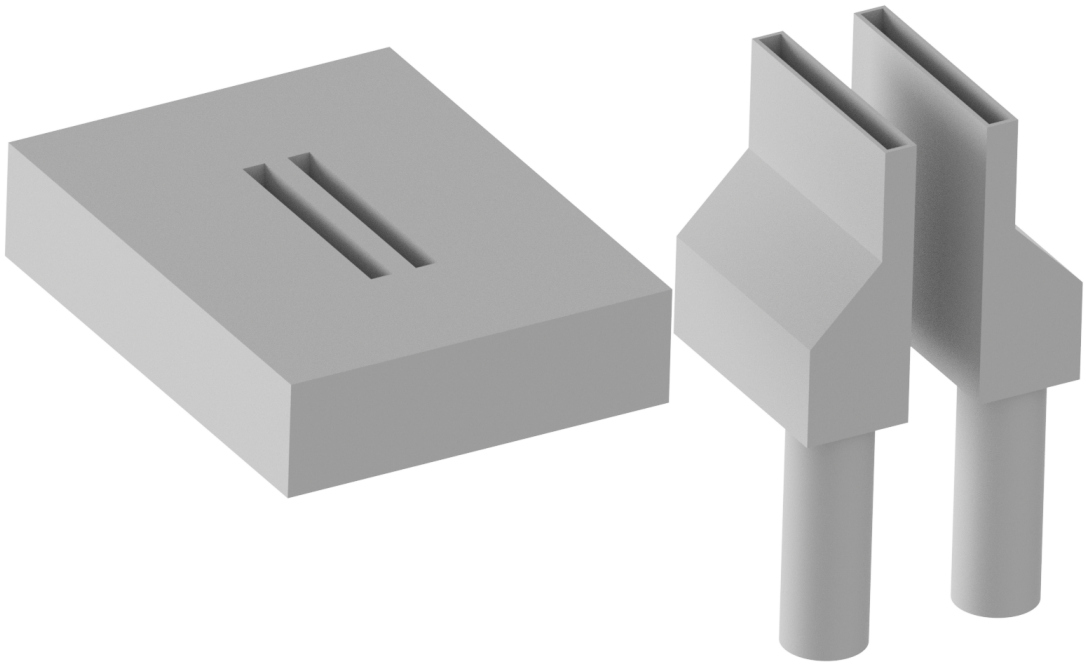

Figure 1.12: An example of Twin Planar Jets that are Unventilated (left) and Ventilated (right)

In work conducted by Marsters [44] using HWA and static pressure probes, they conducted the same twin planar jet in a "ventilated" experimental setup where the solid plane does not exist. This was done in an effort to simulate conditions similar to that of an aircraft. Marsters found that there is little impact of an environment that is considered unventilated or ventilated on the mean flow behavior discussed previously. Marsters do support the conclusion by Tanaka that the behavior is effectively independent of Reynolds number assuming the jets are undergoing fully developed turbulence. Elbanna et. al. conducted a similar experimental campaign to that of Marsters to capture turbulence fluctuations in ventilated twin planar jets using HWA [45]. Elbanna et. al. confirmed the observations of

Marsters while determining some properties of ventilated jets are not exactly the same as a single jet. In the work by Lin and Sheu [46], they used HWA to investigate similar qualities to discussed previously. They observed the twin jets and later combined jet exhibit self-preserving behavior of the mean streamwise velocity in the converging and combined regions. The turbulent intensities, and Reynolds shear stresses are not observed to be self-similar except in the combined region. Whereas, the flow behavior in the merging region is not considered self-preserving. It is in this work, that the terms merge and combined points, converging, merging, and combined regions are seemingly defined which is used exhaustively in later studies. Ko and Lau [8] used HWA to comprehensively investigate the converging and merging regions of partially vented (a bluff body/separation plate separated the two jets) two planar-like turbulent jets for identifying the flow structures in water. This work is similar to the experimental efforts shown in chp 2 but has a much smaller aspect ratio $\left(\frac{H}{w}\right)$, smaller separation ratio $(\frac{S}{a})$, and significantly lower Reynolds number based on duct width. Ko and Lau were able to obtain a results of the streamwise flucations, spanwise fluctations, and the off-diagonal Reynolds stresses in the converging and merging regions.

Unlike previous studies, Nasi and Lai measured twin planar jets using LDV as opposed to HWA [47]. They observed similar behavior to previous studies and further observed the independence of flow behavior from Reynolds number.

Summarized Twin Jet Physics

The proceeding discussions regarding the twin jet will follow the vernacular of Anderson and Spall [7]. Figure 1.13 provides an schematic of the flow features notable of the twin jets when combining together. The behavior is characterized by three regions that will be referred to as the converging, merging, and combining regions. The converging region starts from the point of the injection of the jets to the merge point of the jets. The

merge point is defined in this study as the point where the centerline streamwise velocity flips from negative to positive or considered zero. The merging region exists from the merge point till the combined point. The two jets progress towards becoming a single jet in this region. The combined point is defined as the point corresponding the maximum centerline streamwise velocity. After the combined point, the single jet is encountering the combined region where the jet exhibits self-preserving and self-similar behavior similar to a true single jet.

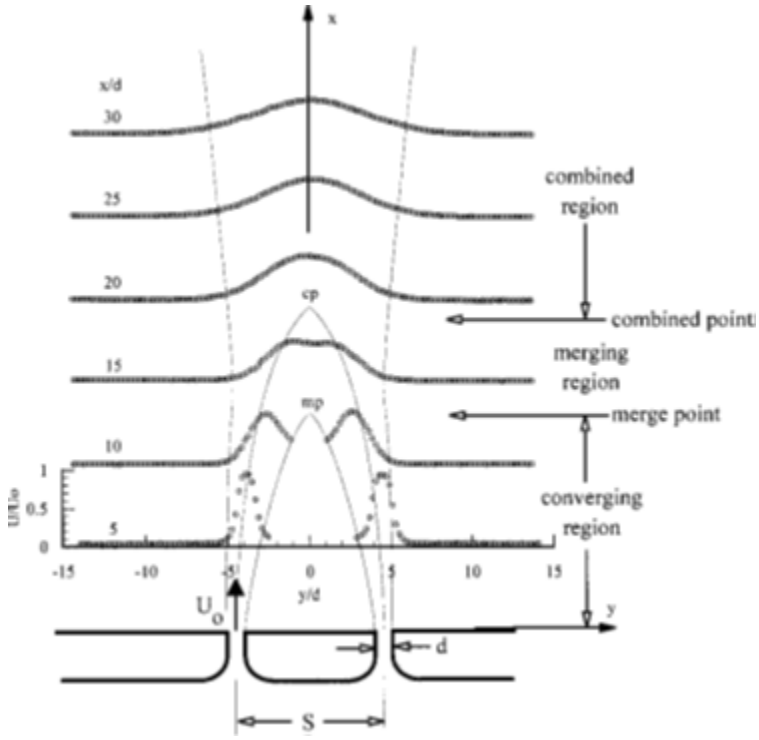

Figure 1.13: Schematic of Twin Slotted Jets Merging into One Jet [7] where $d = a$ for this study

The twin planar-like turbulent jets have a Reynolds stress $\overline{uv}$ distribution similar to figure 1.14 for the merging and converging regions of flow. This is This information

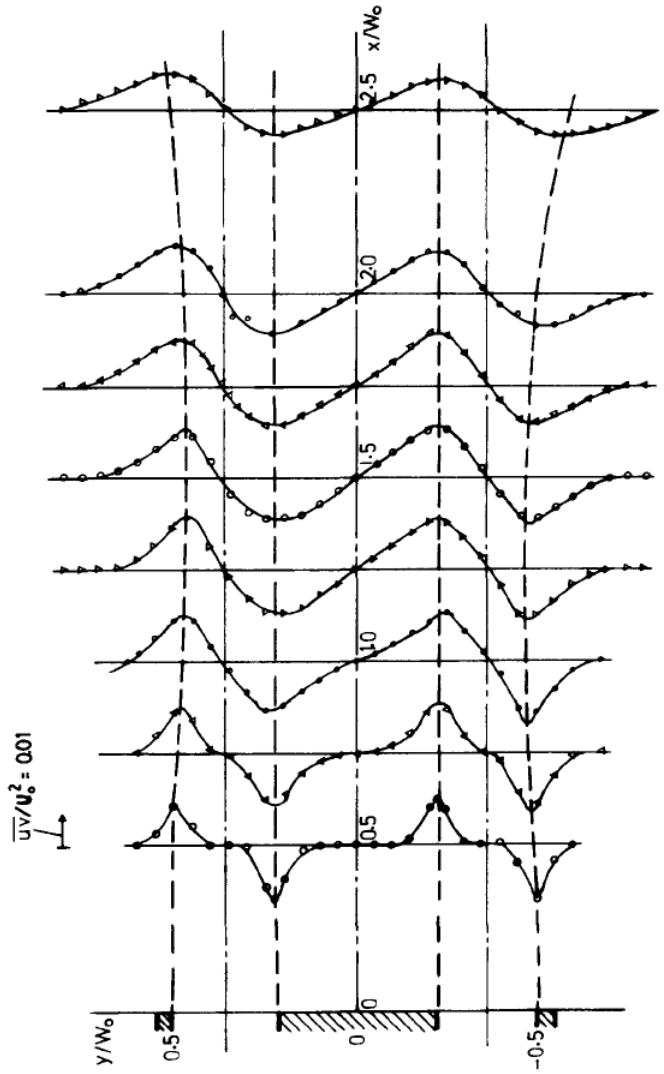

Figure 1.14: Example of Reynolds Stress $\overline{uv}$ Components in Partially Vented Twin Planar-Like Jet [8]

provides useful insight for the solution validation in chapter 5 to ensure the appropriate Reynolds stress distributions are being captured.

Previous CFD Validation Efforts

An initial effort to do basic CFD validation was done by Behrouzi and McGuirk using a RANS framework (not stated whether steady or unsteady) with a high Reynolds number $\kappa - \epsilon$ turbulence model [48]. This work is seemingly disconnected from the rest of the literature on twin planar jets. This is likely due to the focus twin jets impinging into a weak to strong crossflow. In their work, Behrouzi and McGuirk do a sample case test case where no crossflow is experienced and is compared qualitatively to the CFD predictions. They found that RANS with a high Reynolds number $\kappa - \epsilon$ turbulence model can predict the gross features of the twin jets.

Anderson and Spall conducted an experimental and CFD validation campaign for twin planar jets based off guidance of previous studies [7]. In this work, they gathered experimental data using HWA of the centerline streamwise velocity and Reynolds stresses for different $\left(\frac{H}{w}\right)$ ratios. They compared this experimental data to CFD simulations using a 2-D steady RANS framework with the standard $\kappa - \epsilon$ and Reynolds Stress turbulence (RSM) models using Fluent V 4.4. Anderson et. al. found the standard $\kappa - \epsilon$ and RSM simulations were able to capture the time averaged centerline streamwise velocity as compared to the experiment. They did note the RSM model over-predicted the peak velocities while the standard $\kappa - \epsilon$ model either directly captured it or slightly under-predicted the peak for four different separation distance over nozzle width ratios. The authors found the CFD results of velocity profiles in the merging and combined regions predicted a faster merging of the two jets. For the merge points, the two CFD predictions were found to compare well to their experimental results and previous investigations of other authors. Anderson et. al. did know the RSM prediction of merge points was slight higher than the standard $\kappa - \epsilon$ model. For the combined point, the authors found a significant amount of scatter for any given separation distance over nozzle width ratio between all available and applicable

data. They determined the reasoning behind the scatter is due to upstream effects of the separate experimental facilities used. This is asserted by the authors to apply to both merge and combined points.

Lastly, Anderson et. al. found the Reynolds stress components in the streamwise and spanwise components of the RSM and experiments to be in decent agreement. Two points to note about this analysis, the mesh convergence analysis was quite limited (based solely on centerline streamwise velocity) and the experimental uncertainty was not shown. This implies the results have to be considered carefully. For both studies discussed in this section, the specific references for their turbulence models were not appropriately listed. Both studies do not make any note of the vorticity profiles which can indicate mesh resolution issues.

1.6 Objectives of Current Study

The objectives of this work are as follows:

1. What can be considered a simple quantitative and qualitative means of determining mesh convergence for meshes of high unstructured and/or specific area refined meshes?

2. What currently proposed method using discretization error to calculate uncertainty/error bands is generalized enough for high unstructured or specific area refined meshes?

3. What is a suitable way to show solution validation and can it involve uncertainty/error bands?

4. Are these current metrics easy to implement for solution validation and if not, can they be simplified?

2. TWIN JET WATER FACILITY EXPERIMENTS

The Twin Jet Water Facilty (TJWF) and some of the experimental campaigns are largely the focus of this dissertation. The Twin Jet Water Facilty (TJWF) created by the University of Tennessee, Knoxville (UTK) is being used for on-going studies of many purposes. It was originally developed for testing different types of fluid and heat transfer instrumentation (ultrasonic velocimetry (UVP) and thermocouple rakes, thermal imaging cameras) for opaque fluids such liquid sodium [49]. It included a complementary CFD component to help design and do basic validations studies with. This was in an effort to aide the development of sodium fast reactor instrumentation and monitoring technology. The original experimental campaign was intended to have both a scaled water and liquid metal (mercury) test facilities. The instrumentation was going to be tested in both facilities to understand the potential measurement issues related to using a fluid other than water.

The TJWF was later re-purposed for a variety of studies including the development of experimental databases for CFD V&V efforts. This campaign has become the focus of the American Society of Mechanical Engineering (ASME) V&V symposium recent benchmark and challenge workshops.

2.1 TJWF Design and Dimensions

The TJWF consists of the mixing tank and external piping/pumps. The mixing tank is placed on top of a movable cart that can be used for local transport. It can be removed from the cart in the case of moving across country (i.e. from UTK to TAMU). The mixing tank is made up of 25.4 mm (1 inch) thick acrylic sheets glued together allowing for an almost completely transparent measurement volume. The mixing tank is comprised of the jet head and weir overflows. The jet head contains the two separated rectangular vertical jets and the stagnation boxes that feed into the jets. The TJWF is shown in Figure 2.1 with

the mixing tank, movable cart, and piping/pumps. The TJWF's two jets are feed by two 186.43 watt (0.5 Hp) pumps that suction from separated header tanks. Each piping line feeding a separate jet from the header tanks through the pumps includes a throttling valve for volumetric flow control and an isolation valve. The two header tanks are connected by a common piping line includes a value that allows isolation between the header tanks. The water in the mixing tank will eventually reach the weir overflows that feed into the header tanks. This allows the TJWF to be operating in several operational modes.

The TJWF as-built dimensions are 762 mm by 1016 mm by 1206.5 mm defined as the outside length, width, and height including the thickness of the walls. The jet head extends 384.175 mm above the bottom of the TJWF and the top of the tank is 822.325 mm above the jet head. A schematic of the jet head with major dimensions that are 171.45 mm by 47.752 mm by 279.4 mm in length, width, and height shown in Figure 2.2. Each jet is 87.63 mm by 5.8 mm in length and width and are separated by 12 mm sheet of acrylic. This yields a centerline to centerline separation distance of 17.8 mm.

2.1.1 Hydraulic Diameter and Reynolds Numbers Definitions

The hydraulic diameter of the twin jet is calculated using the standard definition,

$$D_h = 4\frac{A}{P} = \frac{2wL}{L+w} \tag{2.1}$$

The Reynolds number definition used for the majority of the experimental work was defined using the above definition as

$$Re_{D_h} = \frac{\rho U D_h}{\mu} \tag{2.2}$$

Whereas the definition of Reynolds number in literature is based on the jet width and stated as,

Figure 2.1: Twin Jet Water Facility during the UTK Experimental Campaign [9]

$$Re_a = \frac{\rho U a}{\mu} \tag{2.3}$$

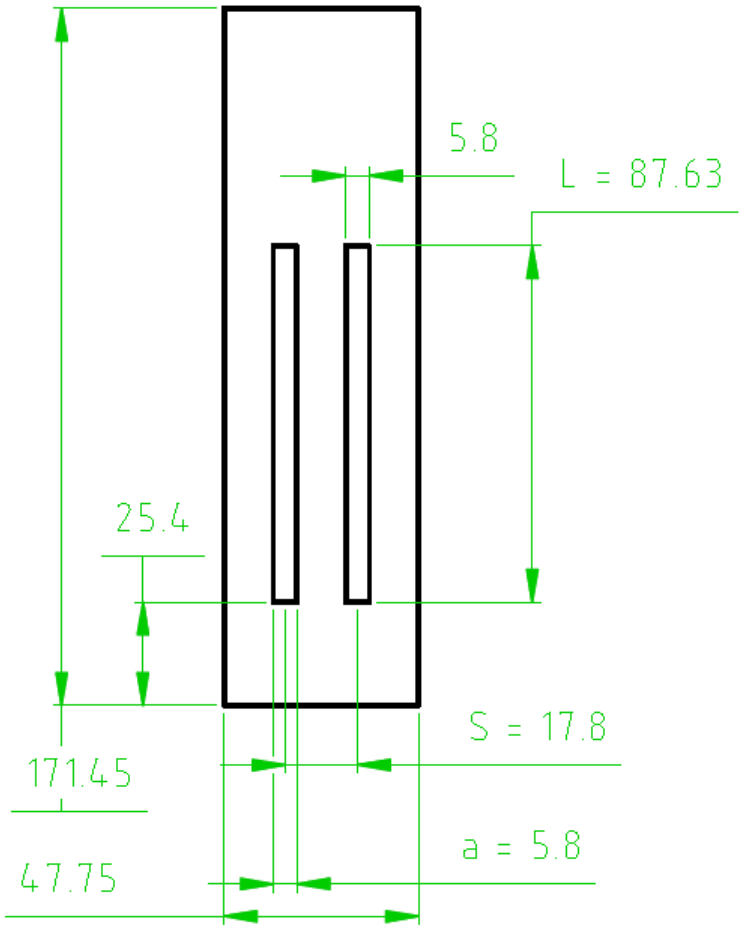

Figure 2.2: Twin Jet Water Facility Jet Head Schematic

where ρ and μ are density ($\frac{kg}{m^3}$) and dynamic viscosity ($Pa - s$).

The aspect ratio ($\frac{L}{a}$) of the jet which provides a basic means of determining if secondary flows are still contributing to the "centerline" behavior of jet is 15.1. This is not high enough to suggest that the TJWF experiments can be simulated without considering the effect of secondary flows [50]. This requires 3-D simulations to be conducted to appropriately account for the twin jet mixing behaviors. Based on this information, the Reynolds number used for the duration of these studies will based off the hydraulic di-

ameter of each jet. This is further motivated to ensure consistency with the experimental efforts at UTK and TAMU.

2.2 UTK Experiments

The UTK Thermal Fluids group conducted one set of the experimental campaign using Particle Image Velocimetry (PIV) and UVP measurements. Their efforts documents the initial PIV data collected by Crosskey et. al. [9] presented with error estimates. These error estimates are separated by the symmetric and random components. An effort to determine difference in measurements of PIV and UVP techniques was done by Wiggins et. al. [10]. In this work, they were able to show strong agreement of the two measurement techniques in the combined region of flow shown. They did observe poor agreement of the measurements in the converging region which is recommended for further study shown in figure 2.3. The disagreement of the measurements manifested in the form of a strong asymmetry where one jet had a much larger profile than the other.

2.3 TAMU Experiments

The TAMU Thermal-Hydraulic Research Laboratory has ongoing experimental efforts using a variety of different measurement techniques within the TJWF. These efforts include LDV, PIV, UVP, and Laser Induced Fluorescence (LIF) to do both isothermal and heat transfer experiments. The focus of the current work has been on isothermal conditions using similar initial and boundary conditions that was utilized by Crosskey et. al. [9]. These conditions establish the basis of the initial and boundary conditions of the twin jet simulations discussed later and can be found in Table 2.3.

The LDV results are quite extensive and include many forms of data throughout the converging, merging, and combining regions of flow [12]. This includes velocity profiles, vorticity profiles, Reynolds stress profiles of streamwise and spanwise component, and merge/combined points. The currently available PIV results [13] include velocity profiles,

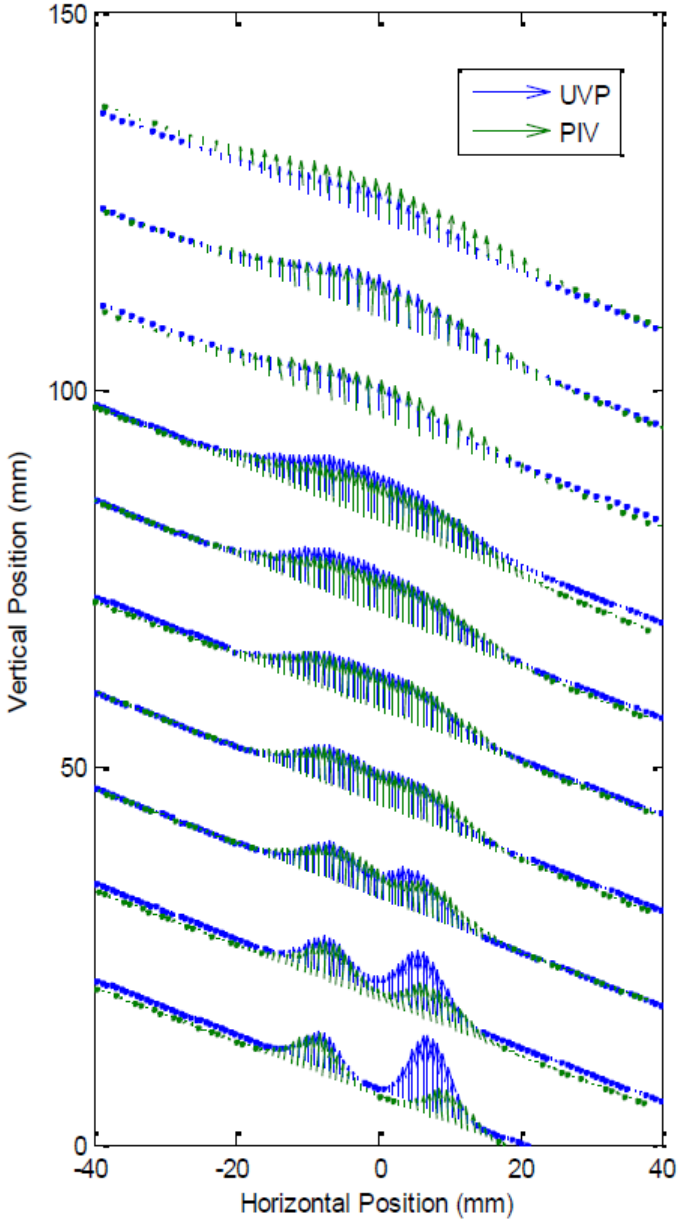

Figure 2.3: Comparison of UVP vs. PIV Measurements in TJWF [10]

and Reynolds stress profiles, and turbulent intensity profiles. These two sets of experimental results are utilized for the majority of the validation work discussed in later sections.

There are several ongoing efforts to collect additional using PIV, UVP, and LIF data.

Institution	UTK-PIV	UTK-UVP	TAMU-LDV & PIV	TAMU - UVP
Pressure (kPa)	Ambient	Ambient	Ambient	Ambient
Temperature ($^{\circ}C$)	26	20	23	23
Flow rate (per jet - $\frac{kg}{s}$)	0.385	0.378	0.385	0.385
Ave. Inlet Velocity ($\frac{m}{s}$)	0.75	0.74	0.75	0.75
Reynolds Number (D_h)	9100	8000	9100	9100
Reynolds Number (a)	4900	4300	4900	4900

Table 2.1: Experimental Test Conditions for TAMU and UTK Campaigns

Recently, Lee and Hassan [51] published work involving additional collection of PIV data and conducted Proper Orthogonal Decomposition (POD) on the data. A UVP effort by Cabral et. al. [52] to determine the performance of the UVP measurements of the merge point and combined point as compared to LDV and PIV. There is an on-going effort to investigate thermal mixing within the TJWF using LIF, but published material does not exist for it yet.

2.3.1 Experimental Uncertainty

The experimental uncertainty for the velocity in the streamwise and spanwise directions, and off-diagonal Reynolds stress component ($\overline{uv}$ on the measurement plane were calculated using data measured at three different points in the domain. This data was provided by Wang et. al. [53] for the ASME V&V Symposium Benchmark Problem in 2016 for the different participants to apply their own form of solution validation. The data points were provided in locations shown in figure 2.4 with each point in either the converging, merging, or combined region of flow. This allows for an uncertainty representative of each region to be applied to the quantities of interest used for solution validation.

Each point was sampled $3,000$ times randomly in time to get instantaneous values for streamwise and spanwise velocity values. The streamwise and spanwise velocity components for the merging region are shown in figure 2.5. The mean, standard deviation,

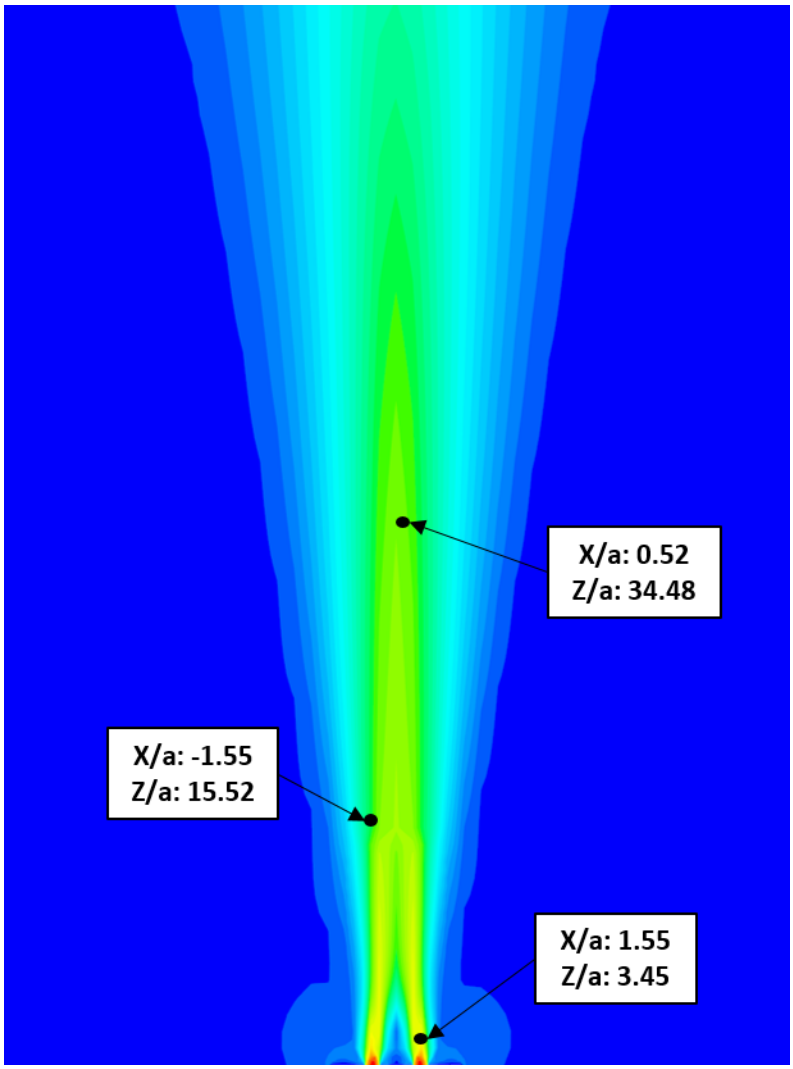

Figure 2.4: Locations of Measurement Points for use of Determining Experimental Uncertainty

and standard error of the mean for each component were calculated using the following equations.

$$\overline{u} = \mu_{\overline{u}} = \frac{\sum_{i=1}^{N} u_i}{N} \tag{2.4}$$

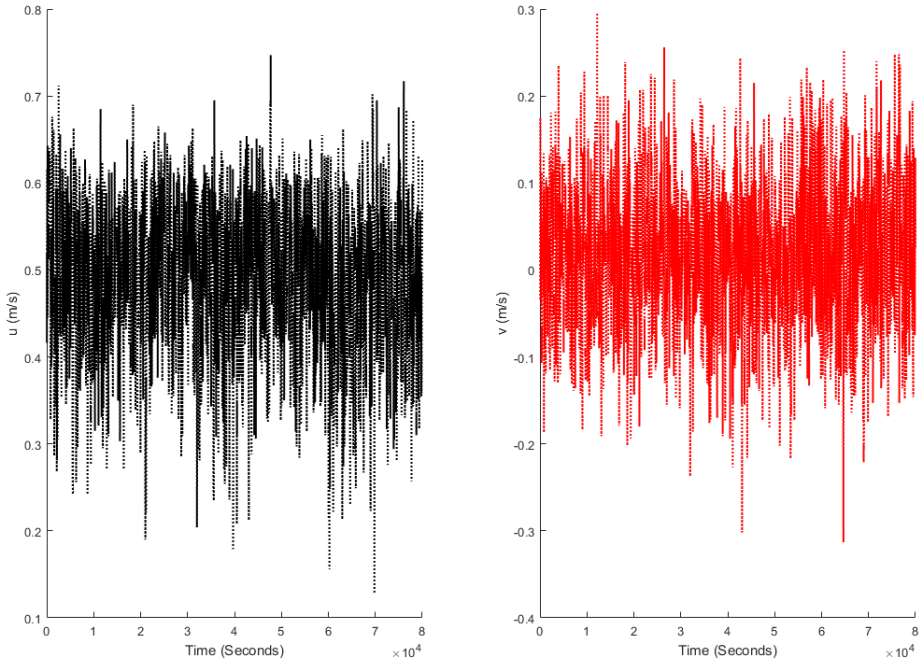

Figure 2.5: Velocity Signals of Streamwise and Spanwise Components at $\frac{Z}{a} = 3.45, \frac{X}{a} = 1.51$

$$\sigma_{\overline{u}} = \sqrt{\frac{1}{N-1}\sum_{i=1}^{N}|u_i - \mu_{\overline{u}}|^2} \tag{2.5}$$

$$\alpha_{\overline{u}} = \frac{\sigma_{\mu_{\overline{u}}}}{\sqrt{N}} \tag{2.6}$$

The Reynolds stress off-diagonal component of the streamwise and spanwise velocities at a specific point is calculated by taking the covariance of the two signals. This is represented as the following equation.

$$\overline{u'v'} = cov(u_i, v_i) = E[u_i v_i] - E[u_i]E[v_i] = \frac{\sum_{i=1}^{N} u_i \times v_i}{N} - \mu_{\overline{u}}\mu_{\overline{v}} \tag{2.7}$$

The standard error of the mean for $\overline{uv}$ is calculated using the cross correlation of steamwise and spanwise components.

$$\rho_{uv} = \frac{cov(u_i, v_i)}{\sigma_{\overline{u}}\sigma_{\overline{v}}} \tag{2.8}$$

Then using the cross-correlation, the SEM of $\overline{uv}$ is calculated using the following equation found in [54].

$$\alpha_{\overline{u'v'}} = \sigma_{\overline{u}}\sigma_{\overline{v}}\sqrt{\frac{1+\rho_{uv}^2}{N-1}} \tag{2.9}$$

The fractional uncertainties (fractional SEM) are calculated by normalizing by the mean value of the quantity of interest. The overall quantities for each point are summaries in table 2.3.1 and are applied as $x \pm 2\alpha_x$.

$\frac{X}{a}$	$\frac{Z}{a}$	$\overline{u}$	$\frac{\alpha_u}{\overline{u}}$	$\overline{v}$	$\frac{\alpha_v}{\overline{v}}$	$\overline{u'v'}$	$\frac{\alpha_{u'v'}}{\overline{u'v'}}$
1.55	3.45	0.751	0.00287	-0.0381	0.0416	0.00343	0.0575
-1.55	15.52	0.509	0.00363	0.0006	2.81	-0.00356	0.0513
0.52	34.48	0.495	0.00316	0.0197	0.0716	0.00148	0.0836

Table 2.2: Mean Values and Fractional SEM at Points in the Converging, Merging, and Combined Regions

3. COMPUTATIONAL MODELING AND METHODOLOGY

The computational modeling of the TJWF were focused on using steady RANS to simulate the twin jet physics. Unsteady RANS simulations were not approached due to the additional time requirement and additional complexity for analysis regarding solution V&V. It is noted that unsteady effects of the twin jet behavior will not be captured using steady RANS such as low frequency "flapping" of the combined jet. It is not believed to significantly contribute to the parameters compared and discussed in chapters 4 and 5.

This chapter covers the governing equations, turbulence modeling, modeling assumptions, specific computational domain, and meshing used for the RANS efforts. Further, the relevant post processing of quantities of interest will be covered to ensure no confusion exists over how these were calculated.

3.1 Physics and Governing Equations

The twin jet simulations were approached using an incompressible RANS framework with isothermal conditions. The simulations were conducted as steady state where the time dependent terms were set to zero. The steady RANS equations in this work are shown below in tensor form.

Continuity:

$$\frac{\partial \overline{u_i}}{\partial x_i} = 0 \tag{3.1}$$

where $\overline{u_i}$ includes the streamwise (1) and spanwise (2, 3) velocity components. The momentum (Reynolds) equations are,

$$\rho \frac{\partial}{x_j} \overline{u_i u_j} = -\frac{\partial \overline{p}}{\partial x_i} + \frac{\partial}{\partial x_j}(2\mu S_{ij} - \rho \overline{u_i' u_j'}) \tag{3.2}$$

where $\overline{u_1'^2} = \overline{u'^2}$, $\overline{u_2'^2} = \overline{v'^2}$, $\overline{u_3'^2} = \overline{w'^2}$ are the Reynolds shear (off-diagonal) stresses and

$\overline{u_1'u_2'} = \overline{u'v'}$, $\overline{u_1'u_3'} = \overline{u'w'}$, $\overline{u_2'u_3'} = \overline{v'w'}$ are the Reynolds normal (diagonal) stresses. These quantities together are contained in the Reynolds stress tensor τ and are not solved directly in two-equation turbulent models.

The Boussinesq eddy viscosity assumption which relates the Reynolds stress tensor and the mean strain rate is used. The mean strain-rate tensor, S_{ij}, is represented in the equation 3.3.

$$S_{ij} = \frac{1}{2}\left(\frac{\partial \overline{u_i}}{\partial x_j} + \frac{\partial \overline{u_j}}{\partial x_i}\right) \tag{3.3}$$

The relationship between mean strain rate and the Reynolds stress tensor is shown in equation 3.4

$$-\overline{u_i u_j} = 2\nu_\tau S_{ij} - \frac{2}{3}\kappa\delta_{ij} \tag{3.4}$$

where δ_{ij} is the Kronecker delta and is zero for off-diagonal components ($i = j$), ν_{tau} is the kinematic eddy viscosity, and κ is the turbulent kinetic energy. The turbulent kinetic energy is represented by equation 3.5.

$$\kappa = \frac{1}{2}\overline{u_i' u_i'} \tag{3.5}$$

The kinematic eddy viscosity and turbulent kinetic energy are solved for using the standard $\kappa - \epsilon$ turbulence model discussed partial in subsection 3.1.1.

3.1.1 Turbulence Modeling

Standard κ-ϵ Turbulence Model

The standard $\kappa - \epsilon$ turbulence model is an industry standard model implemented in most commercial CFD solvers. It has almost ubiquitous usage throughout the overall CFD communities and is commonly seen in most nuclear engineering CFD literature. It is classified as a two-equation model involving both turbulent kinetic energy (TKE) (κ) and

dissipation (ϵ).

The steady-state two equations for the standard $\kappa - \epsilon$ turbulence model are shown in the equations below.

$$\rho \nabla \kappa \overrightarrow{u} = \nabla[(\mu + \frac{\mu_t}{\sigma_k})\nabla\kappa] + P_\kappa - \rho(\epsilon - \epsilon_0) + S_\kappa \tag{3.6}$$

$$\rho \nabla \epsilon \overrightarrow{u} = \nabla[(\mu + \frac{\mu_t}{\sigma_k})\nabla\epsilon] + \frac{1}{T_0} C_{\epsilon_1} P_\epsilon - C_{\epsilon_2} f_2 \rho (\frac{\epsilon}{T_0} - \frac{\epsilon_0}{T_0}) + S_\epsilon \tag{3.7}$$

The full time dependent equations, individual terms and coefficients are discussed in detail in Appendix A.

The work by Behrouzi et. al. [48], Anderson et, al. [7]. involved the usage of the standard $\kappa - \epsilon$ turbulence model. As previously mentioned, Behrouzi did a very minimal qualitative comparison while Anderson did both an extensive qualitative and quantitative comparison to the twin planar jet phenomenon based on centerline measurements. The standard $\kappa - \epsilon$ turbulence model was selected to reduce the complexity of the analysis and limit the computational resources needed. The underlying assumptions of tandard $\kappa - \epsilon$ turbulence model are discussed in greater detail in the provided references [55], [56]. This provides motivation for the inclusion of this turbulent model for the RANS studies.

3.1.2 Numerical Method

The RANS equations were discretized using the finite volume method and solved using the SIMPLE algorithm with Rhoe-Chow interpolation. This is referred to as the segregated solvers in Star-CCM+ v10.06.010 [57] and v11.04.012 [11].

3.1.3 Numerical Convergence Criteria

Each individual simulation was ran for a large enough number of iterations in order for the residuals of continuity, momentum (x, y, and z), and turbulent quantities to reduce 3-4

orders of magnitude. The residuals were run past the original reduction criteria to ensure residual behavior did not significantly change after a meaningful number of iterations had been calculated. In this case, the significant change is intended to mean the residuals began oscillating around their specific reduction value and an example is shown in figure 3.1.

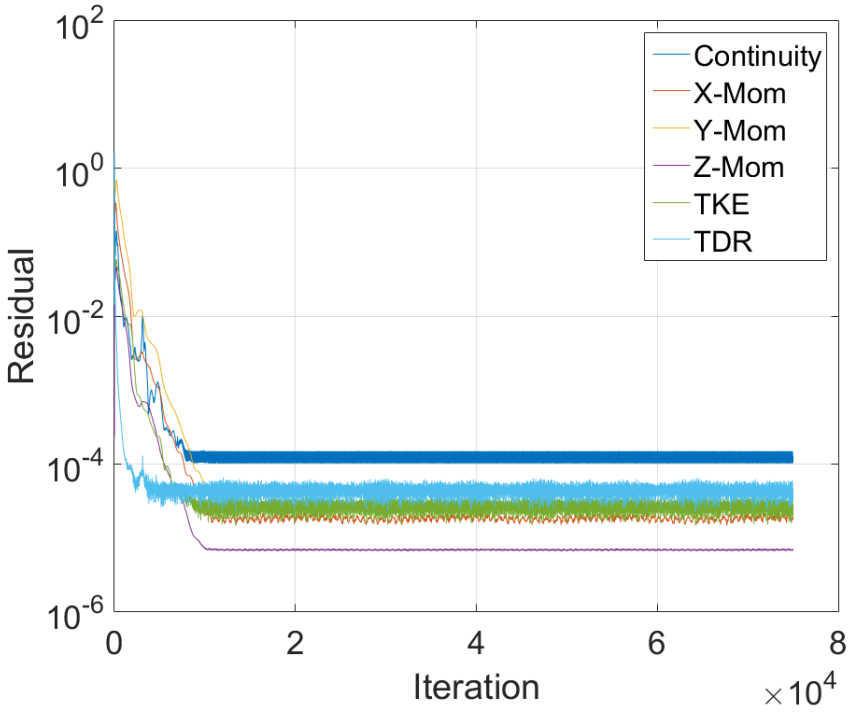

Figure 3.1: Example of Residual Behavior for the TJWF Simulations

The residuals are calculated as the root mean square of the absolute error of the quantities discussed and normalized by the maximum residual for all of the iterations. This is shown by the following equation,

$$Residual(\phi) = \frac{\sqrt{\frac{1}{n}\sum_{i=1}^{N} r^2}}{Max(Res_j(\phi))} \tag{3.8}$$

where r is the absolute error of the quantity and ϕ is a quantity of interest.

Quantities such as the centerline streamwise velocity and velocity profiles at different characteristics heights were spot checked during runs to ensure calculations were approaching or had reached asymptotic behavior. Specific points of streamwise velocity in the merging, converging, and combined regions of flow were plotted and tracked during the runs. These plotted over the number of iterations to ensure they plateaued out values to ensure numerical convergence.

3.1.4 Near Wall Modeling

The near wall modeling for the different turbulence models utilized a two-layer [58] or all y^+ wall treatment [11]. The wall treatment are damping functions meant to model the viscosity-affected near-wall regions in a domain. The functions are utilizing a predetermined length-scale in specific near wall regions. The all y^+ wall treatment is used as a blended model between the low y^+ wall and high y^+ wall treatments. The low y^+ treatment directly resolves the viscous sublayer and requires the first cell or node is placed $y^+ < 1$. The high y^+ treatment uses damping functions to model the viscous sublayer and places a requirement that the first cell or node is placed $y^+ > 30$. A graphical depiction of Star-CCM+'s low, blending (all wall), and high y^+ approaches are shown in figure 3.2.

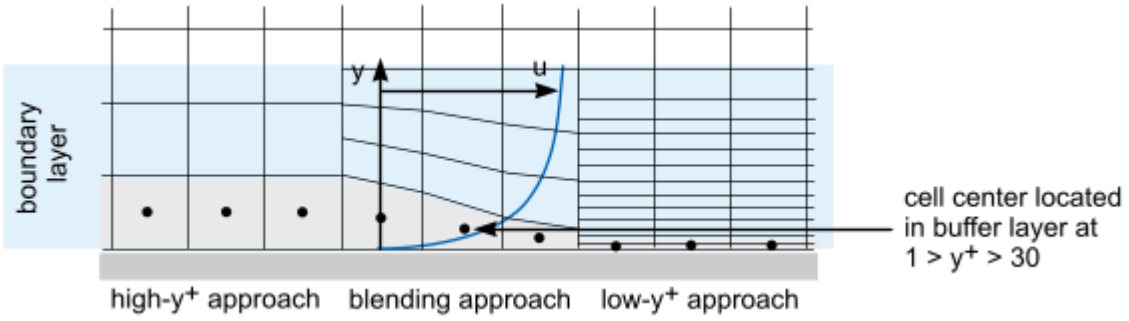

Figure 3.2: Near Wall Behavior and Wall Treatment used in Star-CCM+ [11]

In general, this is quite important behavior to ensure is appropriately resolved. For the twin jets, it is relaxed for the enclosure walls due to the extremely low velocities and lack of impact on the twin jet physics. This is discussed in subsection 3.3.1.

3.2 Computational Domain Creation

The computational domain for the RANS studies was created using a trade off of representing the true domain and computational intensity. This is generally true for any CFD analysis and the major simplifications are discussed in detail below. The computational domain could potentially be simplified further, but was acceptable for the author's available computational resources. The computational domain used in the RANS studies is shown in Figure 3.3.

3.2.1 Simplifying Assumptions

The following simplifying assumptions are utilized to reduce the meshing and physics modeling requirements and consequently the computational and time requirements of the simulations.

Water-Air Interface

The internal volume of the TJWF is mostly water with an water-air interface around the same height as the weir overflows. The water surface of the water-air interface is assumed to experience minor movement. This enables the usage of slip wall condition instead of fully modeling the upper computational domain and the movement of the water surface. A future sensitivity study in the future could look at the usage of moving (deforming) mesh or fluid of volume implementations used by Carasik et. al. [59] for a similar study. Though, it is not expected to have a significant impact on the results of the study.

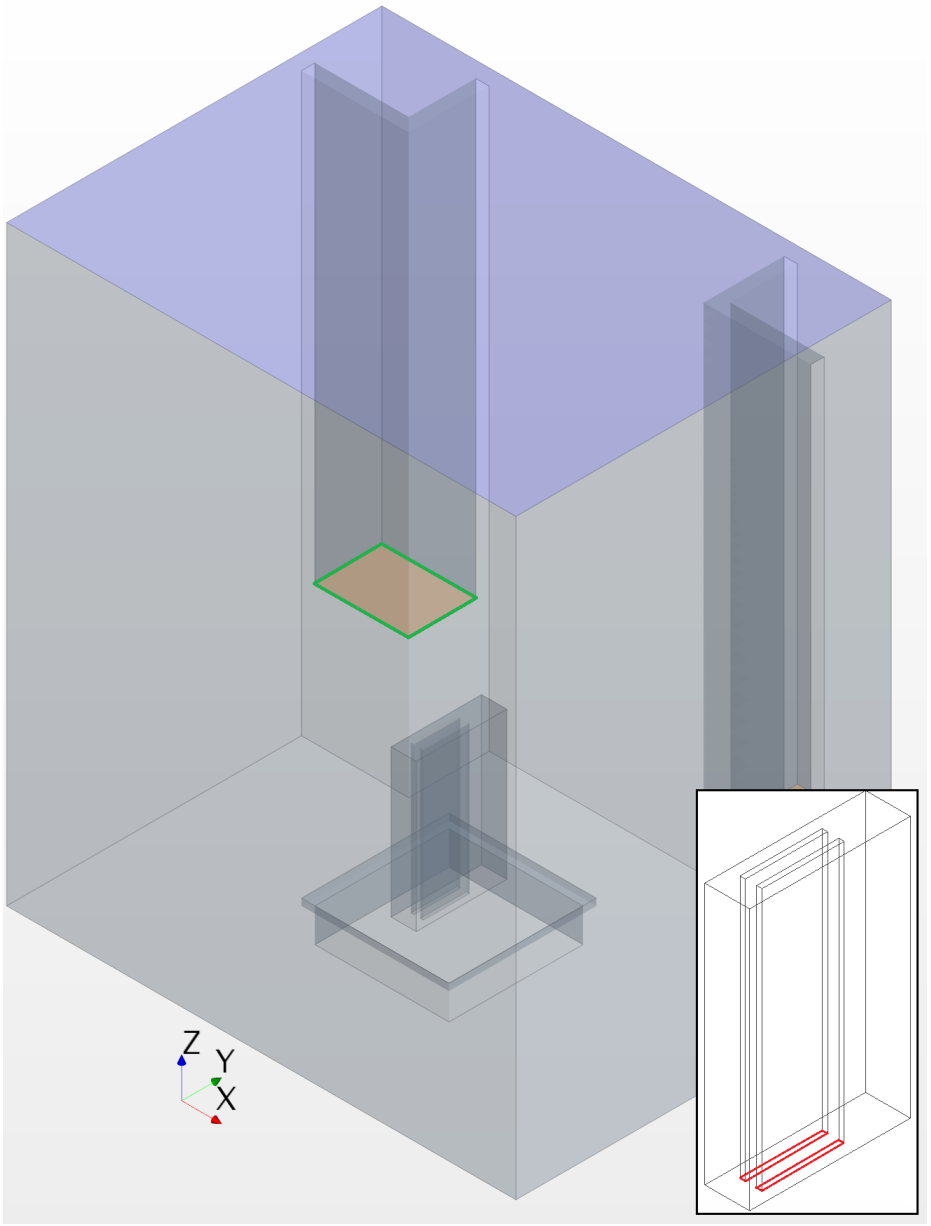

Figure 3.3: Twin Jet Water Facility Computational Geometry used for RANS Studies with Inlet (Red) and Outlet (Green) Boundaries Highlighted

Reduction of Upstream Domain

The upstream effects from stagnation boxes feeding into the inlet jets cause some asymmetry to be observed near the inlet jet exhausts [12]. Based on previous works by

Carasik et. al. ([60], [61]), the impact of the asymmetry from the stagnation boxes was not found to significantly impact the observed quantities of importance. A future sensitivity study could be conducted to determine if the upstream conditions (and lack of inclusion of stagnation boxes) affect the MP and CP. Anderson et. al. [7] determination of scatter of MP and CP for different experimental facilities would support an investigation into this.

Additional Geometric Features

Components such as bolts, nuts, instrumentation (such as joint PIV UVP studies) are not considered to impact the flow results. These are not reflected in the simulation efforts. These features would likely add a significant number of additional mesh cells which would be a waste of computational resources.

3.3 Meshing Techniques

3.3.1 Near Wall Meshing

The near wall mesh created using the prism layer mesher on all surfaces (excluding the jets and the top surface of the jet head) using a total thickness of 2.0 mm. There are four prism layers with a stretching factor of 1.1 to smooth the transition for each layer. The flow in the regions near the walls, excluding the jet, experience very low flow velocities and are not very important to simulate the behavior. In the these regions, the prism layers are created for completeness and are checked to ensure the near wall modeling in valid. An approximate calculation of the thickness of each layer is shown in table 3.3.1.

Prism Layer	Thickness (mm)	Distance from Wall (mm)
1	0.431	0.431
2	0.474	0.905
3	0.521	1.426
4	0.574	2.000

Table 3.1: Near Wall Prism Layer Properties

3.3.2 Inlet Jets

The inlet jets were held constant for both refinement strategies analysis. Both inlet jets are created using a target surface minimum size of 0.15 mm and target maximum size of 0.25 mm. The inlet jets are 50 meshing layers stretched by 1.3 ratio for a total distance of 279.4 mm. The mesh of the inlet jets was created using extrusions from the inlet surface. It is defined at the point where the inlets are connected to the large enclosure. The surface had target minimum size of 0.15 mm and a targeted maximum size of 0.25 mm.

Precursor Simulations

These sizes ensured that flow was sufficiently resolved the inlet flow and based on a comparison to precursor simulations. The precursor simulations were conducted using the Star-CCM+ v10.06.010 [57] for the entire 279.4 mm length of the jet. The inlet was defined as a uniform velocity corresponding to the experimental and TJWF simulation inlet velocity. The outlet was set as a static pressure out. The mass flow rate corresponded to the same one used in the experimental and the full TJWF simulations. The mesh was created using the directed mesher with double hyperbolic stetching in both spanwise directions with the first cell starting at 0.1 mm. The streamwise direction was split evenly for the specified number of layers. This was done to ensure the near wall regions were properly resolved and the mesh parameters are shown in table 3.3.2. The resulting mesh counts and effective refinement factor defined by equation 1.8 is shown in table 3.3.2.

Mesh	X-Max (mm)	# Layers	Y-Max (mm)	# Layers	Z-Max (mm)	# Layers
1	0.200	30	2.00	100	1.20	250
2	0.176	40	1.55	120	0.93	300
3	0.127	50	1.27	120	0.79	300

Table 3.2: Meshing Parameters for the Inlet Jet Precursor Simulations

Mesh	Mesh Count	Eff. R_{12}
1	$7.50 * 10^5$	n/a
2	$1.44 * 10^6$	1.24
3	$2.45 * 10^6$	1.19

Table 3.3: Meshing Information for the Inlet Jet Precursor Simulations

The precursor simulations were ran using the same convergence criteria discussed in subsection 3.1.3 and utilized the standard $\kappa - \epsilon$ turbulence model with the two-layer/all y^+ wall treatment. The outlet profiles along the x-axis at the outlet boundary for the precursor simulations and the profiles at exhaust and $\frac{1}{4}$ in the inlet jet from the exhaust for the TJWF simulations are shown in figure 3.4. The x-axis in this case is along the width of the jets which is previously defined as being the y-axis in chapter 1. The profiles are very close and provide support for the inlet meshing selected for the TJWF simulations.

3.3.3 Outlets

The outlet extensions are created by using the surface mesh where the original "outlet" surface is defined. The mesh is extruded with 25 meshing layers being stretched using a 1.4 ratio for a total distance of 600 mm. The outlets extensions were made long enough to ensure backflow/reversed issues are strongly reduced and prevented numerical convergence issues. The length was determined using the mesh with the lowest number of D.O.F. and varying the length until the number of cells encountering reversed flow was minimized.

3.3.4 Bulk Refinement Strategy

The "bulk" refinement meshing strategy is being used to investigate the meshing requirements for non-specific mesh refinement. The entire domain, excluding the inlet jets and the outlet extensions, are being meshed using the same overall requirements. The bulk meshing base size and maximum size and the resulting cell counts are shown in Table

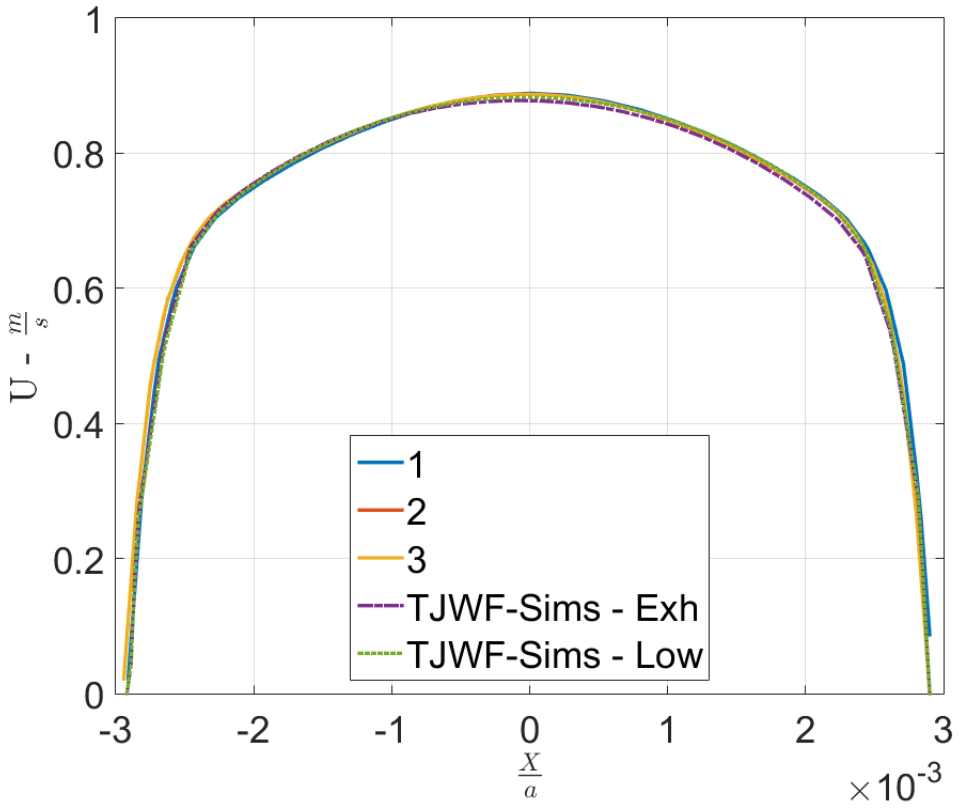

Figure 3.4: Inlet Jet Profile along the X-Axis

3.3.4. The meshing for the bulk region is shown in Figure 3.5.

Mesh Identifier	Base Size (mm)	Maximum Cell Size (mm)	Cell Count
M1	25	50	$4.8 * 10^6$
M2	12.5	25	$14.3 * 10^6$
M3	6.25	12.5	$14.5 * 10^6$
M4	3.125	6.25	$16.9 * 10^6$
M5	1.5625	3.13	$38.2 * 10^6$
M6	0.78125	1.56	$236 * 10^6$

Table 3.4: Bulk Mesh Sizes and Cell Counts

It is worth noting that the largest mesh is an enormous number of D.O.F. for a steady state simulation of a reasonably simple geometry. At the point of writing, it would not be expected to see such a large amount of mesh cells for a calculation such as this using RANS.

3.3.5 Spot Refinement Strategy

The "spot" refinement meshing strategy is being used to investigate the reduced meshing requirements for when specific regions are being refined. There are three spot refinement regions utilized and labeled; jet inlet, core, and expansion. Each of the refinement regions were defined with in an isotropic manner such that x, y, and z directions with have the same size. The base and maximum cell sizes defined for the mesh overall are the same as seen in Table 3.3.4. The specific sizes for each spot region and the cell count for each mesh is found in Table 3.3.5. An example of the meshing for the spot strategy is shown in Figure 3.5.

This refinement strategy results in meaningful jumps in D.O.F with every successive mesh level. This ensure that a global refinement is occurring while the localized refinement in the areas of highest gradients are done. This does result in a significantly large mesh by the fourth mesh as opposed to fifth mesh for the bulk refinement strategy. The consequence is the needed computational resources increases faster for the spot refinement strategy as opposed to the bulk refinement strategy but the benefit is discussed in chapter 4.

Mesh Identifier	Jet Inlet Size (mm)	Core Size (mm)	Expansion Size (mm)	Cell Count
M1	5	10	20	$4.9 * 10^6$
M2	2.5	5	10	$14.9 * 10^6$
M3	1.25	2.5	5	$19.2 * 10^6$
M4	0.625	1.25	2.5	$53.2 * 10^6$
M5	0.3125	0.625	1.25	$322 * 10^6$

Table 3.5: Spot Mesh Sizes and Cell Counts

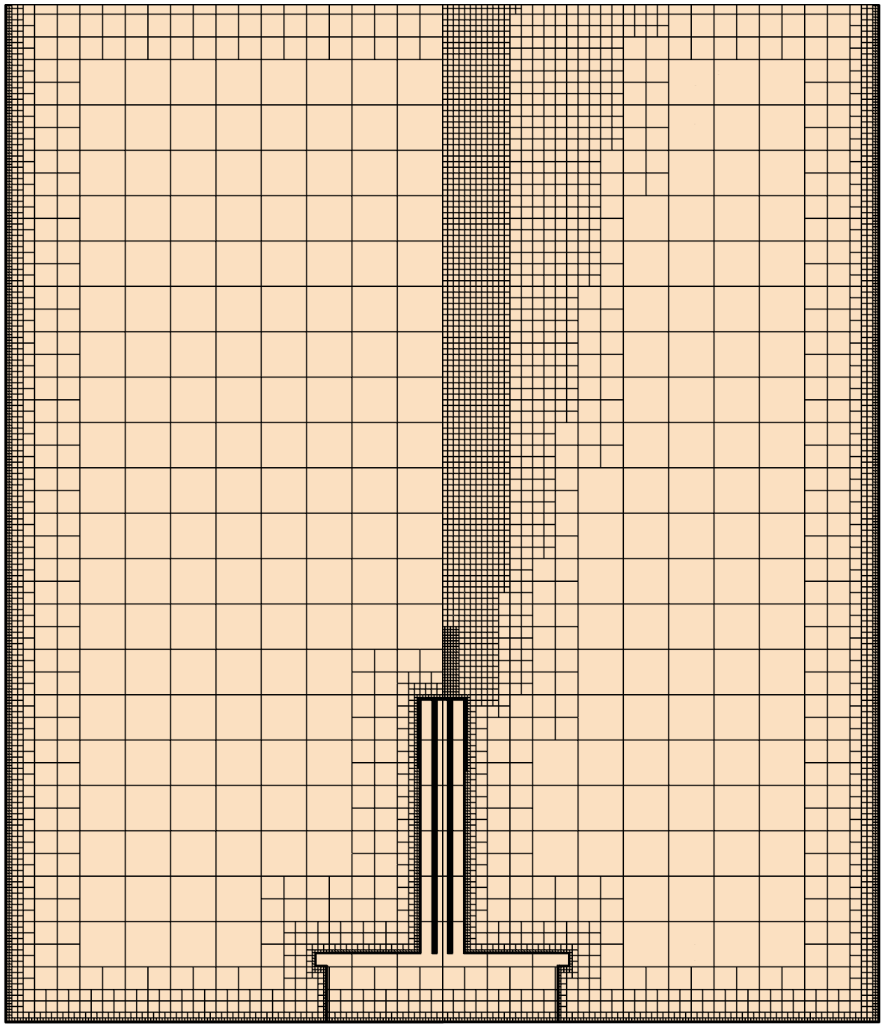

Figure 3.5: Meshing for Bulk (left) and Spot (Right) Refinement Strategies âĂŞ Coarsest Mesh for Each

3.3.6 Boundary and Initial Conditions

The inlet surfaces have a velocity inlet defined with a uniform constant profile. The inlet turbulent specification is done using the turbulence intensity of 0.053 and a length scale of 0.762 mm. The top surface is defined where a water surface with an average constant water height is. The outlets are defined as static-pressure outlets where the velocity gradients are set to zero. The boundaries are summarized in table 3.3.6 which were used

for each simulation. The initial conditions were all initialized from their default values set in Star-CCM+.

Boundary Type	Value	Surface
Velocity Inlet	0.75 $\frac{m}{s}$	Red
Static Pressure Outlet	0 Pa	Green
Symmetry (Slip-Wall)	n/a	Purple
Wall (Non-Slip)	n/a	All Others

Table 3.6: Boundary Conditions used in the Simulations

3.4 Post Processing

The post processing was done using Star-CCM+ built-in post processing tools and Mathworks MATLAB. The raw data was extracted from Star-CCM+ and the imported using csv files into Matlab for data analysis and plotting. The measurement probe points and lines are shown in figure 3.6 where the quantities of interest are extracted. These are created to be analogous to the measurements found in literature (centerline streamwise velocity) and experimental efforts (velocty profiles and Reynolds stress $\overline{u'v'}$ at charateristic heights).

3.4.1 Merge and Combined Points

Using a Star-CCM+'s line probe (see figure 3.6), the centerline streamwise velocity was extracted from each RANS simulations. The merge point was calculated by finding the centerline streamwise velocity that is closest to zero. The corresponding position was then normalized by the jet width. The combined point was calculated by finding the maximum centerline streamwise velocity and the resulting position was normalized by the jet width.

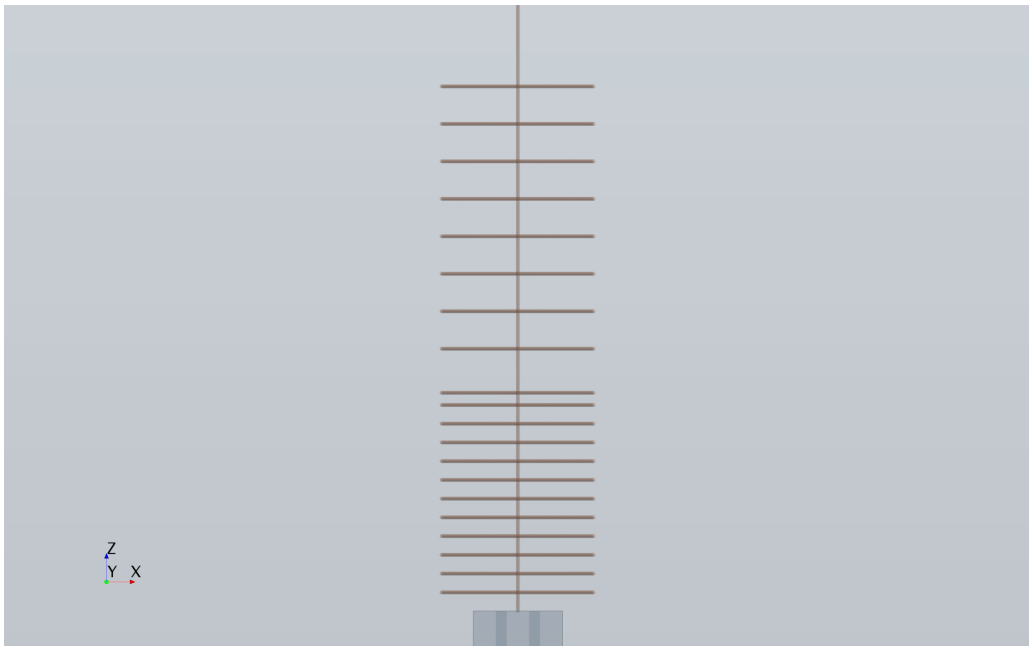

Figure 3.6: Measurement Points defined in the TJWF Simulations

3.4.2 Reynolds Stresses for Two Equation Models

Since the Reynolds stress tensor is not directly calculated when using two equation turbulence models, it is not directly presented as one of the outputs in Star-CCM+. The Boussinesq assumption about the relationship between the turbulent viscosity and velocity gradients are then used again to calculate the Reynolds stress components a posteriori. This assumption is linear in nature and utilized the isotropy assumptions for Reynolds stresses. The Reynolds stress off-diagonal component $\overline{u'v'}$ will be calculated using equation 3.4.

4. TECHNIQUES FOR SOLUTION VERIFICATION ANALYSIS

Two approaches to solution verification analysis are conducted for the TJWF simulations using steady RANS. One approach discussed is based off the GCI and GRE estimation of observed order of accuracy to determine mesh convergence. The second approach is independent of the GCI and GRE framework and allows mesh convergence to be determined without observed order of accuracy.

These is using a form of solution verification to focus on the author's own defined mesh convergence and mesh sensitivity analysis discussed in section 1.3.

4.1 Meshing Strategy Comparison

In order to show the difficulty of applying GCI in an internal flow situation involving turbulence, two mesh refinement strategies are compared for mesh convergence. The first is a bulk strategy discussed in section 3.3.4 that the refinement occurs by reducing the base and maximum cell size with each successful level. The second is a spot strategy discuss in section 3.3.5 where the refinement is done by reducing the base, maximum, and isotropic cell sizes in three large refinement regions.

The bulk strategy is meant to be similar to what is recommended by Roache [24]. Roache argues against highly localized refinements due to issues it causes with GCI. It is shown in order to exemplify the difficulty of obtaining mesh convergence within a reasonable and computationally achievable amount of D.O.F.

The spot strategy is shown as an example of a globally refined mesh with regions of high local refinement. This is similar to approaches observed in standard CFD analyzes found in journals and industry. It is done such that the global refinement recommend by Roache is used and that the savings due to optimizing the number of D.O.F. in regions of highest gradients.

4.1.1 Centerline Streamwise Velocity

The centerline streamwise velocity profiles along the z axis with the starting point defined at $0.5 * S$ and $0.5 * l$ are shown in Figures 4.1 and 4.2 for bulk and spot refinement simulations. The centerline streamwise velocity is considered a "global" quantity allowing for a mesh convergence comparison of the meshing strategies. This is due to the centerline being a probe of information throughout the main region of interesting physics.

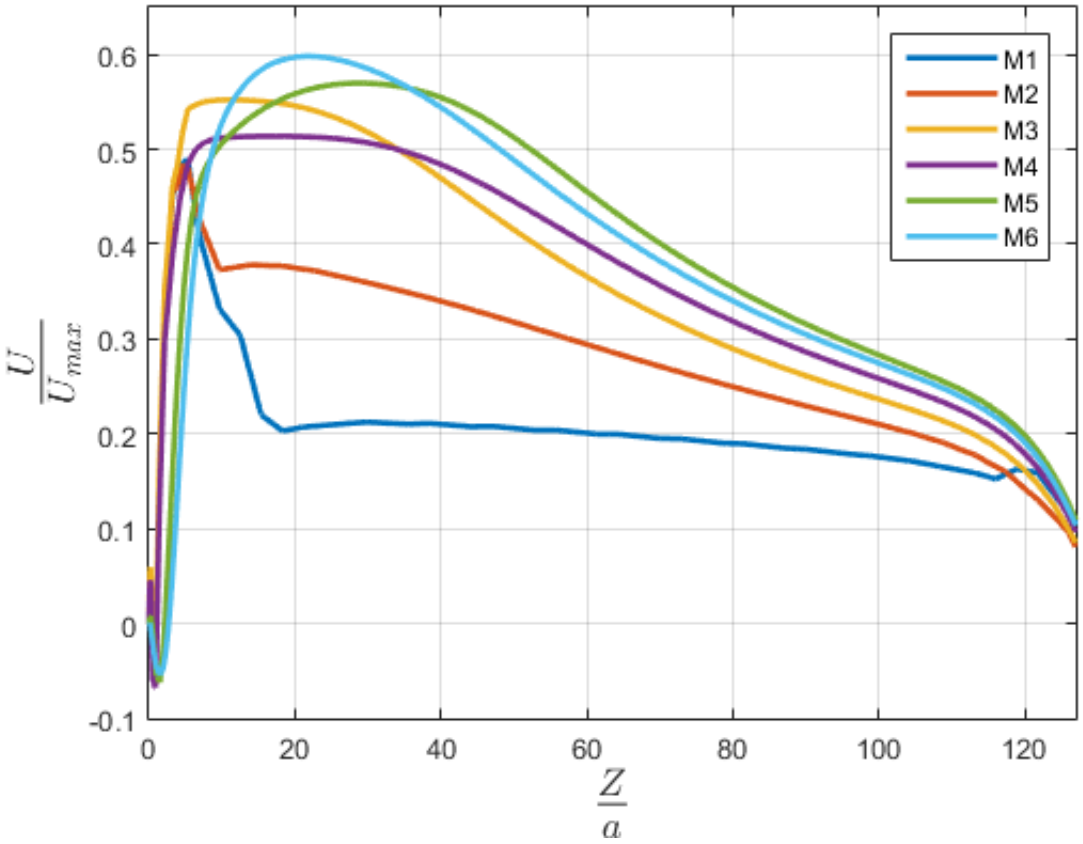

Figure 4.1: Centerline Streamwise Velocity for Six Bulk Meshes of Successive Refinement

Immediately, the bulk strategy is observed to not converge between any two profiles.

The structure of the velocity profile is vaguely similar between each mesh, but still characteristically different. It is obviously deficient and leads to a questioning of the appropriateness of this type of meshing strategy for high aspect ratio problems. In particular, it requires a reasonably large mesh of 16 million D.O.F. to begin resolving the highest gradients of the flow.

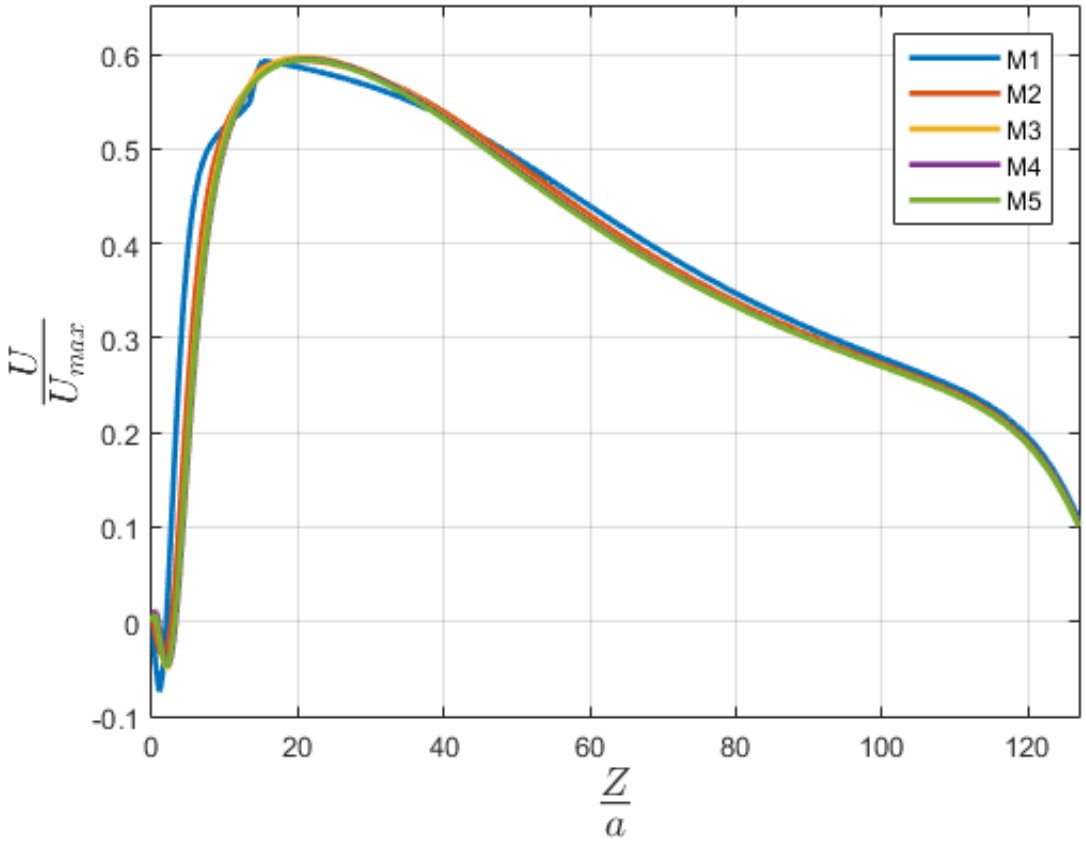

Figure 4.2: Centerline Streamwise Velocity for Six Spot Refined Meshes of Successive Refinement

Even for the smallest number of D.O.F. for the spot strategy, the flow in the centerline is observed to begin resolving the highest gradients. Within one level increase, the flow

is shown to approach the solution of the highest D.O.F. mesh. This is expected behavior from putting an importance on resolving the highest gradients mentioned previously. The behavior of both of these strategies is the same as the profiles observed by Tanaka [42], [43] and Anderson [7]. In general, for a qualitative comparison these results are encouraging but further investigation of other quantities are approached to confirm these observations.

4.1.2 Merge and Combined Points

The merge and combined points for each level of mesh for both meshing strategies are viewed in Table 4.1.2 and 4.1.2. These are provided to show a quantitative measure of mesh convergence or lack of convergence. The MP and CPs provide insight into when the two twin jets are merging and combine into a single self-similar turbulent planar jet.

The MP for the bulk and spot refinement strategies tell entirely different stories of when the flow is being resolved. For the spot meshes, the MP predictions congregate with each increasing refinement of the mesh. This is consistent which the behavior seen of the centerline streamwise velocity in figure 4.2. Whereas, the bulk meshes show an initial amount of clustering for the four coarsest meshes and then significantly jump with the last two meshes. This is not a desirable result in that it indicates that additional refined meshes should be pursued. Further, it is expected due to the number of D.O.F. are not appreciably changing. This is occurring even though the parameters are being consistently halved until the M5 mesh.

The CP for both meshing strategies provide even more detail and a quantitative confirmation of the behavior seen in figures 4.1 and 4.2. The spot meshes quickly gather around the CP prediction of roughly 21 starting between the M2 and M3 meshes. It is believed the predictions will not deviate from this cluster due to this region being sufficiently resolved and the associated percent difference in CP are small. The bulk meshes deviate considerably for each successive refinement in the mesh and do not truly clutter in a meaningful

Identifier	MP - Bulk	% Difference	MP - Spot	% Difference
M1	1.1066	n/a	1.906	n/a
M2	1.1066	0.0	2.6684	33.33
M3	0.88948	21.75	3.1767	17.39
M4	1.1066	21.75	3.3038	3.92
M5	2.1602	64.50	3.1767	3.92
M6	2.6684	21.05	n/a	n/a

Table 4.1: Merge Points Comparison of Bulk and Spot Refinement Strategies

way.

Identifier	CP - Bulk	% Difference	CP - Spot	% Difference
M1	5.3369	n/a	15.1212	n/a
M2	4.7016	12.66	20.4581	30.00
M3	11.8174	86.15	20.9664	2.45
M4	17.153	36.83	21.3476	1.80
M5	28.9717	51.25	21.0934	1.20
M6	21.7288	28.57	n/a	n/a

Table 4.2: Combined Points Comparison of Bulk and Spot Refinement Strategies

4.1.3 Velocity Profiles at Specific Vertical Height

The velocity profile along the x axis centered as the origin at a specified vertical height in the converging region is shown in figures 4.3 and 4.4 for each meshing strategy. This profiles are compared since this is the region of where the highest velocity outside of the inlet jets will be found. It corresponds to the area were the highest gradients in velocity and other quantities of interest are expected to be found. Further, this will give a different piece of information outside of the centerline streamwise velocity, MP, and CP. It will give an indication that the local behavior of the flow which later dominates the downstream features is resolved properly. The information in this region is likely able to give the

clearest signal of the minimal amount of mesh needed.

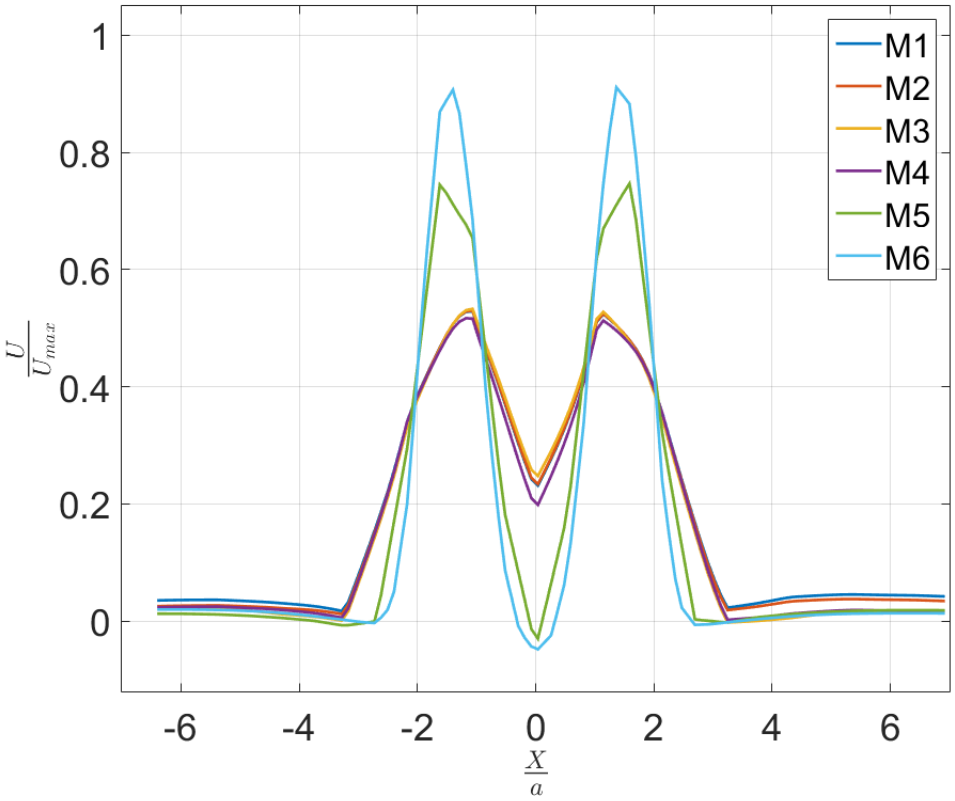

Figure 4.3: Velocity Profiles at $\frac{Z}{a} = 1.72$ for Bulk Meshes

The bulk mesh predictions show a consistent set of behavior observed with the merge points in section 4.1.2. The velocity profiles in this region show an early set of clustering around a similar solution and then make significant jumps in predictions with the finest two meshes. The coarsest meshes (M1-M4) could be mistakenly considered converged but do not show a physical result seen in literature [7], [42]. It is not believed a converged result could be determined from this information considering the meshing strategy.

As seen with the merge points in the section 4.1.2, the velocity profiles begin to con-

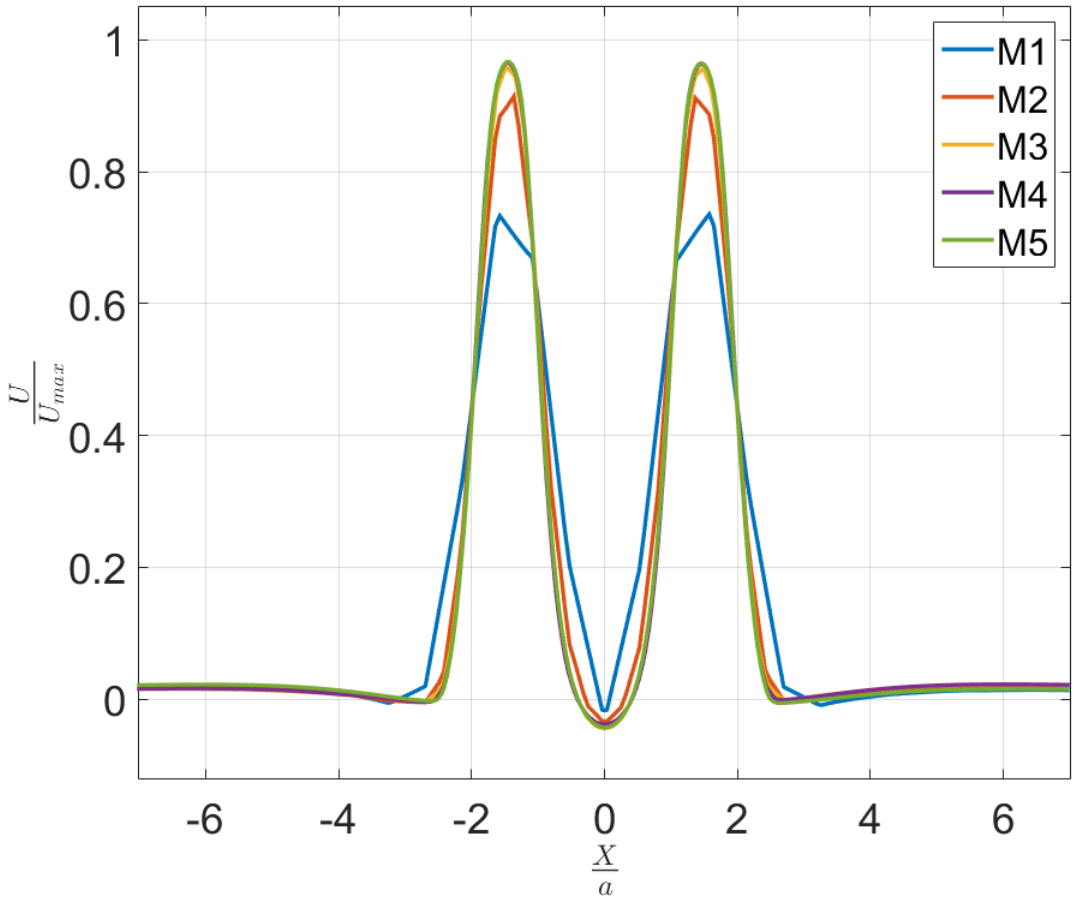

Figure 4.4: Velocity Profiles at $\frac{Z}{a} = 1.72$ for Spot Meshes

gregate within only two levels of mesh refinement. By the M3 mesh, the velocity profiles have reached an undeviating behavior with additional levels of refinement. The velocity profile could serve as an indication of convergence in conjunction with the previously discussed quantities for this meshing strategy. This is discussed in greater details in the following subsections.

4.1.4 Mesh Strategies Summary

In general, a bulk strategy of mesh refinement is a poor choice for high aspect ratio changes in geometry where flow physics of interest are. It is not to say one could not find the strategy to would work well for a simple pipe flow of constant diameter. The evidence was presented here involving the centerline streamwise velocity, merge point and combined points, and the velocity profile in the converging region of flow. All of the evidence clearly presents a case that localized regions of refinement should be utilized in order to reach a converged mesh. This specifically to be done with a reasonable amount of computational resources. If an analyst was to select a bulk strategy of refinement, they would need to go potentially into several billions of D.O.F. to show mesh convergence. This is quite a restrictive amount of cells and would require thousands of cores since the highest meshes were capped at 1000 cores each. Although, this could change in the future with larger computing systems and the utilization of more efficient numerical methods. As more complexities are introduced, it is likely the same problem would be encountered.

4.2 Application of Generalized Richardson Extrapolation Method for Determining Mesh Convergence

Using the spot meshing strategy, mesh convergence was attempted using the generalized Richardson extrapolation method involving one set of grid triplets. This set of grid triplets is the M3-M5 meshes due to clustering behavior discussed in section 4.1. From these grid triplet set, the effective refinement factor was determined between the successive levels. The refinement factors are shown in table 4.2. It is a desired criterion that the refinement factors be above 1.1 [22] or 1.3 [62] to determine if any appreciable difference could be observed. With refinement factors of 1.40 and 1.82 based on equation 1.8, this criterion should be satisfied for this discussion.

Identifier	Mesh Count	Eff. Refinement Factor
M3	19238715	-
M4	53159429	1.40
M5	322941441	1.82

Table 4.3: Effective Refinement Factors between Spot Meshes

4.2.1 Observed Order of Accuracy

In order to determine the observed order of accuracy discussed in section **??**, the transcendental equation for non-equal refinement factors is used. Unfortunately, the guidance is not well defined on what quantities should be utilized for determining P. In this case, several different quantities relevant to the physics of interest are analyzed. Specifically, the MP, CP, maximum streamwise velocity, centerline streamwise velocity profile, and velocity profiles at different heights are compared.

The MP, CP, and maximum streamwise velocity are considered local quantities that are potentially indicative of global behavior. The observed order of accuracy of each is compared using the following equations [62],

$$p = \frac{1}{ln(r_{21})}|ln\left|\frac{\epsilon_{32}}{\epsilon_{21}}\right| + q(p)| \tag{4.1}$$

$$q(p) = ln\left(\frac{r_{21}^{p} - s}{r_{32}^{p} - s}\right) \tag{4.2}$$

$$s = 1 * sgn\left(\frac{f_3 - f_2}{f_2 - f_1}\right) \tag{4.3}$$

where 1 is the finest mesh and 3 is the coarsest mesh.

The observed order of accuracy is calculated iteratively using the formal order of discretization as an initial guess. The first and second equations are updated each iteration until the defined tolerance between the previous and current iteration of P is reached. If

the P becomes effectively zero, the observed P is set to 0.5. Whereas if the P goes above the formal order, the observed P is set to the formal order. This is in accordance with guidance provided by Oberkampf and Roy [29] for providing realistic estimates of observed P. Additionally, the formal order of discretization for these simulations in Star-CCM+ are reportedly 2nd order and $P_f = 2$ is used.

The centerline streamwise velocity profile points and the velocity streamwise profiles can be used as global quantities due to the substantial amount of points in the domain sampled. The observed P is calculated at each point individually and an average of all individual P is created. The mean observed P for each global quantity is reported in table 4.2.1.

Quantity	Type	Observed P	% Error
Merge Point	Local	0.5	75
Combined Point	Local	0.92	54
Maximum V_z	Local	1.01	49.5
Centerline V_z	Global	1.45	27.5
V_z Profiles	Global	1.55	22.5

Table 4.4: Observed Order of Accuracy for Localized and Global Quantities

From observing table 4.2.1, what or which of these quantities should be used to determine a converged set of meshes has been reached? If one was to look at the local quantities, they would find that they are not mesh converged due to a appreciable difference between the observed P and the formal P. This may lead them to continually iterate on meshes and meshing strategies. Which will result in either finding an "appropriate" mesh strategy or fail to do so and consequentially waste a significant amount of computational resources. In contrast, the mean observed P for each of the global quantities are much closer to the formal order. The global observed Ps are observed to have large percent errors with re-

spect to the formal order. This does not provide strong evidence that a converged mesh is contained within this mesh triplet. Additionally, one should consider the distribution of the observed P for the two global quantities which are found in figure 4.5 and 4.6.

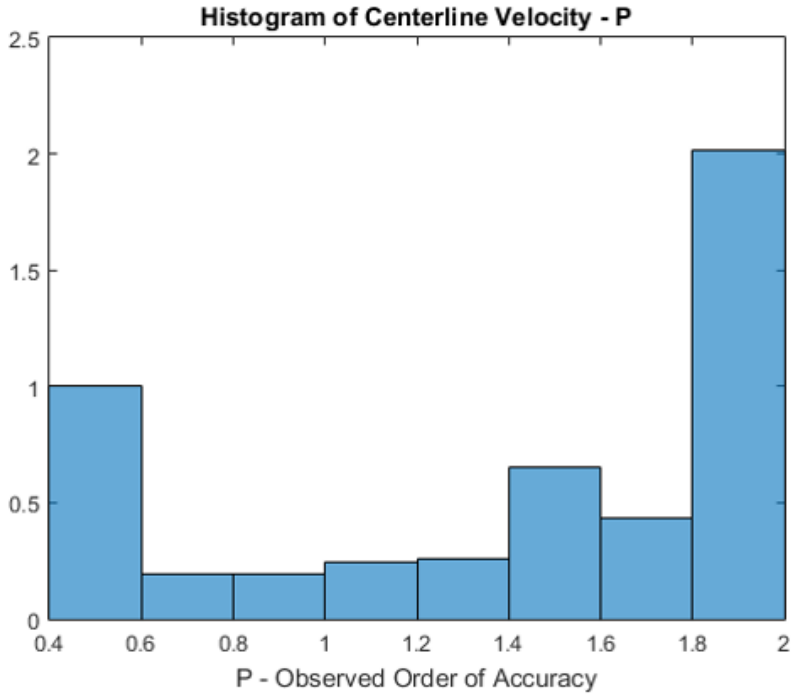

Figure 4.5: Distribution of Observed Order of Accuracy for Centerline Streamwise Velocity

For the centerline streamwise velocity, the distribution is peaked in three places at 0.5, 1.5, and 2.0. The large amount of observed Ps at 0.5 and 2.0 are indicative of failed or non-physical super-converged [63] orders. The smaller peak of 1.5 could be used to support the mean value of 1.45. Although that conclusion is dubious at best, due to the overwhelming amount of failed and super-converged calculated observed P which pollute the mean value.

The distribution of observed P for the velocity profiles shows only two significant peaks of failed and super-converged orders. There is no other observable peak within this

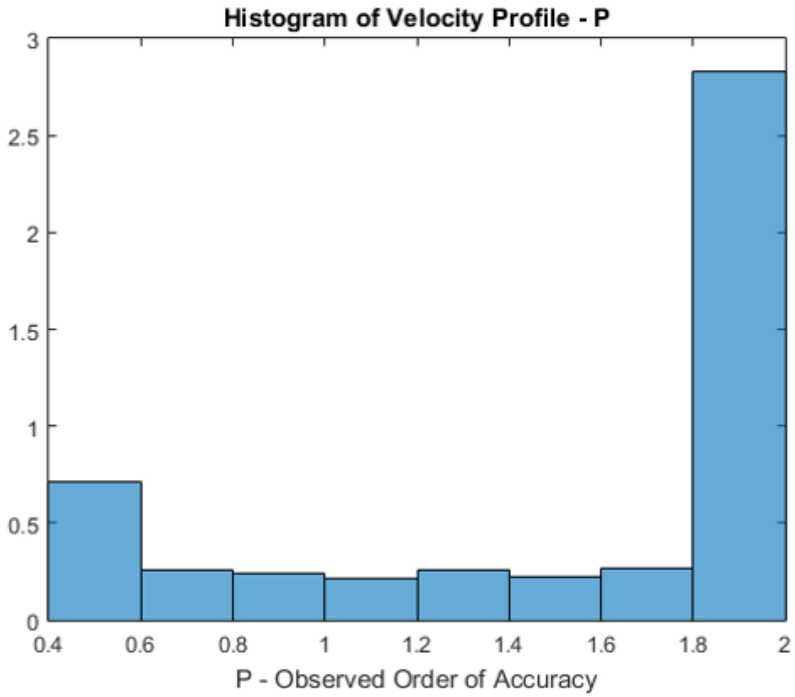

Figure 4.6: Distribution of Observed Order of Accuracy for Streamwise Velocity Profiles

distribution. This indicates the mean observed order of accuracy value of 1.55 is entirely polluted by failed and super-converged orders. It is considered to be incorrect to base mesh convergence off this quantity.

4.2.2 Determination of Applicability - GRE

Based off the discussion in the previous section, it quite difficult to determine if mesh convergence can be determined from the grid triplet shown using the GRE method. This gives little evidence for hope that mesh convergence could be determined using the GRE. It would likely result in an aforementioned waste of time and computational resources which is not a desirable outcome of any CFD analysis.

This result was expected due to the limitations of Richardson extrapolation outside of the asymptotic region where the quantities found above were in the oscillatory and

monotonic divergent behavior. When there is the usage of large areas of local refinement, this method has been shown to fail and leaves a CFD analyst searching for answers on how to define convergence.

One could try and determine which observed order of accuracy to use for subsequent creation of uncertainty (or error) bands on the simulation results. Based off the discussion above and in the author's opinion, a global quantity should be used assuming at least a substantial peak of non-reject or super-convergence orders is shown. Further, the peak should within a $5-10$ percent difference from the mean value. In this case, the center-line streamwise velocity calculated observed P (of 1.45) will be used during the solution validation discussion found in Chp. 5.

4.2.3 Mesh Convergence using a Case of Evidence

An alternate proposed method for determining mesh convergence is presented consistent with the definition discussed in chapter 1. This is presented as a "softer" means of suggesting mesh convergence has been reached in lieu of predictions of observed orders of accuracy. The method is intended as a mixture of qualitative and quantitative mixture of evidence build using at least two supporting substantially difference quantities (or a gradient of a quantity). If a quantity can be shown to reach "convergence" within some range of meshes, it can be used to suggest a minimum requirement of mesh. This alone does not take into account the mesh information on a global or local scale. In order to address this, the gradient of the same quantity can be used to insert mesh information since it directly involves the grid spacing locally. This provides coverage of mesh information in mesh convergence studies strongly encouraged by Roache [22], [24]. It is intended that this can provide an analyst with a simple and power methodology to determine mesh convergence when GRE fails.

Using the results from the previous section 4.1, it could be argued based the M3 level

of mesh would be sufficient. Of course this does not include any meaningful information of mesh in any of the quantities compared. In order to address this, the vorticity in the y-component is calculated and compared in the converging region. Vorticity is calculated using the gradient information of velocity in two directions,

$$\overrightarrow{\omega} = \nabla \times \overrightarrow{u} \tag{4.4}$$

which results in y-vorticity being calculated as follows.

$$\omega_y = \frac{\partial u}{\partial z} - \frac{\partial w}{\partial x} \tag{4.5}$$

Additionally, available correlations or analytical solutions from literature can be used to help build the case of evidence. In fact, it is highly suggested this is included if the analyst can find a suitable and meaningful analytical solution. Though it is not even considered a requirement because outside of specific cases, analytical solutions do not exist. In this case, analytical solutions for the single turbulent planar jet region exist. The analytical solutions for turbulent planar jets [38] which is discussed in detail in section 1.5.3.

y-Vorticity in Converging Region

The vorticity profiles in the converging region for the spot meshes are shown in figure 4.7. The results are shown in the region because this is where vorticity will be largest. If the vorticity is shown to converge within the shown meshes in this region, then the rest of the mesh is likely sufficient. The results are observed to have significant spikes at the $\frac{X}{a} = |1|, |2|$ points which are good to examine if the mesh is resolving. Based off the previous information, the M3 mesh is able to mostly resolve the overall features of the y-vorticity. Although, the differences are notable and the M4 mesh is the minimum recommended for comparison and future studies.

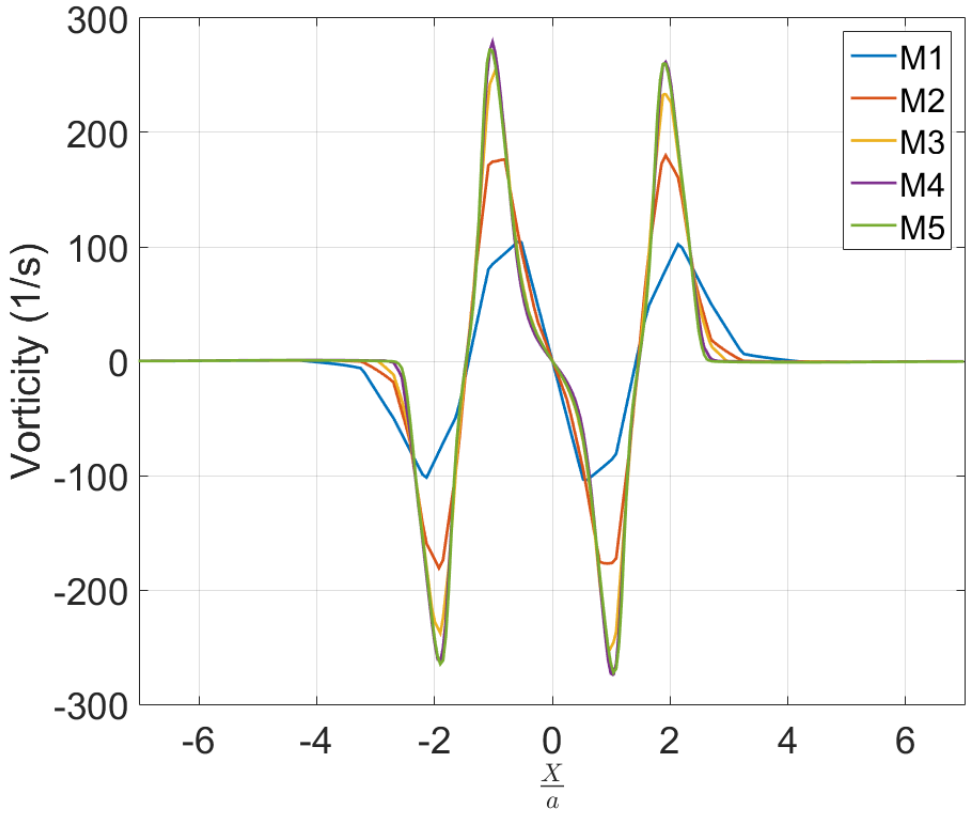

Figure 4.7: y-Vorticity Profiles at Z/a = 1.72 for Spot Meshes

Single Turbulent Planar Jets

The combined region of the twin jets has behavior that is comparable to that of a single planar turbulent jet. The streamwise velocity profiles in this region can be compared to the analytical solutions of Goertler and Tollmien discussed in section 1.5.3. Two sets of CFD velocity profiles are plotted against the analytical solutions in figures 4.8 and 4.9 for the M4 mesh.

The normalizing velocity for each profile is the maximum or peak velocity of the specific profile and not the maximum in the domain. The b for the CFD simulations is calculated for each profile. This is done by finding the points where the velocity is one half of

the maximum velocity on the positive and negative sides of the X-axis. Then an average of the two is calculated which is the jet half-width for each individual profile.

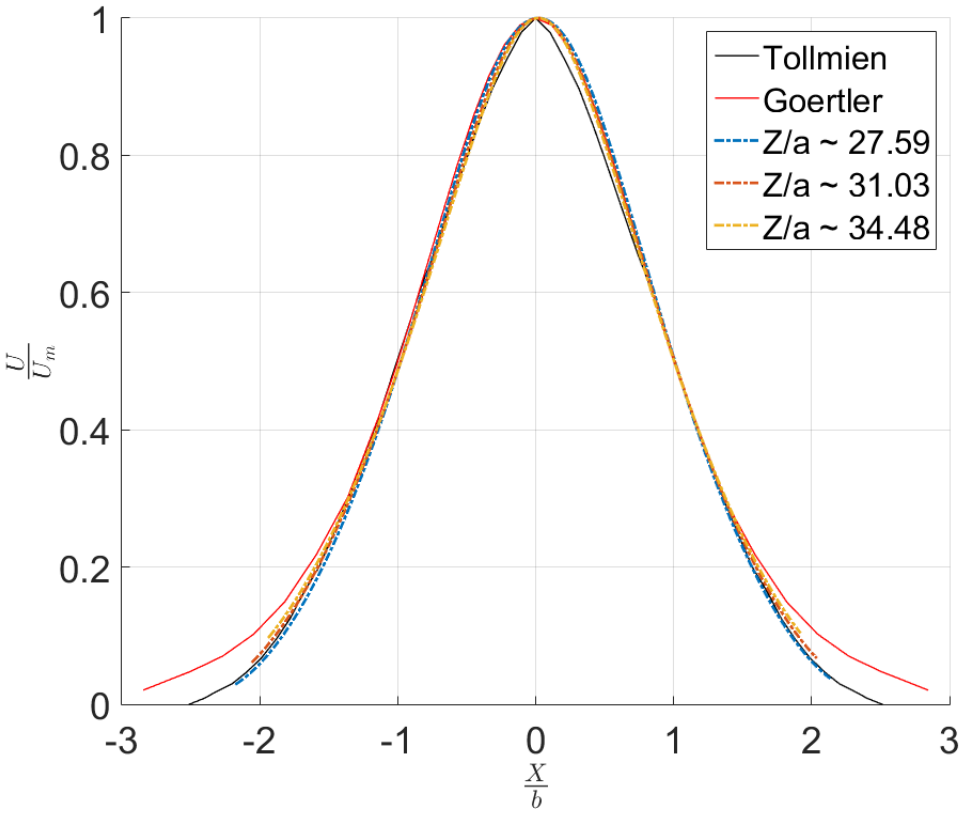

Figure 4.8: Analytical Solutions of Turbulent Planar Jets vs. RANS Spot M4 Set 1

For lower profiles in the combined region, the velocity profiles are observed to compare well against the analytical solutions. There is some very slight deviation towards the edges of the jets, but nothing that is a cause for concern.

For the highest profiles in the combined region, the velocity profiles are shown to compared and are well bounded by the analytical solutions. In general, the comparisons to the analytical profiles provides additional evidence and confidence the behavior is being

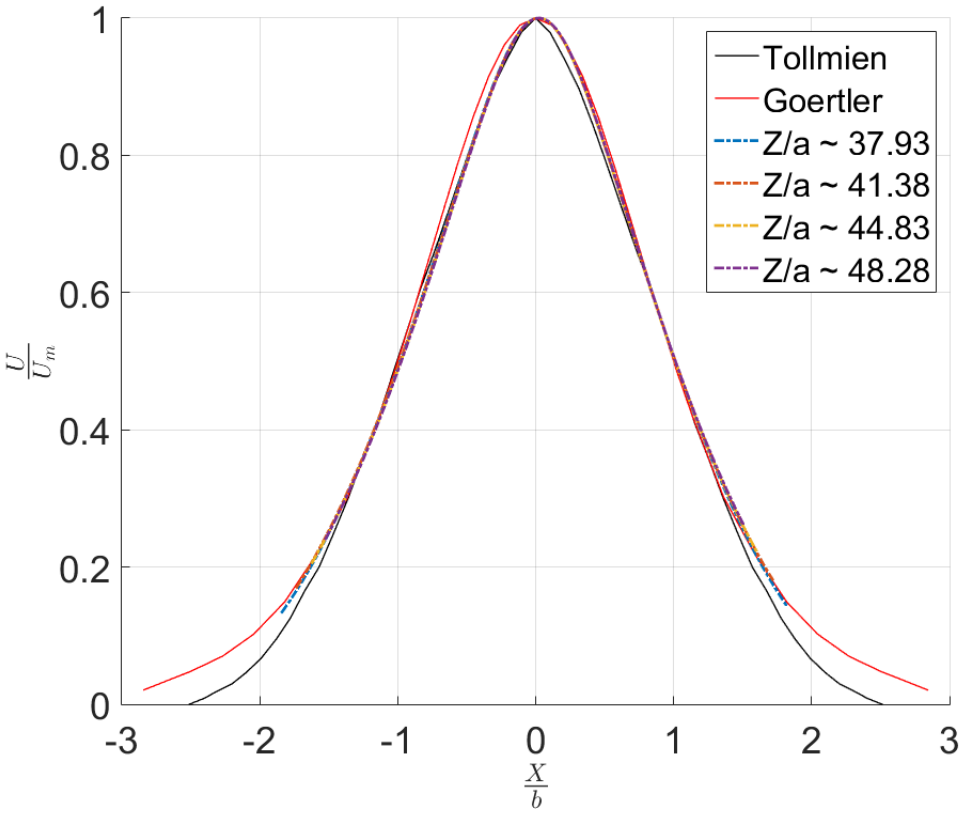

Figure 4.9: Analytical Solutions of Turbulent Planar Jets vs. RANS Spot M4 Set 2

resolved using this mesh.

4.2.4 Determination of Applicability - Case of Evidence

The discussions in subsections 4.1.1, 4.1.2, 4.1.3, 4.2.3 provide support for a working case of evidence meanings of determining mesh convergence. In this analysis, six different parameters are compared in either a quantitative or qualitative manner using quantities of interest, gradients of quantities, and comparisons to literature. It is observed that in each of the comparisons of simulation data, a converged result with a corresponding mesh could be determined. The quantities (streamwise velocity) of interest comparisons yielded a similar suggested converged result starting at the M3 mesh. Whereas, the gradient of the quantity

indicated the M4 mesh would be better suited based on the inclusion of mesh information. This is supported by the favorable qualitative comparison to the analytical jet profiles found in literature. It is then determined this approach is appropriate and recommended as an alternate means of determining measure convergence. This is useful in cases of internal flow with large aspect ratio changes in the geometry where localized meshing is effectively a requirement. Whereas, the observed order of accuracy techniques are shown to fail and proper guidance is not provided for these situations.

This analysis is quite extensive as compared to what is found in literature for similar studies (i.e. the number of parameters compared). Therefore, the follow criterion is recommended to balance determining a suitable converged mesh and reasonable use of resources. Also, this addresses the first question in section 1.6.

1. At least one quantity of interest (velocity field) that can indicate global behavior (such as highest gradients) should be compared between at least three levels of mesh refinement.

2. The gradient of the quantity of interest (such as vorticity) should be compared to confirm the previous determination and determine in any further refinement is needed.

3. If possible, a quantity of interest (global behavior) should be compared to analytical or higher order (such as LES or DNS) solutions.

4. The quantity of interest or the gradient of the quantity of interest needs to be compared using a quantitative metric such as percent difference or L^2 norm.

The following requirements are carried from the GCI to ensure the method is appropriately applied. These requirements are retained to ensure there is at least some basic structure and rigor retained for the mesh convergence analysis.

1. A consistent refinement strategy that refines both the global (base) size and the refinement regions sizes (not including near wall refinement) are reduced using the same multiplier.

2. The effective refinement factor defined in subsection 1.3.1 is at least $1.2 - 1.3$ between successive meshing levels based on guidance by Celik et. al. [62].

4.3 Methods for Determining Mesh Sensitivity

This section will discuss the creation of uncertainty/error bands using the GCI and $Error_{L^2}$ and the merits in internal flows in large aspect ratio changes in the geometry. The results from this section will be used in chapter 5 for the solution validation analysis to the TJWF experimental data. The uncertainty/error bands are determined for the streamwise velocity and Reynolds Stresses of the off-diagonal component at the characteristic heights for both methods.

4.3.1 Grid Convergence Index Uncertainty/Error Bands

The GCI is calculated for both quantities of interests using the observed order of accuracy of 1.45. It was determined using the centerline streamwise velocity profile observed order of accuracy discussed in subsection 4.2.2. These are calculated as absolute GCI quantities due to the low magnitude (close to or below unity) which can cause superfluously large uncertainty bands for a relative GCI calculation. A factor of safety of 3 is used in order for a conservative calculation of the uncertainty between M3 and M4 meshes. The uncertainty bands are shown in figure 4.10 and 4.11 for both velocity and Reynolds stress distributions in the converging region.

4.3.2 $Error_{L^2}$ Uncertainty/Error Bands

The $Error_{L^2}$ is calculated for each velocity profile or Reynolds stress profile and multiplied by two before being applied to the overall profile. The averaged or exact quantity

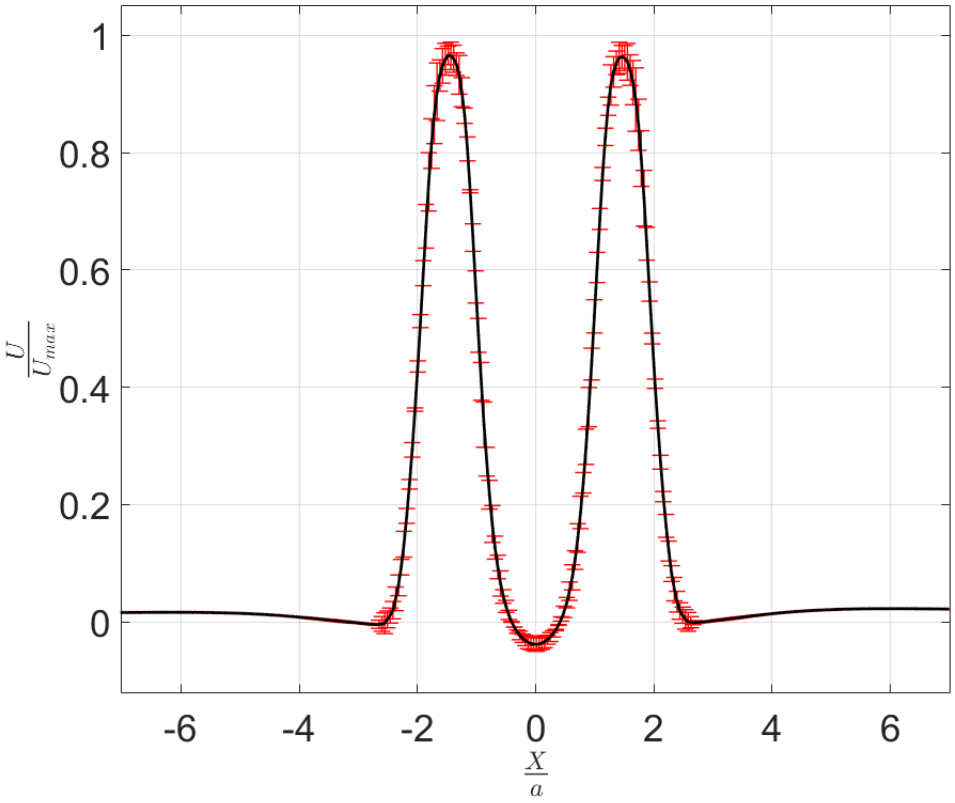

Figure 4.10: Velocity with GCI Uncertainty Bands at $\frac{Z}{a} = 1.72$

$\overline{f}$ is the M5 mesh result which is assumed to be the most accurate prediction. This is similar to the SEM applied to the experimental measurements. For the velocity profiles, the $Error_{L^2}$ is normalized by the maximum velocity of the profile before being applied with the following equation.

$$Error_{L^2}^{Max}(U) = \frac{Error_{L^2}(U)}{max(U(x(:), Z/a))} \tag{4.6}$$

The Reynolds Stress profile of the $\overline{u'v'}$ is normalized by either the largest value of the maximum $\overline{u'v'}$ or the absolute value of the minimum value $\overline{u'v'}$ along the profile.

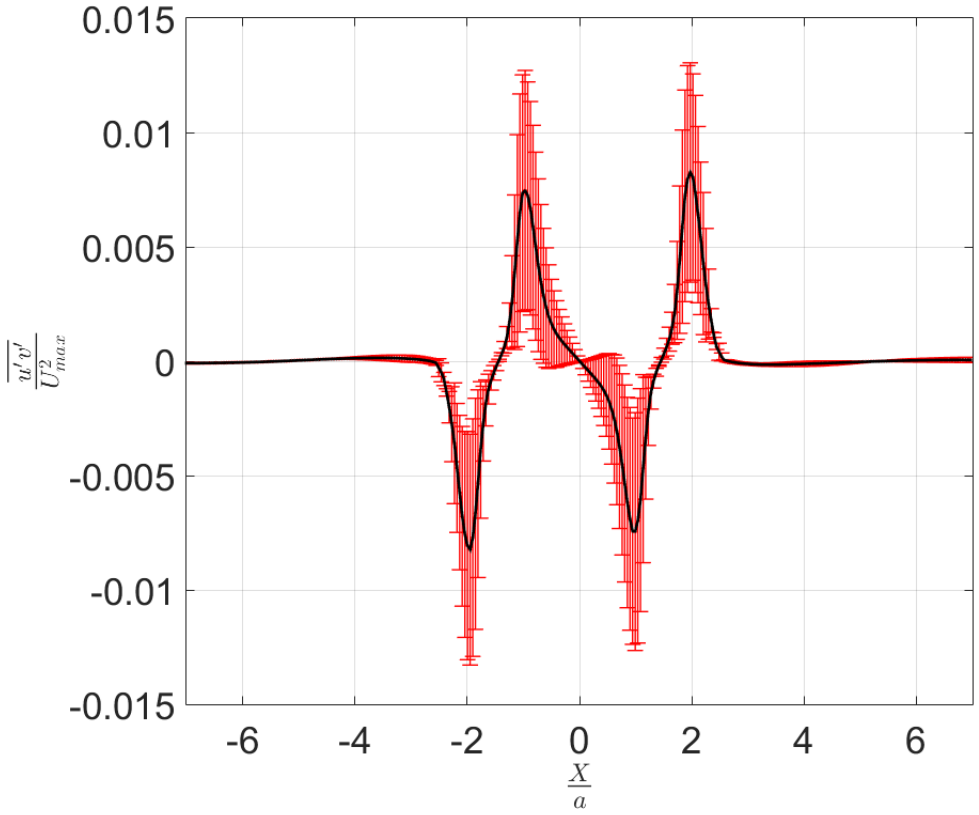

Figure 4.11: Reynolds Stress Profile with GCI Uncertainty Bands at $\frac{Z}{a} = 1.72$

$$Error_{L^2}^{Max}(\overline{u'v'}) = \frac{Error_{L^2}(\overline{u'v'})}{max[max(\overline{u'v'}(x(:), \frac{Z}{a}), |min(\overline{u'v'}(x(:), \frac{Z}{a}))|]} \tag{4.7}$$

The uncertainty bands are shown in figures 4.12 and 4.13 for both velocity and Reynolds stress distributions in the converging region.

4.3.3 Mesh Sensitivity Metrics Comparisons

Both set of uncertainty bands are observed to be reasonable and not a significant overshoot of the potential uncertainty (such as bands half the size of the graph). Though the GCI uncertainty bands for the $\overline{u'v'}$ stress are quite a notably larger than $Error_{L^2}$ bands.

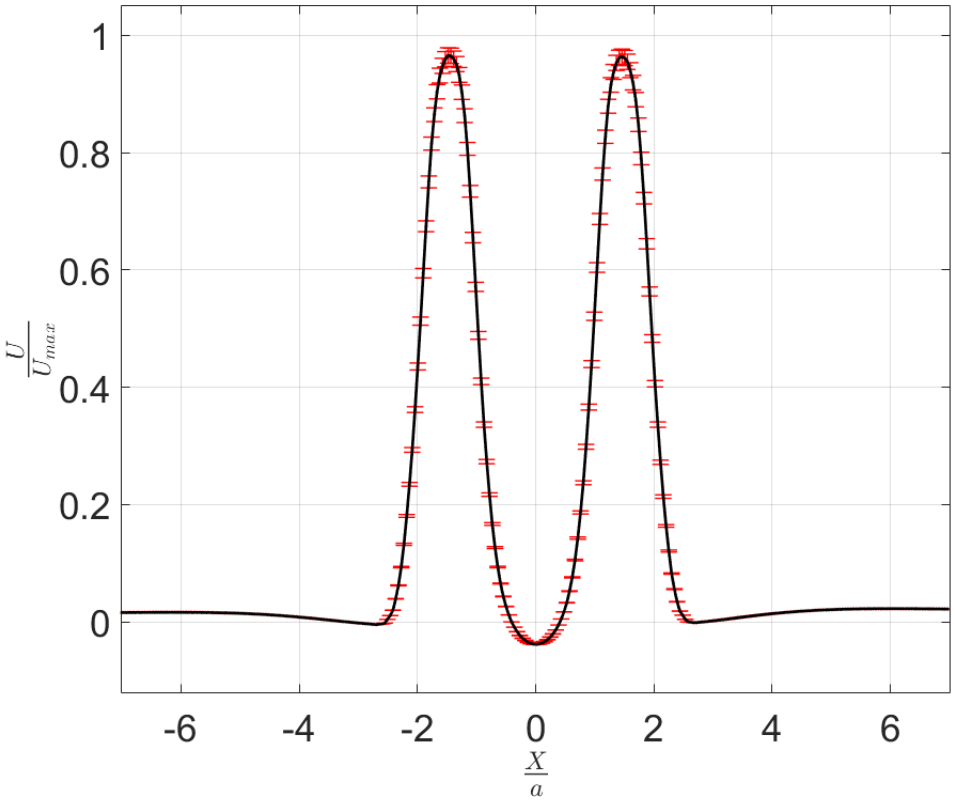

Figure 4.12: Velocity with $Error_{L^2}$ Uncertainty Bands at $\frac{Z}{a} = 1.72$

The $Error_{L^2}$ results in a more uniform band along the profiles which is expected due to the "global" value used. Whereas, the GCI bands change in sizes corresponding to the individual differences at those points between the M3 and M4 meshes. Additionally, the reader is reminded that several restrictions of the GRE and GCI methods are violated for this mesh triplet (i.e. mesh stratergy, non-asymptotic range, etc). This requires that the GCI uncertainty bands are not utilized in isolation.

The metrics discussed address the second question in section 1.6 which the answer is somewhat general enough. Clearly, $Error_{L^2}$ is quite general and easily applied when global data sets are available. It can be treated as analogy to how uncertainty bands are

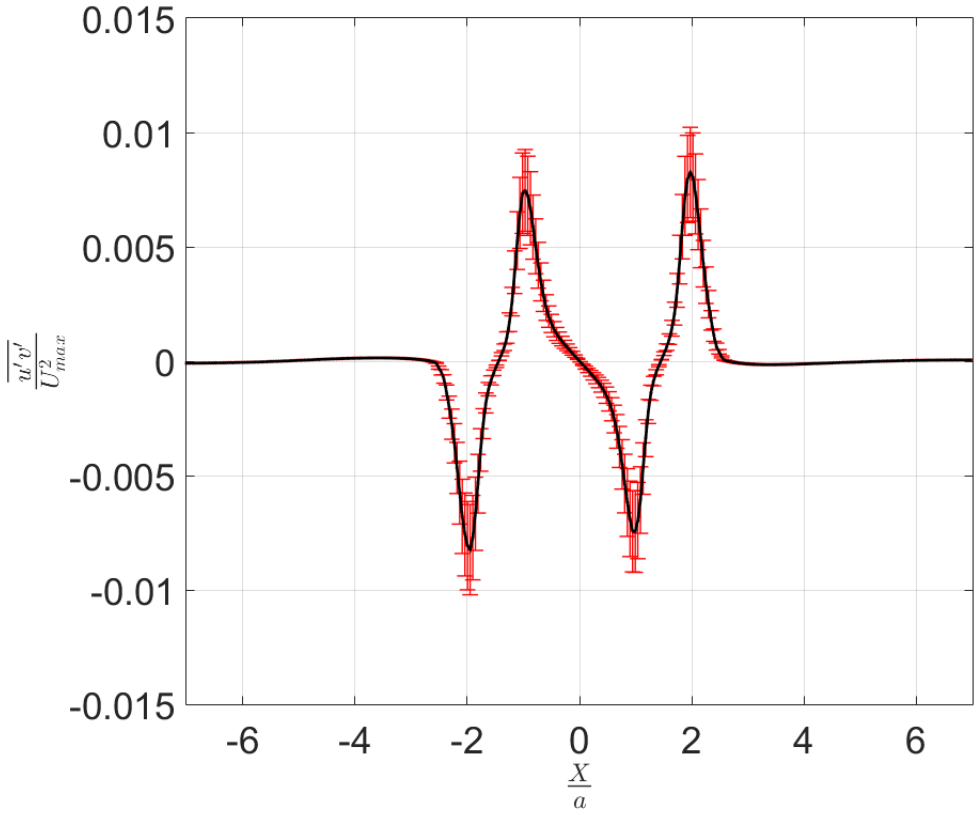

Figure 4.13: Reynolds Stress $\overline{u'v'}$ Profile with $Error_{L^2}$ Uncertainty Bands at $\frac{Z}{a} = 1.72$

developed for experimental efforts when uncertainty quantification is limited. Such as, uncertainty for a large set of experimental measurement points is determined using the uncertainty determined from one or two points. $Error_{L^2}$ should be normalized such that the data where unreasonably large uncertainty bands would not result but should be meaningful in purpose. The GCI "works" but with previously mention violations of requirements for usage. In this case, a factor of safety of 3 should be used even when the mesh triplet is used to provide a conservative but not artificially large (size of the graph) uncertainty. Additionally, $Error_{L^2}$ is significantly easier to implement, does not require very strict meshing strategies, and does not require significant work to determine a quantity to base

the observed order of accuracy on. It does not include meshing information or formal order that is a deficiency and could be investigated in the future.

5. SOLUTION VALIDATION ANALYSIS*

In this analysis, the validation is done by quantitatively and qualitatively comparing the available experiment results to the analogous simulation results. The results of the MP and CP, velocity profiles, and Reynolds Stress $\overline{u'v'}$ profiles are compared and contrasted. This is explicitly due to what experimental data was available at the time of writing for use in solution validation. Qualitative approaches such as color map and graphical comparisons are shown and discussed for the streamwise velocity and Reynolds stress $\overline{u'v'}$ profiles. A quantitative approach of percent difference and absolute difference calculations between experiment and simulation results are done for MP/CP, velocity profiles, and Reynolds Stress $\overline{u'v'}$. The reported quantities of interest are standard quantities found in twin planar turbulent jet literature and are meaningful for comparisons to the experimental works. It is likely that for a realistic situation involving twin jet-like geometry, that only qualities such as MP, CP, and velocity data would be meaningful for design and development activities such as discussed in chapter 1. All quantities are normalized based off the reported max velocity for the simulation or experiment as needed.

Based off the discussion in chapter 4, the RANS results for the spot refinement strategy created using mesh M4 will be used for comparisons. This mesh has been shown to be converged based off a posteriori comparisons using the mesh data itself and the analytical streamwise velocity profile solutions of turbulent free shear planar jets. The most readily available data sets discussed above allow for a simple comparison of the data using the experimental uncertainty and the simulation uncertainty. The uncertainty bands of the GCI

*Reprinted with permission from "Laser-Doppler measurements of the turbulent mixing of two rectangular water jets impinging on a stationary pool" by H. Wang et al., 2016, International Journal of Heat and Mass Transfer, 92, 206-227, Copyright 2016 by Elsevier.

*Reprinted with permission from "Particle image velocimetry measurements of the flow in the converging region of two parallel jets" by H. Wang et al., 2016, Nuclear Engineering and Design, 306, 89-97, Copyright 2016 by Elsevier.

metric with the centerline velocity profile observed order of accuracy and the $Error_{L^2}$ are shown and compared.

Ultimately, the question of "is this simulation validated using the available comparisons?" is discussed and determined if it is appropriately answered. This is meant to serve as a potential case study for solution validation with a high resolution data set and to potentially support the case of evidence method for the mesh convergence study in chapter 4. Additionally, questions 3-4 in section 1.6 will be addressed.

5.1 Merge and Combined Point Comparison

The merge and combined points for the LDV and PIV experiments and the spot M4 mesh are shown in Table 5.1. The merge point is presented as a range of value for both experimental results which is a consequence of the two measurement techniques. For the LDV measurements, the range is a occurs because of the experimentalists' spatial sampling where only the $\frac{Z}{a} = 1.72$ and 3.45 heights were probed [12]. The authors did not report additional measurements within these ranges which if sampled could have resulted in a more specific point identified. For the PIV measurements, the range of the MP is a consequence of two different magnification where the lower magnification (i.e. less resolution) resulted in the smaller observed MP [13].

The CP results are reported as single quantities, but the LDV result is potentially a consequence of no additional samples between $\frac{Z}{a} = 13.79$, $\frac{Z}{a} = 15.52$, and $\frac{Z}{a} = 17.24$. Though it has to be stated that these results in conjunction with the PIV results are the highest resolution ones available to date for this geometry and conditions.

The MP for the simulations are shown to be well bounded within both LDV and PIV experimental results. The percent difference for the lower range of the MP results is expectantly highest for the LDV and PIV lower bounds. The simulation prediction is quite close to the predictions of the higher bounds of LDV and PIV measurements with low %

Identifier	MP	$\%Diff_{MP}$	CP	$\%Diff_{CP}$
M4	3.30	n/a	21.35	n/a
LDV Exp	1.72-3.45	62.95-4.44	15.52	31.62
PIV Exp	2.66-3.50	21.48-5.88	16.84	23.62

Table 5.1: Merge and Combined Points - Solution Validation

differences. This is further encouraged by the PIV measurements' higher bounds results from the higher magnification which has a higher resolution used for the measurement in this region. This result indicates the spot M4 mesh is able to reasonably predict the behavior in merging region. It also suggests that the inlet jet conditions are sufficiently resolved enough when a length of 279.4 mm to develop the flow profile before the exhaust point is used.

The combined point for the spot mesh is approximately 31.62% and 23.62% different and predicted higher than both the LDV and PIV measurements. This is an expected result do the potential sensitivity of the inlet conditions on CP [7] and a consequence of using a turbulent model based on the Boussinesq assumption (isotropy of Reynolds stresses assumed). It is not believed the over-prediction of the CP is an indication that concern needs to be placed in the results.

5.2 Velocity Profiles at Characteristics Heights Comparison

Color Map Comparisons

The color maps for the simulation, LDV experiment, and PIV experiment of the velocity profiles are shown in figures 5.1,5.2,5.3,5.4. It is noted that the LDV and PIV measurements are shown as either a full field view or as a close up in the converging and merging regions of flow. A corresponding color map of the simulation results for each has been generated for comparison. Additionally, the color bars have been addressed to the corresponding minimums and maximums of each. The PIV measurement having a smaller

color map view is due to the measurement window being restricted to this size to ensure the features in these regions are captured properly. The spatial directions in LDV and PIV results are scaled using the jet width whereas the simulation results are not. This is meant to be shown as an example of a loose color map comparison and to point out the common pitfalls.

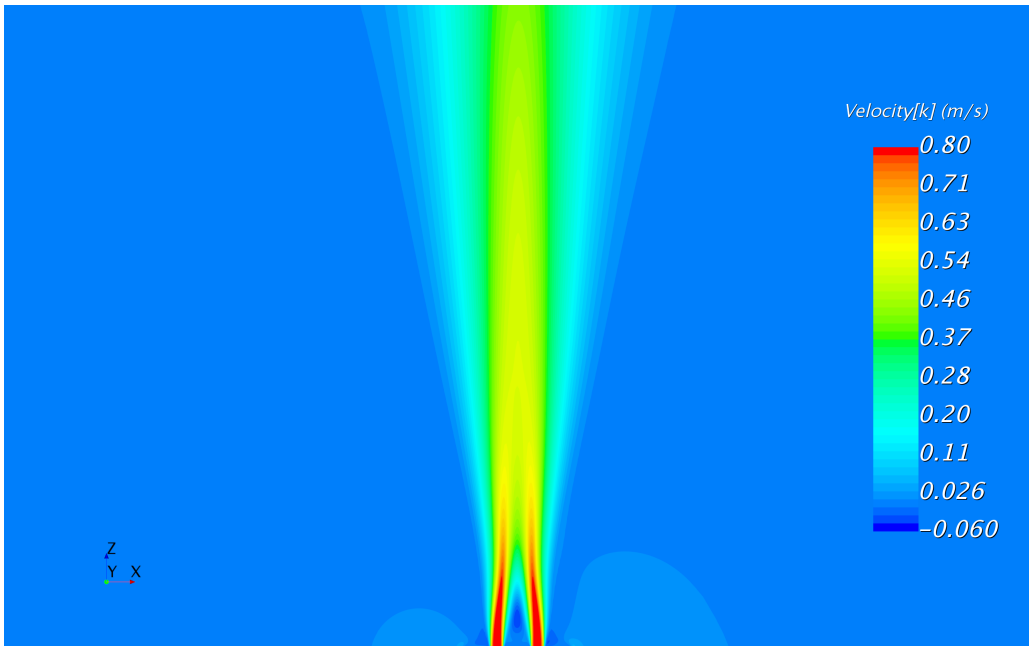

Figure 5.1: Color Map of Streamwise Velocity Field for the RANS M4 Spot Mesh

The simulation results are observed to capture the experimental measurements are shown to capture the flow behavior of the twin jets. The higher velocities in the jets and the low velocity region corresponding to the recirculation cells are seen in converging and merging regions for the simulation and PIV color map. The combined region does not have enough or clear enough information for the LDV measurement to make any true qualitative comparison based off this information. Though a single combined jet is

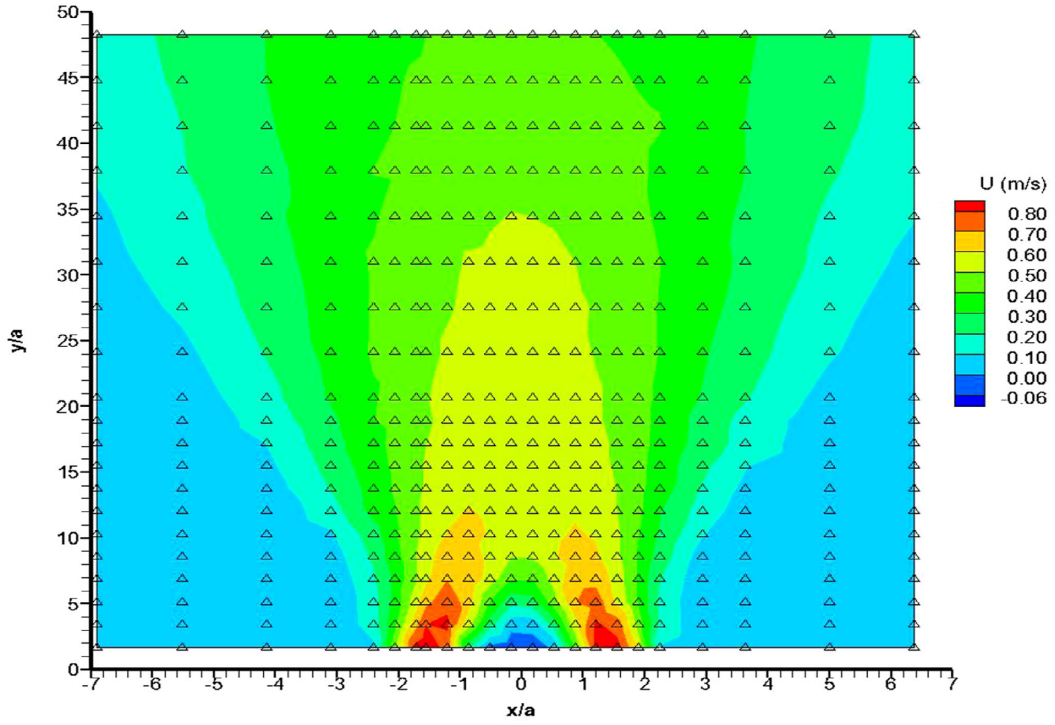

Figure 5.2: Color Map of Streamwise Velocity Field for the LDV Experiment [12]

observed for the simulations as in the LDV measurements. It is clear the comparison between the simulation and LDV color maps is quite inadequate and it is cautioned against comparisons such as this.

The "left" jet is observed to have a slight asymmetry in both LDV and PIV measurements that it is not captured by the simulation. The lack of asymmetry of this jet is due to the upstream conditions in the experiment not producing a fully developed profile at the point of exhaust which is desired for symmetry to be observed. The jet asymmetry is shown to be quite minor and is viewed to not significantly impact the simulation results which discussed further in the following subsection.

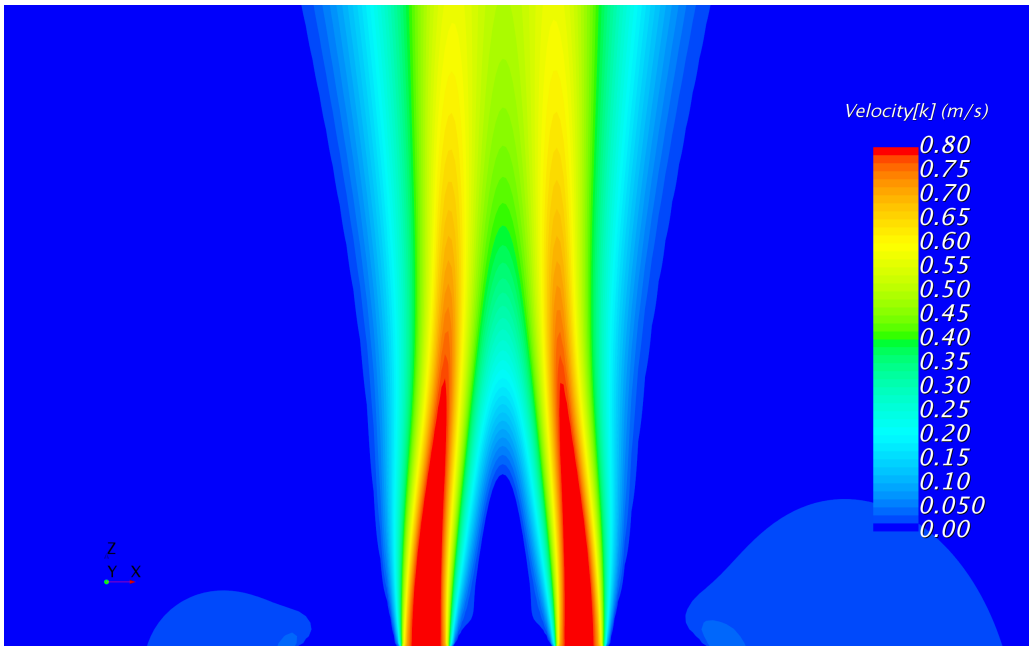

Figure 5.3: Color Map of Streamwise Velocity Field for the RANS M4 Spot Mesh - Zoomed in to Converging and Merging Regions

Graphical and Quantitative Comparisons

The velocity profiles at the different characteristic heights within the domain are shown in figures 5.5 and 5.6. These heights are selected to exemplify the simulation results in different characteristic regions of flow. In particular, the profiles in the converging region before the merge point and in the merge point are presented. The profiles near the combined point and well into the single self-similar jet region are presented as well. The PIV experimental results of this same case were not reported for the same heights as the LDV data and are not able to be included. The GCI and $Error_{L^2}$ uncertainty bands are shown separately for clarity. These uncertainty bands are presented in conjunction to the results in the following section to determine if the CFD results can be considered validated. This is explicitly pertaining to the overlapping of uncertainty bands for both the experimental measurements and the simulation results.

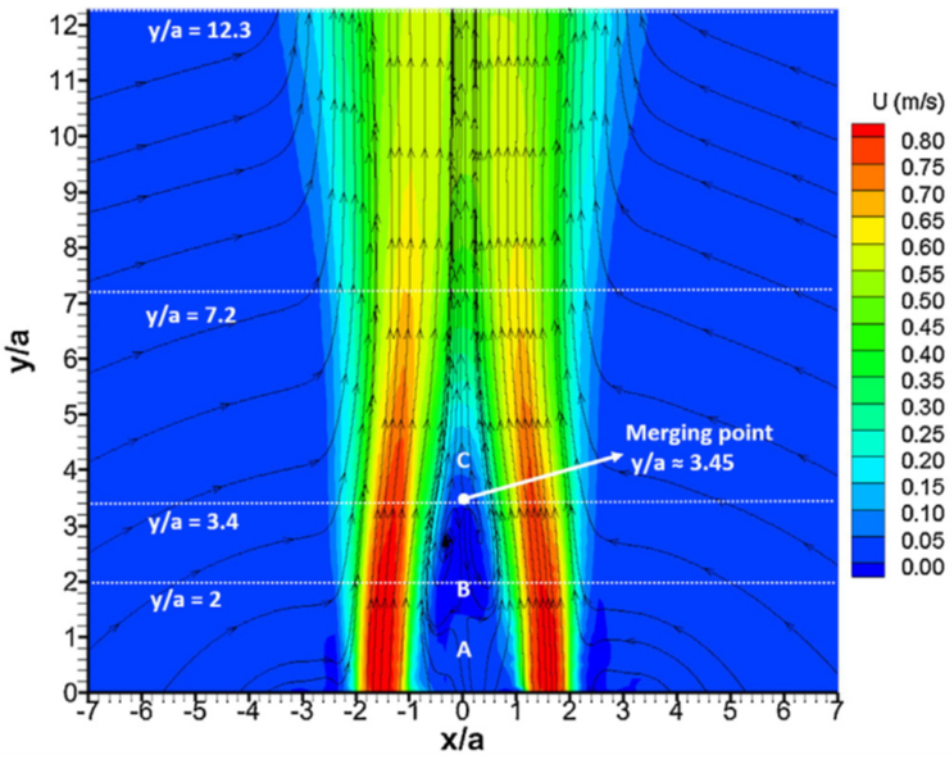

Figure 5.4: Color Map of Streamwise Velocity Field for the PIV Experiment [13] - Zoomed in to Converging and Merging Regions

The CFD predictions of the velocity profile in the converging region and at the merge point are observed to favorably compare to the experimental measurements. Some slight asymmetry of the "left" jet at the $\frac{Z}{a} = 1.72$ height is not captured which is consistent with previous observations in the preceding subsection. The lack of asymmetry prediction is not found to significantly impact the results downstream as the absolute difference is low at 0.068. The prediction at the merge point has no visible deficiencies observed and in general shows decent agreement based off the visual comparisons. Interestingly, the absolute differences calculated in some points were found to be high than initially expected for the lower profiles. For instance, for the $\frac{Z}{a} = 1.72$ profile, the absolute difference were as high as 0.2965 on the side of "left" jet which is due the small difference in position

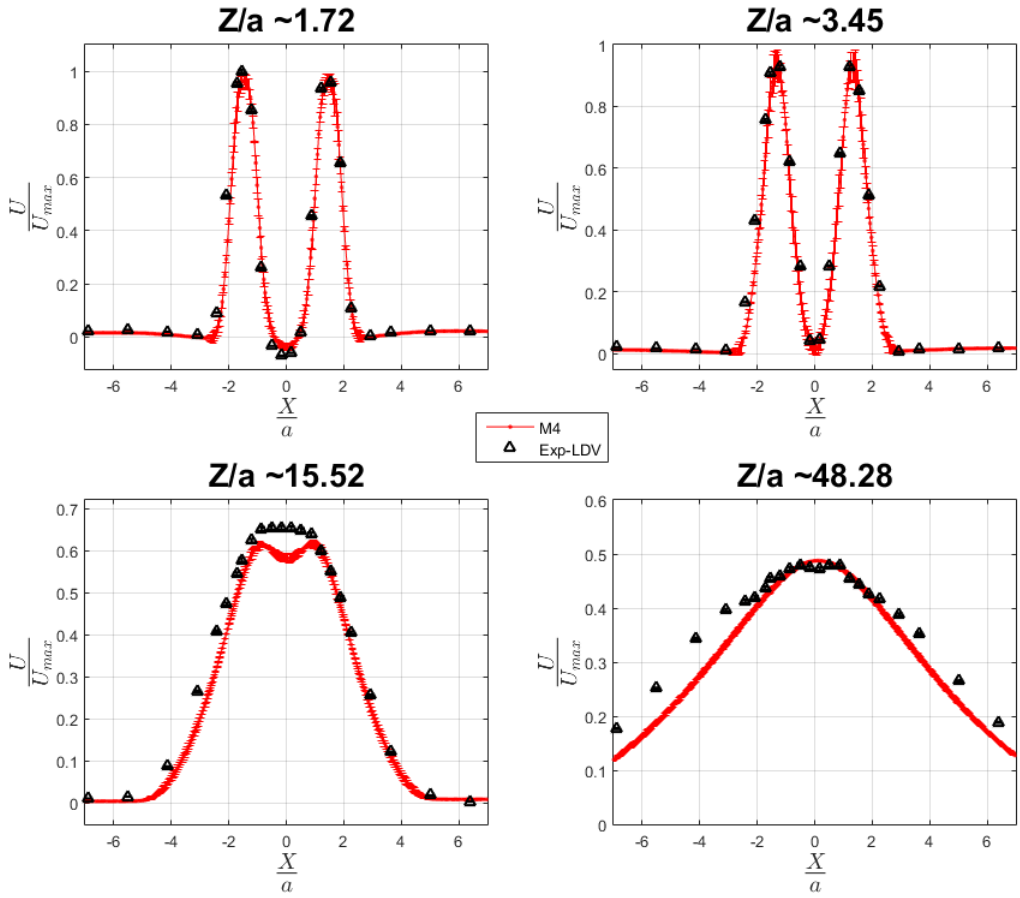

Figure 5.5: M4 vs. LDV Results - Streamwise Velocity Profiles with GCI Uncertainty Bands

between the measurement and prediction. It is not considered to be a large issue. The absolute difference in the peaks for the same profile was found to be small at 0.0684 and 0.0068 for the "left" and "right" jets. Similar absolute differences were found for the $\frac{Z}{a} = 3.45$ where the jets have the lowest percent differences of 0.0049 and 0.0736 for the "left" and "right" jets. The GCI and $Error_{L^2}$ uncertainty bands do overlap somewhat for these two profiles. Due to the small difference in position between the measurements and simulation results, these comparisons could actually be used against the solution being

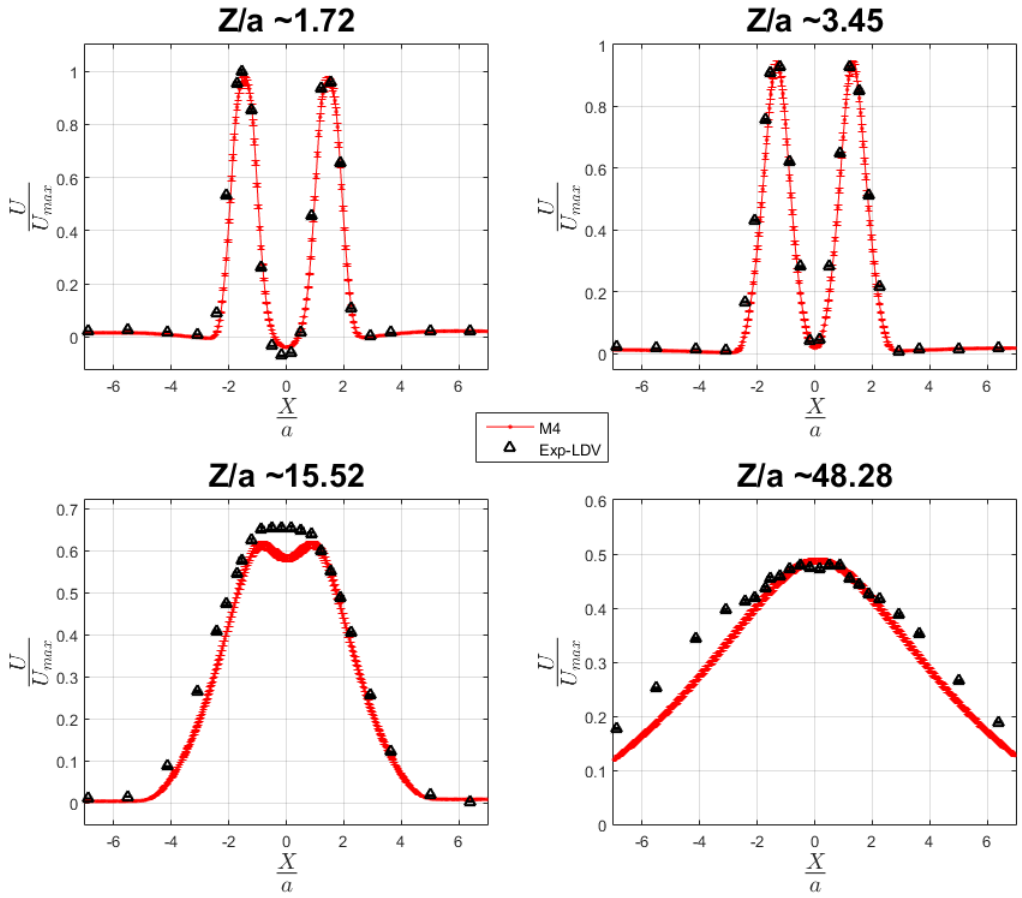

Figure 5.6: M4 vs. LDV Results - Streamwise Velocity Profiles with $Error_{L^2}$ Uncertainty Bands

validated. For these two profiles, this seems very unreasonable based on the graphical (i.e. the two profiles without considering the uncertainty bands) and MP comparisons which are viewed to support validation.

The CFD results near the combined point ($Z/a = 15.52$) confirm the results observed in the previous section of the over-predicted CP. The experimental measurements of the two jets have merged into a single jet and reached a peak centerline velocity noticeably before the simulation predicts. Whereas the CFD predicted profile is still in the process

of merging into a single jet. This is seen by the twin peaks of two jets still merging in the simulation results whereas the experiment is showing one jet profile. It is noted, the overall velocity profile is captured excluding the peak of the profile ($-2 < \frac{X}{a} < 2$). This is confirmed by the absolute differences are at a small at 0.039 and 0.0207 at $\frac{X}{a} = |2|$ for the "left" and "right" peaks. Whereas, the highest absolute difference between the two peaks is found to be 0.062 at $\frac{Z}{a} = -0.172$. Both GCI and $Error_{L^2}$ uncertainty bands do not provide good coverage as compared to the small experimental uncertainty implying low support for validation. In this profile, it is a little less clear cut to argue it supports the validation effort, but excluding the center of the profile the majority of the results compare favorably.

The single self-similar jet profile at $Z/a = 48.28$ is observed to have a strong comparison between the CFD and experiment in the peak region of the profile. The left and right "legs" are found to be under-predicted by the CFD results. The absolute differences in this profile is actually a bit higher where the majority of the points due to the aforementioned under-predicted "legs". The lower experimental uncertainty in these measurements were of interest and have been investigated. It is suspected the experimental data collected in the upper profile were not collected for a long enough period of time. This area has a much lower velocity than in the converging region. Which requires significantly more averaging time for the velocity profile, than in the converging region, to reach a statistically stationary state (i.e. measured for a substantially long enough period of time). The uncertainty bands in this region is likely not capturing the true uncertainty at those points. This is due to the uniform uncertainty applied for all points along this profile that is not directly associated with this profile. The low magnitude of the experimental uncertainty and simulation uncertainties, using both GCI and $Error_{L^2}$ methods, made a validation comparison difficult. It again would not readily support the case for the solution to be argued to be "validated".

In general, the simulation results for the lower profiles are considered to strongly support the validation case even with low overlapping of experimental and simulation uncertainty bands. This is due to an overall low absolute difference between the results. The combined point profile also suffers from low uncertainty overlap but the absolute differences were found to be low. This is excluding the peak of the profile where the simulation shows clear deficiencies. For the combined region profile, the top of the jet shows a strong comparison between the simulation and experiment but the "legs" suffer from a significant under-prediction which is believed to be an issue with the experiment.

5.3 $\overline{u'v'}$ Stress Profile at Characteristic Heights Comparison

Color Map Comparisons

The color maps for the simulation, LDV experiment, and PIV experiment of the $\overline{u'v'}$ profile are shown in figures 5.7,5.8,5.9,5.10. It is noted that the PIV measurements are shown as a close up in the converging and merging regions of flow. The spatial directions in LDV and PIV results are scaled using the jet width whereas the simulation results are not. The LDV measurements are shown normalized with the maximum measured velocity which is done similarity for the simulation colormap for the full field measurement. The PIV color map is not normalized and the simulations again are not normalized to reflect this.

In each figure, four distinct regions of large positive and negative shear stress regions are observed which is expected based off the literature. It is worth noting that these results are of flipped magnitudes than seen in figure 1.14. This is due to the datum and the direction of the spanwise being flipped. For the LDV and simulation colormaps, the shear regions are observed to extend well into the combined region which is observed in the simulation. There is an observed reduction of the Reynolds stress component which is due to the velocity of the combined jet slowly reducing in magnitude going downstream.

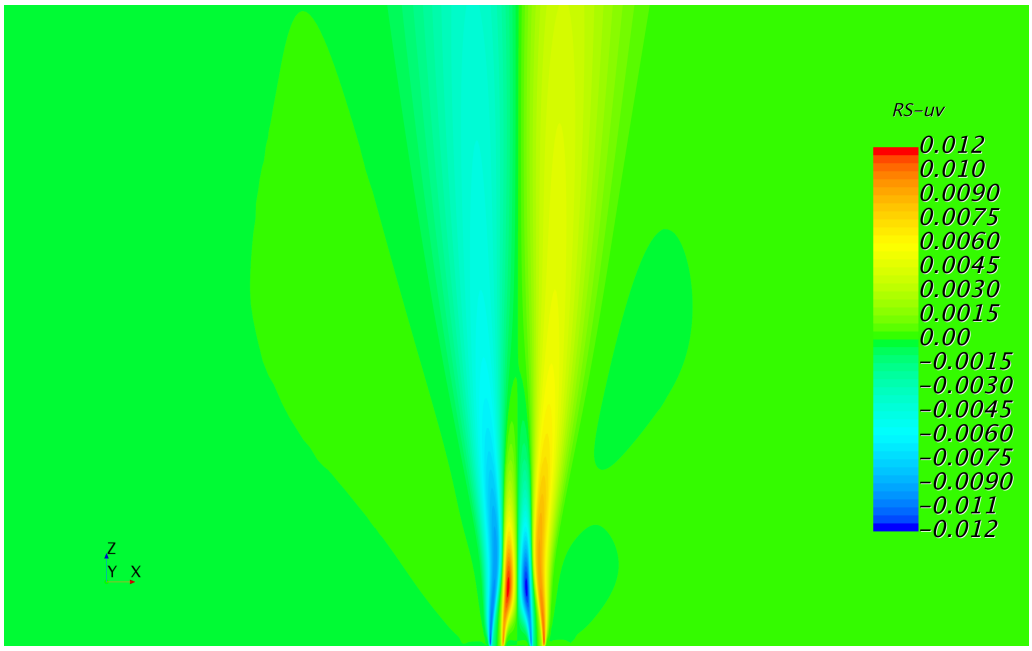

Figure 5.7: Color Map of $\overline{u'v'}$ Field for the RANS M4 Spot Mesh

The higher fidelity PIV measurements are captured by the simulation results in that the elongated structures show a good comparison. It is worth noting that these are in regions were entrainment is expected to be significant on the edges of the jets and in the recirculation region as seen in literature. The shear layer that occurs between the jet flow and the entrained flow which causes large shear stress regions to be observed. In the case of the converging and merging regions between to the two jets, the jets are interaction and beginning to exchange momentum which is expressed by the large pockets of positive and negative $\overline{u'v'}$ stress which then dissipates as the jets fully merge as seen in the LDV measurements. For the Reynolds stress $\overline{u'v'}$ component, the color maps provide a reasonable qualitative comparison, but this is still dubious and analysts again should push towards more direct forms of comparison.

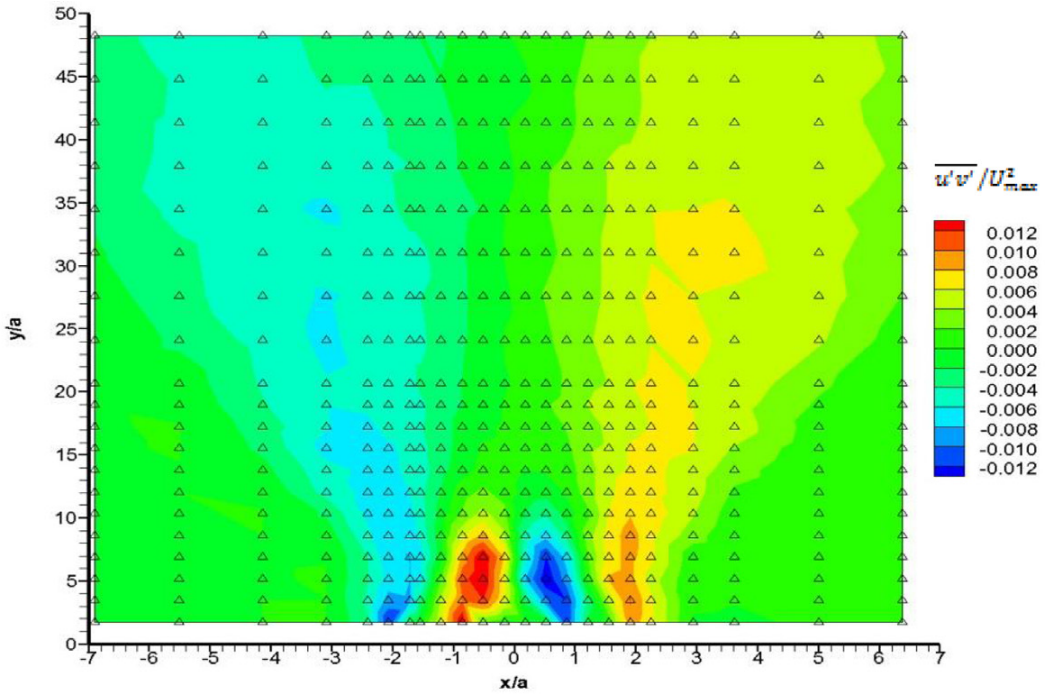

Figure 5.8: Color Map of $\overline{u'v'}$ Field for the LDV Experiment [12]

Graphical and Quantitative Comparisons

The Reynolds stress profiles of the off-diagonal component in the streamwise and spanwise directions at the previously mentioned characteristic heights are reported in figures 5.11 and 5.12. The CFD stresses profiles were constructed a posteriori using the Boussinesq assumption (section 3.4.2) with the calculated turbulent viscosity and gradients of velocity on the measurement plane. This is required due to the Reynolds stresses are not directly calculated when two equation turbulence models are used. The PIV experimental results of this same case were not reported for the same heights as the LDV data and are not able to be included. Again, the uncertainty bands for both GCI and $Error_{L^2}$ are shown in the separate graphs for clarity.

The Reynolds stress $\overline{u'v'}$ component in the converging and merging regions are pre-

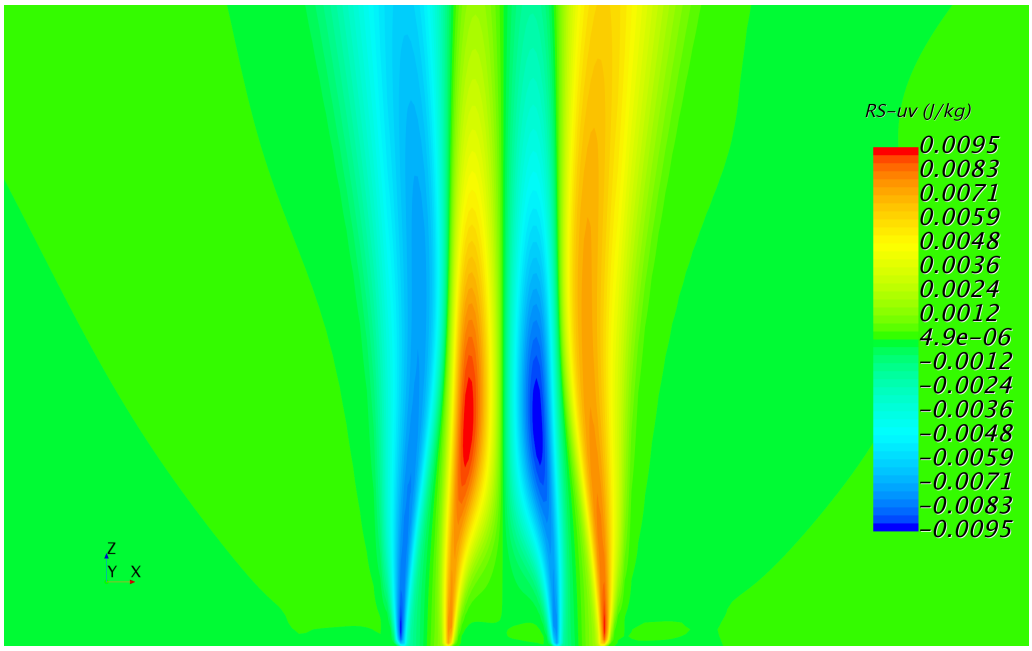

Figure 5.9: Color Map of $\overline{u'v'}$ Field for the RANS M4 Spot Mesh - Zoomed in to Converging and Merging Regions

dicted well in the general shape by the CFD simulation. The profiles are observed to experience significant under prediction of the spikes in the profiles at $\frac{X}{a} = |0.862|, |2.07|$ for the $\frac{Z}{a} = 1.72$ profile and $\frac{X}{a} = -2.069, -0.517, 0.862, 1.9$ for the $\frac{Z}{a} = 3.45$ profile. In the spikes, the maximum absolute difference is highest at 0.0105 and 0.00731 for the $\frac{Z}{a} = 1.72$ and $\frac{Z}{a} = 3.45$ profiles. The absolute difference drastically reduces outside of the highest points of the spikes to minuscule amounts. The GCI uncertainty bands show large overlapping with the experimental uncertainty in the spike regions which is somewhat surprising. The $Error_{L^2}$ bands for these profiles are observed to be much smaller for the $\frac{Z}{a} = 1.72$ profile which undermines the validation support from the GCI metric. This is similarly seen for the $\frac{Z}{a} = 3.45$ profile which has a larger uncertainty in the spikes but again the same overlap is not observed. Additionally, this behavior from the simulation of strongly under-predicting the spikes is expected due to the assumed isotropy of the

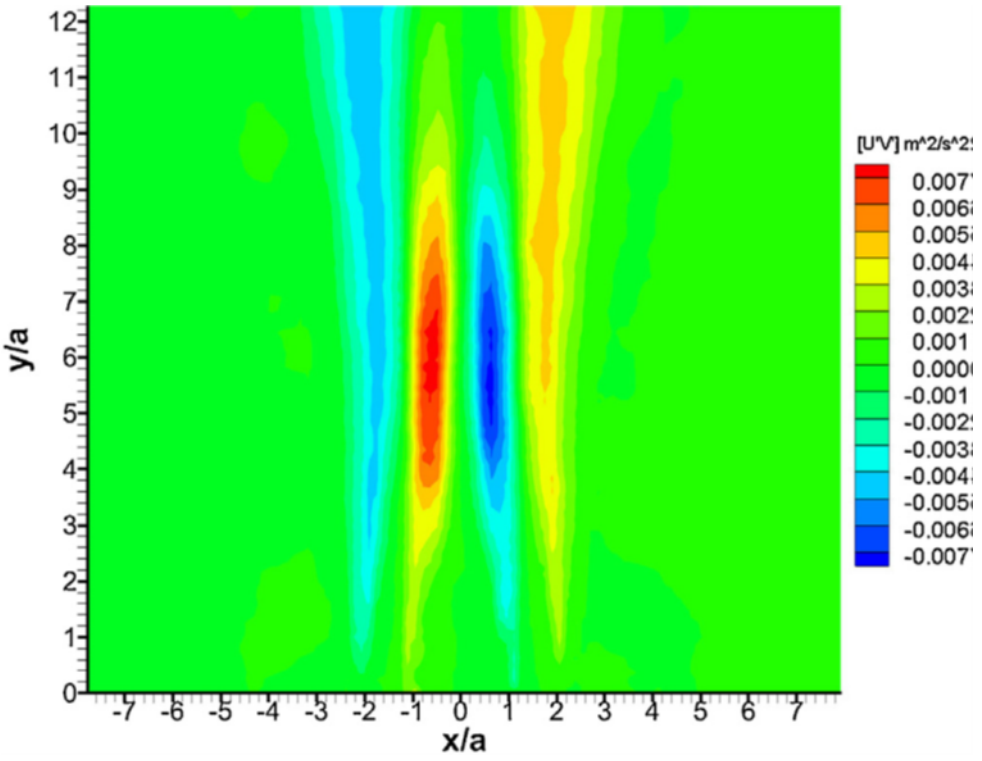

Figure 5.10: Color Map of $\overline{u'v'}$ Velocity Field for the PIV Experiment [13] - Zoomed in to Converging and Merging Regions

Reynolds stress tensor. Excluding the highest point of the spikes, the two profiles provide another amount of support that the solution results are validated.

For the CP Reynolds stress $\overline{u'v'}$ profile ($\frac{Z}{a} = 15.52$, the general shape is captured but significant structural differences are seen. Aroung the $\frac{X}{a} = |0.25|$, the separate positive and negative peaks corresponding to the still merging jets are observed but the absolute differences are still low in this region. Whereas, the experimental data is observed to be mostly flattened in this region. The peaks in the experimental profile are under-predicted by approximately half the total magnitude corresponding to absolute differences of 0.0053 for the left negative peak and 0.0034. These results are still in a region of higher anistropy of the Reynolds stresses which is not surprising to see under-prediction by the RANS

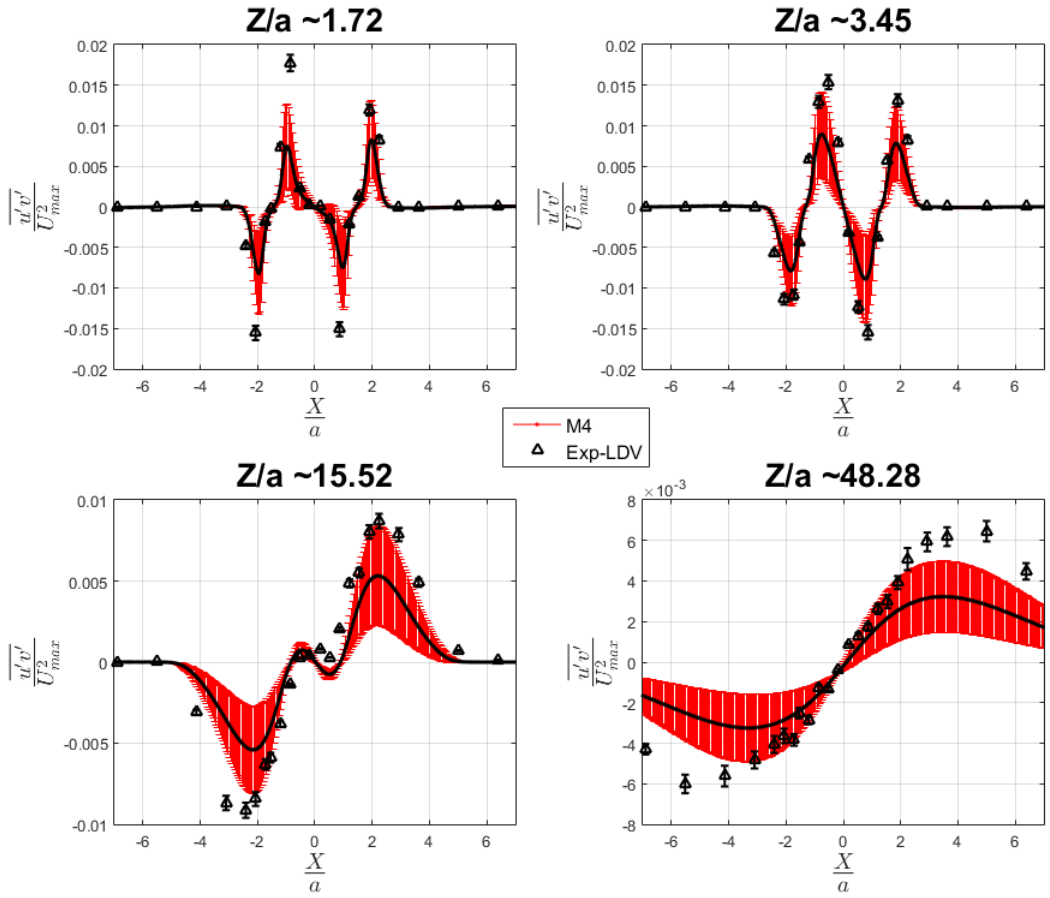

Figure 5.11: M4 vs. LDV Results - $\overline{u'v'}$ Profiles with GCI Uncertainty Bands

model. The capturing of the shape does provide support for validation. There is little overlap of the $Error_{L^2}$ uncertainty while the GCI uncertainty is quite large and almost entirely encapsulates the experimental results. The GCI overlap is again inconsistent and does not truly support a validation conclusion.

The combined region profile shows similar under and over prediction of the Reynolds stress profiles of the experiment results by the simulation. The largest absolute error of 0.0035 and 0.0036 corresponding to the maximum and minimum $\overline{u'v'}$ which is not surprising. These results do capture the shape of the profile very well, but the Reynolds stress

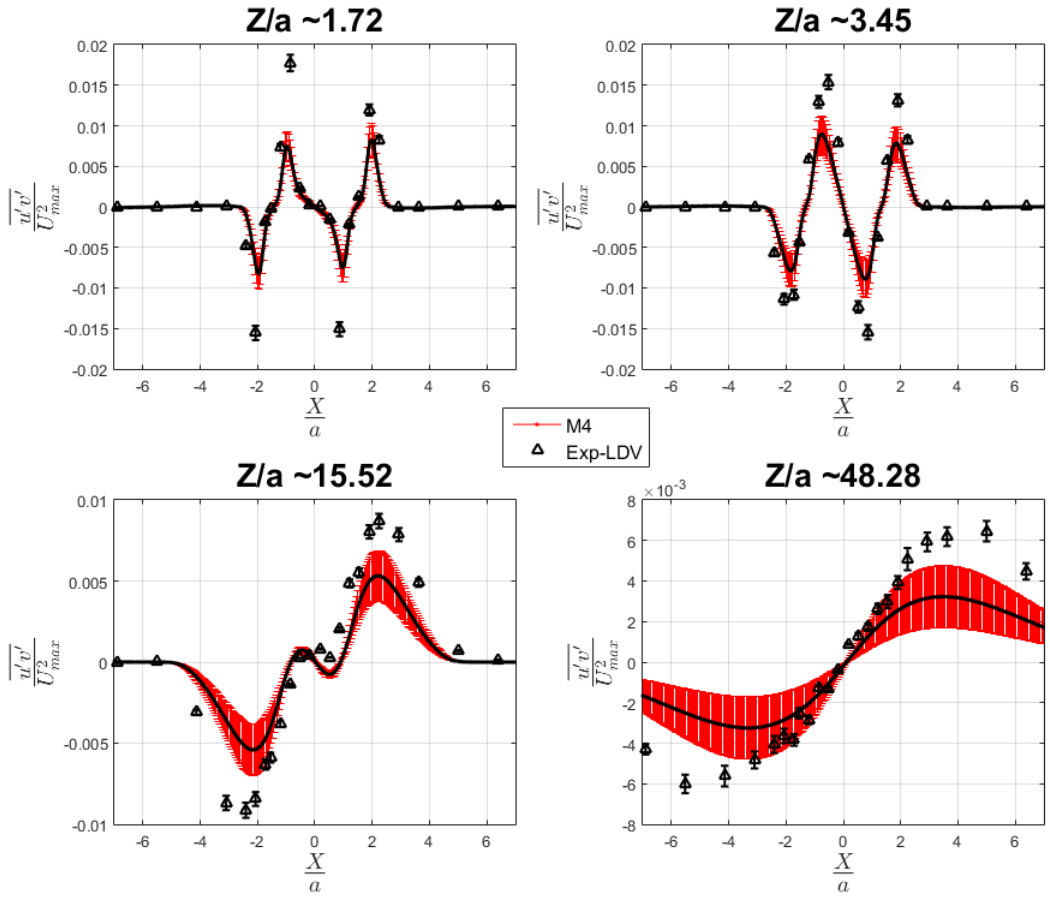

Figure 5.12: M4 vs. LDV Results - $\overline{u'v'}$ Profiles with $Error_{L^2}$ Uncertainty Bands

predictions should be much closer in magnitude since the anistoropy is heavily reduced. Again, these measurements where these large discrepancies are observed are in regions which experimental measurements may not have been collected for a long enough period of time. This could lead to the larger stresses we observe in the profiles. Interesting, the GCI and $Error_{L^2}$ are very close in magnitude with each other overall. There is overlap with the experimental uncertainty bands from $-3.5 < \frac{X}{a} < 2$ to both sets of simulation uncertainties.

The general trends are captured based off these visual comparisons and the expected

deficiencies were observed for the simulation results. The GCI and $Error_{L^2}$ error bands do not give significant confidence as a usage of a validation metric since there is little overlap with the experimental uncertainty.

5.4 Is the Calculation Validated?

Based on the adequately predicted experimental results by the simulation, the simulations are believed to be validated with some caveats. This is supported by the basic quantitative and qualitative comparisons except for areas that are well characterized for their deficiencies. These deficiencies are not felt to be deal breakers and are considered to be areas that can be approached for future works to improve the simulations.

The quantitative metrics were focused on merge/combined points of the twin jets and for each of the profiles of velocity and Reynolds stresses $\overline{u'v'}$ at characteristic heights. The merge point was found to be bounded by both LDV and PIV measurements while the combined point showed a notable over-prediction. The CFD over-prediction was approximately 31.62% and 23.62% different above the LDV and PIV measurements. This is not considered to be greatly worrying because ultimately the dimensionalized difference was around one to two centimeters which is quite small.

Absolute differences for each characteristic velocity profile was used to determine the how far were the predictions from the experiment as a quantative measure. For the majority of the profiles, the absolute differences were found to be reasonably low excluding three situations. The first is a slight offset of the corresponding points between the experimentally measured and the simulation predicted velocities which can result in an abnormally large difference in areas of large gradients. The second being regions where the measured velocity profile may have been collected for an insufficient amount of time. Such as towards the upper range of the measurement profile where lower velocities require significantly longer measurement times. The third was where the CFD prediction of the higher

combined point resulted in a velocity profile that was not combined where the experiment was observed to be.

For the Reynolds stress $\overline{u'v'}$ profiles, the simulations were observed to predict the general behavior of the flow, but the absolute differences were quite high in certain regions. These regions were where the predictions were expected to under-predict the Reynolds stress such as high anisotropic regions of flow. For the combined point profile where a considerable anisotropic region is still experienced, the behavior of the flow was captured but the peaks were again under predicted. The absolute differences in this region were higher but not terrible. The combined jet region where the self-similar jet behavior could be observed experienced the same higher absolute difference behavior in the "legs". Though, this last profile is difficult to conclude if the simulation is actually deficient or due to aforementioned issues with the experimental measurements in that region.

The qualitative means of comparing the color maps and graphical profiles provided insight into if the flow behavior was sufficiently predicted in the simulations. It was observed that the overall general trends and the behavior was predicted correctly while the previously mentioned deficiencies were identified using the graphical comparisons. The color maps were useful in determining qualitative flow comparisons, but were limited in their scope for discussing validation.

Using the discussion above, it is felt that the question 3 in section 1.6 is answered. It is suitable to show solution validation through basic quantitative and qualitative metrics that investigate meaningful quantities of the flow. It is felt that engineering judgment and ultimately what experimental data is available can help determine the extent of what needs to be compared. Ultimately, it is found the uncertainty bands were not useful for determining validation in this solution validation analysis.

With regards to question 4 in section 1.6, it was found by the author that these metrics were easy to apply for solution validation. Though, certain metrics were found to not be

as useful as others and require additional study.

6. SUMMARY AND CONCLUSIONS

Solution V&V methodologies for CFD simulations were analyzed using the twin jet semi-classical case to find or determine a meaningful yet simple solution verification technique. A solution validation analysis was conducted to ensure the predicted behavior was a reasonable approximation of reality. This was done using data collected from experimental campaigns in the TJWF at Texas A&M University.

The solution verification investigation resulted in the following case of evidence methodology to be recommended for usage of mesh convergence. It is felt this methodology is general and simple enough that it can be applied in many cases where others fails. For instance, internal flows with high aspect ratio changes of geometry in areas of interest which are found in SFRs and VHTRs. This is exemplified by the twin jet case which is where GCI is not able to be applied properly. The GCI issues are due to the inability of reaching the asymptotic region due to computational requirements. The case of evidence methodology is recommended as follows.

1. At least one quantity of interest (velocity field) that can indicate global behavior (such as areas of highest gradients) should be compared between at least three levels of mesh refinement.

2. The gradient of the quantity of interest (such as vorticity) should be compared to confirm the previous determination and be used to determine if any further refinement is needed.

3. If possible, a quantity of interest (global behavior) should be compared to analytical or higher order (such as LES or DNS) solutions.

4. If possible, a quantity of interest or the gradient of the quantity of interest needs to be

compared using a quantitative metric such as percent difference, absolute difference or L^2 norm.

The solution validation analysis was used to find that the twin jet simulations using steady RANS with the standard $\kappa - \epsilon$ turbulent model could provide a decent prediction of reality. Simple qualitative comparisons of color maps and extensive graphical comparisons were shown to be of value in determining the strength and weaknesses of the CFD efforts. The quantitative comparisons of MP/CP and absolute differences of the velocity and Reynolds stress $\overline{u'v'}$ profiles at characteristic heights were used as well. These resulted in confidence that the behavior compared in the qualitative metric was reflective in quantitative comparisons. In general, the uncertainty bands from the GCI and $Error_{L^2}$ for mesh sensitivity were not found to be particular useful. It is understandable that there is considerable investigative effort (mesh sensitivity metrics) occurring in this area (uncertainty quantification), but the value is lost on the author at the time of writing for this specific analysis.

REFERENCES

[1] "Sodium-Cooled Fast Reactor (SFR)," 2016.

[2] "Very-High-Temperature Reactor (VHTR)," 2016.

[3] D. Tenchine, "Some thermal hydraulic challenges in sodium cooled fast reactors," *Nuclear Engineering and Design*, vol. 240, no. 5, pp. 1195–1217, 2010.

[4] B. M. King, *Natural Circulation Scaling of a Pressurized Conduction Cooldown Event in the Upper Plenum of the Modular High Temperature Gas Reactor*. Masters, Oregon State University, 2012.

[5] C. A. J. Fletcher, *Computational Techniques For Fluid Dynamics 1*. Berlin: Springer-Verlag, 2nd ed., 1987.

[6] L. J. S. Bradbury, "The structure of a self-preserving turbulent plane jet," *Journal of Fluid Mechanics*, vol. 23, no. 1, pp. 31–64, 1965.

[7] E. A. Anderson and R. E. Spall, "Experimental and Numerical Investigation of Two-Dimensional Parallel Jets," *Journal of Fluids Engineering*, vol. 123, pp. 401–406, 2001.

[8] N. W. M. Ko and K. K. Lau, "Flow structures in initial region of two interacting parallel plane jets," *Experimental Thermal and Fluid Science*, vol. 2, no. 4, pp. 431–449, 1989.

[9] M. Crosskey and A. Ruggles, "UTK Twin Jet Water Facility Computational Fluid Dynamics Validation Data Set," in *Proceedings of International Congress on Advances in Nuclear Power Plants (ICAPP '14)*, (Charlotte, North Carolina), pp. 1940–1945, American Nuclear Society, 2014.

[10] C. Wiggins and A. Ruggles, "Comparison of UVP and PIV Measurements of the Mixing of Parallel Vertical Jets," in *Advances in Thermal Hydraulics 2014, ATH-14*, (Reno, Nevada), pp. 417–426, 2014.

[11] CD-Adapco, "Star-CCM+ 11.04.012 User's Guide," 2016.

[12] H. Wang, S. Lee, Y. A. Hassan, and A. E. Ruggles, "Laser-Doppler measurements of the turbulent mixing of two rectangular water jets impinging on a stationary pool," *International Journal of Heat and Mass Transfer*, vol. 92, pp. 206–227, 2016.

[13] H. Wang, S. Lee, and Y. A. Hassan, "Particle image velocimetry measurements of the flow in the converging region of two parallel jets," *Nuclear Engineering and Design*, vol. 306, pp. 89–97, 2015.

[14] J. E. Brunings, "LMFBR Thermal-Striping Evaluation," tech. rep., Rockwell International, Canoga Park, CA, 1982.

[15] Y. Ieda, I. Maekawa, T. Muramatsu, and S. Nakanishi, "Experimental and Analytical Studies of the Thermal Stratification Phenomenon in the Outlet Plenum of Fast Breeder Reactors," *Nuclear Engineering and Design*, vol. 120, pp. 403–414, 1990.

[16] S. K. Choi, T. H. Lee, Y. I. Kim, and D. Hahn, "Numerical analysis of thermal stratification in the upper plenum of the MONJU fast reactor," *Nuclear Engineering and Technology*, vol. 45, no. 2, pp. 191–202, 2013.

[17] A. J. Neylan, D. V. Graf, and A. C. Millunzi, "The Modular High Temperature Gas-Cooled Reactor (MHTGR) in the U.S.," *Nuclear Engineering and Design*, vol. 109, pp. 99–105, 1988.

[18] W. L. Oberkampf and T. G. Trucano, "Verification and validation in computational fluid dynamics," *Progress in Aerospace Sciences*, vol. 38, no. 3, pp. 209–272, 2002.

[19] S. Jayaraju, F. Roelofs, E. Komen, and A. Dehbi, "RANS modeling of fluid flow and dust deposition in nuclear pebble-beds," *Nuclear Engineering and Design*, vol. 308, pp. 222–237, 2016.

[20] C. Zigh and J. Solis, "Computational Fluid Dynamics Best Practice Guidelines for Dry Cask Applications Final Report," tech. rep., United States Nuclear Regulatory Commission, 2013.

[21] L. F. Richardson, "The Approximate Arithmetical Solution by Finite Differences of Physical Problems involving Differential Equations, with an Application to the Stresses in a Masonry Dam," *Transactions of the Royal Society of London*, vol. 226, no. A, pp. 299–361, 1910.

[22] P. J. Roache, "Perspective: A method for uniform reporting of grid refinement studies," *Journal of Fluids Engineering*, vol. 116, pp. 405–413, 1994.

[23] E. A. Harvego, R. R. Schultz, and R. L. Crane, "Development of a consensus standard for verification and validation of nuclear system thermal-fluids software," *Nuclear Engineering and Design*, vol. 241, no. 12, pp. 4691–4696, 2011.

[24] P. J. Roache, *Fundamentals of Verification and Validation*. Hermosa Publishers, 2009.

[25] I. B. Celik and J. Li, "Assessment of Numerical Uncertainty for the Calculations of Turbulent Flow over a Backward Facing Step," in *Workshop on Uncertainty Estimation*, pp. 1–13, 2004.

[26] I. Celik, J. Li, G. Hu, and C. Shaffer, "Limitations of Richardson extrapolation and some possible remedies," *Journal of Fluids Engineering*, vol. 127, no. 4, pp. 796–805, 2005.

[27] F. Elizalde-Blancas, E. Karaismail, and I. B. Celik, “Application of Error Scaling Method in Conjunction with GCI,” in *3rd workshop on CFD uncertainty analysis*, (Lisbon, Portugal), pp. 1–15, 2008.

[28] I. B. Celik, E. Karaismail, F. Elizalde-Blancas, D. Parsons, and H. Sezer, “Error Estimation using Hybrid Methods,” in *ASME 2012 Fluids Engineering Division Summer Meeting (FEDSM2012)*, (Rio Grande, Puerto Rico), pp. 1–22, American Society of Mechanical Engineers, 2012.

[29] W. L. Oberkampf and C. J. Roy, *Verification and validation in scientific computing*. Cambridge ; New York : Cambridge University Press, 2010., 2010.

[30] T. Xing and F. Stern, “Factors of Safety for Richardson Extrapolation,” *Journal of Fluids Engineering*, vol. 132, no. 6, p. 061403, 2010.

[31] P. J. Roache, “Discussion: "Factors of Safety for Richardson Extrapolation" (Xing, T., and Stern, F., 2010, ASME J. Fluids Eng., 132, p. 061403),” *Journal of Fluids Engineering*, vol. 133, no. 11, p. 115501, 2011.

[32] T. Xing and F. Stern, “Closure to "Discussion of ’Factors of Safety for Richardson Extrapolation’ " (2011, ASME J. Fluids Eng., 133, p. 115501),” *Journal of Fluids Engineering*, vol. 133, no. November, p. 115502, 2011.

[33] L. Eça and M. Hoekstra, “An Evaluation of Verification Procedures for CFD Applications,” in *24th Symposium on Naval Hydrodynamics*, (Fukuoka), Kyushu University, 2002.

[34] T. S. Phillips and C. Roy, *Extrapolation-based Discretization Error and Uncertainty Estimation in Computational Fluid Dynamics Extrapolation-based Discretization Error and Uncertainty Estimation in Computational Fluid Dynamics*. PhD thesis, Virginia Polytechnic Institute and State University, 2012.

[35] L. Eça and M. Hoekstra, "A procedure for the estimation of the numerical uncertainty of CFD calculations based on grid refinement studies," *Journal of Computational Physics*, vol. 262, pp. 104–130, 2014.

[36] P. J. Roache, "Conservatism of the Grid Convergence Index in Finite Volume Computations on Steady-State Fluid Flow and Heat Transfer," *Journal of Fluids Engineering*, vol. 125, pp. 731–739, 2003.

[37] S. B. Pope, *Turbulent Flows*. New York: Cambridge University Press, 2000.

[38] N. Rajaratnam, *Turublent Jets*. Elsevier, 1976.

[39] G. Heskestad, "Hot-Wire Measurements in a Plane Turbulent Jet," *Journal of Applied Mechanics*, vol. 32, p. 721, 1965.

[40] E. Gutmark and I. Wygnanski, "The planar turbulent jet," *Journal of Fluid Mechanics*, vol. 73, no. 3, pp. 465–495, 1976.

[41] D. R. Miller and E. W. Comings, "Force-momentum fields in a dual-jet flow," *Journal of Fluid Mechanics*, vol. 7, no. 2, pp. 237–256, 1960.

[42] E. Tanaka, "The Interference of Two-Dimensional Parallel Jets (1st Report, Experiments on Dual Jets)," *Bulletin of the JSME*, vol. 13, no. 56, pp. 272–280, 1970.

[43] E. Tanaka, "The Interference of Two-Dimensional Parallel Jets (2nd Report, Experiments on the Combined Flow of Dual Jets)," *Bulletin of the JSME*, vol. 17, no. 109, pp. 920–927, 1974.

[44] G. Marsters, "The interaction of two plane parallel jets," *AIAA Journal*, vol. 15, no. 12, pp. 1756–1762, 1977.

[45] H. Elbanna, S. Gahin, and M. I. I. Rashed, "Investigation of Two Plane Parallel Jets," *AIAA Journal*, vol. 21, no. 7, pp. 986–991, 1982.

[46] Y. F. Lin and M. J. Sheu, "Investigation of two plane parallel unventilated jets," *Experiments in Fluids*, vol. 10, no. 1, pp. 17–22, 1990.

[47] A. Nasr and J. C. S. Lai, "Two parallel plane jets: Mean flow and effects of acoustic excitation," *Experiments in Fluids*, vol. 22, no. 3, pp. 251–260, 1997.

[48] P. Behrouzi and J. McGuirk, "Laser Doppler velocimetry measurements of twin-jet impingement flow for validation of computational models," *Optics and Lasers in Engineering*, vol. 30, no. 3-4, pp. 265–277, 1998.

[49] A. Tokuhiro and O. Omotowa, "Data Collection Methods for Validation of Advanced Multi-Resolution Fast Reactor Simulations," Tech. Rep. 09, University of Idaho, Idaho Falls, 2012.

[50] R. Vinuesa, P. Schlatter, and H. M. Nagib, "Characterization of the Secondary Flow in Turbulent Rectangular Ducts With Varying Aspect Ratio," in *International Symposium On Turbulence and Shear Flow Phenomena*, (Melbourne, Australia), pp. 1–6, 2015.

[51] S. Lee and Y. A. Hassan, "Proper Orthogonal Decomposition Analysis of Parallel Twin Jets Measured Using Particle Image Velocimetry," in *2016 International Topical Meeting on High Temperature Reactor Technology (HTR 2016)*, no. 4, (Las Vegas, NV), pp. 172–179, 2016.

[52] A. Cabral, S. Lee, and Y. A. Hassan, "Finding MP and CP using Ultrasonic Velocity Profile on Rectangular Twin Jets," in *Transactions of the American Nuclear Society*, vol. 115, (Las Vegas, NV), pp. 1675–1678, 2016.

[53] H. Wang and Y. A. Hassan, "Benchmark Data for Validation of Computational Simulations of Nuclear System Thermal Fluids Behavior," tech. rep., Texas A&M University, College Station, 2015.

[54] A. Sciacchitano and B. Wieneke, "PIV uncertainty propagation," *Measurement Science and Technology*, vol. 27, no. 8, p. 084006, 2016.

[55] W. P. Jones and B. E. Launder, "The Prediction of Laminarization with a Two-Equation Model of Turbulence," *International Journal of Heat and Mass Transfer*, vol. 15, pp. 301–314, 1972.

[56] B. E. Launder and B. I. Sharma, "Application of the energy-dissipation model of turbulence to the calculation of flow near a spinning disc," *Letters in Heat and Mass Transfer*, vol. 1, no. 2, pp. 131–138, 1974.

[57] CD-Adapco, "Star-CCM+ 10.06.010 User's Guide," 2016.

[58] W. Rodi, "Experience with two-layer models combining the k-epsilon model with a one-equation model near the wall," in *29th Aerospace Sciences Meeting*, (Reno, Nevada), pp. 1–12, American Institute of Aeronautics and Astronautics, 1991.

[59] L. B. Carasik, F. Sebilleau, S. P. Walker, and Y. A. Hassan, "Numerical simulations of a mixed momentum-driven and buoyancy-driven jet in a large enclosure for nuclear reactor severe accident analysis," *Nuclear Engineering and Design*, vol. 312, pp. 161–171, Nov 2017.

[60] L. Carasik, A. Ruggles, and Y. Hassan, "Preliminary investigation of turbulent flow behavior of 3-D twin jets using CFD analysis," in *Transactions of the American Nuclear Society*, vol. 110, (Reno, Nevada), pp. 689–692, American Nuclear Society, 2014.

[61] L. B. Carasik, H. Wang, and Y. A. Hassan, "Verification and Validation of CFD Simulations involving Twin Rectangular Jets using Steady RANS in Star-CCM+," in *Transactions of the American Nuclear Society*, vol. 115, (Las Vegas, NV), pp. 1789–1792, American Nuclear Society, 2016.

[62] I. B. Celik, U. Ghia, P. J. Roache, C. J. Freitas, H. Coleman, and P. E. Raad, "Procedure for Estimation and Reporting of Uncertainty Due to Discretization in CFD Applications," *Journal of Fluids Engineering*, vol. 130, no. 7, pp. 1–4, 2008.

[63] L. Eça and M. Hoekstra, "Discretization Uncertainty Estimation based on a Least Squares version of the Grid Convergence Index," in *Proceedings of the Second Workshop on CFD Uncertainty Analysis, Instituto Superior Tecnico, Lisbon, Oct*, (Lisbon, Portugal), pp. 1–27, 2006.

APPENDIX A

TWO-EQUATIONS TURBULENCE MODELS

A.1 Standard $\kappa - \epsilon$ Turbulence Model

The two equations for the standard $\kappa - \epsilon$ turbulence model are shown in

$$\rho\frac{\partial\kappa}{\partial t} + \rho\nabla\kappa\overrightarrow{u} = \nabla[(\mu + \frac{\mu_t}{\sigma_k})\nabla\kappa] + P_\kappa - \rho(\epsilon - \epsilon_0) + S_\kappa \tag{A.1}$$

$$\rho\frac{\partial\epsilon}{\partial t} + \rho\nabla\epsilon\overrightarrow{u} = \nabla[(\mu + \frac{\mu_t}{\sigma_k})\nabla\epsilon] + \frac{1}{T_0}C_{\epsilon_1}P_\epsilon - C_{\epsilon_2}f_2\rho(\frac{\epsilon}{T_e} - \frac{\epsilon_0}{T_0}) + S_\epsilon \tag{A.2}$$

where κ and ϵ are the turbulent kinetic energy and turbulent dissipation. The dynamic viscosity is shown as μ and μ_t is the dynamic eddy viscosity which is calculated using equation A.3. The terms P_κ and P_ϵ are the production terms for each equation. The terms S_κ and S_ϵ are source terms that can be added as needed. ϵ_0 is the ambient dissipation in the source terms. T_0 is the user defined turbulent time-scale defined in equation A.5. The coefficient f_2 is a damping function. T_e is the eddy turbulent time scale defined as $\frac{\kappa}{\epsilon}$. The coefficients; σ_κ, σ_ϵ, $C_{\epsilon 1}$, $C_{\epsilon 2}$ are all model coefficients that are summarized in table A.1.

$$\mu_t = \rho C_\mu f_\mu \kappa T \tag{A.3}$$

where C_μ is a modeling coefficient, f_μ is a damping function and T is the turbulent time scale defined in equation A.4.

$$T = max\left(T_e, C_t, \sqrt{\frac{\nu}{\epsilon}}\right) \tag{A.4}$$

where C_t is a modeling coefficient.

$$T_0 = max\left(\frac{k_0}{\epsilon_0}, C_t, \sqrt{\frac{\nu}{\epsilon_0}}\right) \tag{A.5}$$

Coefficient or Parameter	Value
σ_κ	1.3
σ_ϵ	1.0
C_μ	0.09
$C_{\epsilon 1}$	1.44
$C_{\epsilon 2}$	1.92
C_t	1.0
f_2	1.0
f_μ	1.0

Table A.1: Summary of Values used for the Model Coefficients